Roy Wang

196 Words

Measurements of the Inclusive Semileptonic Branching Fraction of B Mesons at the Upsilon(4S) Resonance

We present precision measurements of the inclusive semileptonic branching fraction of the B mesons from 2.057 fb^{-1} of Υ(4S) data collected with the CLEO-II detector. By fitting the inclusive lepton spectra to the refined quark model of Altarelli *et al.*, we obtain $\mathcal{B}(B \to X\ell\nu) = (10.56 \pm 0.04 \pm 0.22)\%$. With a modified version of the form-factor model of Isgur *et al.*, in which the fraction of $B \to D^{**}\ell\nu$ is allowed to float, we find $\mathcal{B}(B \to X\ell\nu) = (10.96 \pm 0.07 \pm 0.22)\%$. The original Isgur model yields a lower branching ratio, $\mathcal{B}(B \to X\ell\nu) = (10.26 \pm 0.03 \pm 0.22)\%$, but with a higher χ^2.

To reduce the dependence on theoretical models and sensitivity to possible non-$B\bar{B}$ decays of the Υ(4S), we have made a second measurement with dilepton events. In events with a high momentum lepton tag and an electron we use charge and kinematic correlations to separate the electron spectra of B decays and secondary charm decays. With a small extrapolation to account for the undetected part of the spectrum at low momentum, we obtain $\mathcal{B}(B \to Xe\nu) = (10.46 \pm 0.17 \pm 0.43)\%$. This measurement is largely independent of theoretical models and assumptions about possible non-$B\bar{B}$ decays of the Υ(4S).

Based on our branching ratio results, we have also measured the CKM matrix element $|V_{cb}|$ with precision and confirmed the CLEO measurement of $|V_{ub}|$.

UNIVERSITY OF MINNESOTA

This is to certify that I have examined this bound copy of a doctoral thesis by

Roy Wang

and have found that it is complete and satisfactory in all respects and that any and all revisions required by the final examining committee have been made.

Professor Ronald A. Poling

(Faculty Adviser)

GRADUATE SCHOOL

Measurements of the Inclusive Semileptonic Branching Fraction of B Mesons at the Upsilon(4S) Resonance

A THESIS

SUBMITTED TO THE FACULTY OF THE GRADUATE SCHOOL

OF THE UNIVERSITY OF MINNESOTA

BY

Roy Wang

IN PARTIAL FULFILLMENT OF THE REQUIREMENTS

FOR THE DEGREE OF

DOCTOR OF PHILOSOPHY

December, 1994

Measurements of the Inclusive Semileptonic Branching Fraction of B Mesons at the Upsilon(4S) Resonance

by Roy Wang

Under the supervision of Professor Ronald A. Poling

ABSTRACT

We present precision measurements of the inclusive semileptonic branching fraction of the B mesons from 2.057 fb^{-1} of $\Upsilon(4S)$ data collected with the CLEO-II detector. By fitting the inclusive lepton spectra to the refined quark model of Altarelli *et al.,* we obtain $\mathcal{B}(B \to X\ell\nu) = (10.56 \pm 0.04 \pm 0.22)\%$. With a modified version of the form-factor model of Isgur *et al.,* in which the fraction of $B \to D^{**}\ell\nu$ is allowed to float, we find $\mathcal{B}(B \to X\ell\nu) = (10.96 \pm 0.07 \pm 0.22)\%$. The original Isgur model yields a lower branching ratio, $\mathcal{B}(B \to X\ell\nu) = (10.26 \pm 0.03 \pm 0.22)\%$, but with a higher χ^2.

To reduce the dependence on theoretical models and sensitivity to possible non-$B\bar{B}$ decays of the $\Upsilon(4S)$, we have made a second measurement with dilepton events. In events with a high momentum lepton tag and an electron we use charge and kinematic correlations to separate the electron spectra of B decays and secondary charm decays. With a small extrapolation to account for the undetected part of the spectrum at low momentum, we obtain $\mathcal{B}(B \to Xe\nu) = (10.46 \pm 0.17 \pm 0.43)\%$. This measurement is largely independent of theoretical models and assumptions about possible non-$B\bar{B}$ decays of the $\Upsilon(4S)$.

Based on our branching ratio results, we have also measured the CKM matrix element $|V_{cb}|$ with precision and confirmed the CLEO measurement of $|V_{ub}|$.

Acknowledgement

This thesis work is done in the excellent research environment of the CLEO Collaboration, the School of Physics and Astronomy at the University of Minnesota and the Laboratory of Nuclear Studies at Cornell University. I would like to acknowledge the staff that has created this environment which I have benefited tremendously. In particular, I would like to thank the following people.

Professor Ron Poling has been a great inspiration. He represents much of what I respect both in professional standards and personal dignity. I have no better way to express my appreciation but to present a good thesis.

My CLEO paper committee has done most of the quality control for the two analyses in this thesis. Professor Jeff Richman, Doctors Franz Muheim, David Cinabro and Karen Lingel, they deserve credit.

Professor Ed Thorndike introduced the CLEO experiment to me, and has been a constant source of wisdom for my years at Wilson Lab. I would also like to thank Professor Yuichi Kubota for many discussions. Their sharpness is often a challenge that my work has to face.

I greatly appreciate the help from my fellow Minnesotans in our office. I thank Dave Perticone for the effort he put into the inclusive lepton analysis, Simon Patton and Dan Riley for helping me on computing and software. Especially, I would like to thank Jeff Nelson and Steve Schrenk for many things they have taught me, from calibration database to thesis typesetting.

I would like to thank my parents for their support, and my wife Eva for her encouragement.

Table of Contents

Chapter 1

Semileptonic Decay of B Mesons

Overview: This thesis approaches the question: what is the fraction of time that a B meson decays to a lepton and its antineutrino? In this chapter, we review the basic physics that leads to this question.

1.1 Particles and Interactions

Elementary particle physics is the science that studies the fundamental building blocks of matter and their interactions. Ever since the beginning of our civilization, the human quest for this knowledge has been progressing, from Democritus's concept of atoms, to Newton's formulation of gravity, to Maxwell's unification of the electric and magnetic forces, and so on. To date, we have reached a basic understanding of the world we live in. We know that visible matter in our universe consists of quarks and leptons, and they interact through the four fundamental forces: strong, electromagnetic, weak and gravitational.

Quarks and leptons have spin 1/2 and are therefore Fermions. They are naturally put into three generations, or families, as listed in Table 1.1. The first two leptons are very light [1] ($m_e = 0.51\,\mathrm{MeV/c^2}$ and $m_\mu = 106\,\mathrm{MeV/c^2}$), while the τ is much heavier ($m_\tau = 1777\,\mathrm{MeV/c^2}$ [2]). The neutrinos have very little or no mass. The up, down and strange quarks (u, d and s) are relatively light. Their masses range from a few to a few hundred $\mathrm{MeV/c^2}$. The charm, bottom and top quarks (c, b and t) are heavier, with $m_c \approx 1.3 - 1.5\,\mathrm{GeV/c^2}$, $m_b \approx 4.7 - 5.0\,\mathrm{GeV/c^2}$. Evidence of the top quark has recently been observed by the CDF experiment at Fermilab's Tevatron $p\bar{p}$ collider [3], and its mass has been inferred to be 174 ± 16 GeV/c^2. The bottom quark is the main constituent of the B mesons which are the subject of the research described in this thesis. As the partner of the top quark, the b is the lighter member of the heaviest quark doublet. Since it cannot decay to its own partner, the b quark must decay intergenerationally. How the b quark resolves the choice between possible decay modes provides a unique glimpse into the inner workings of our theory of fundamental interactions. This is the root of much of the importance and excitement of b-quark physics.

Table 1.1: Fermions and their Electric Charges.

$$
\begin{array}{lcccr}
\text{leptons} & \begin{pmatrix} e \\ \nu_e \end{pmatrix} & \begin{pmatrix} \mu \\ \nu_\mu \end{pmatrix} & \begin{pmatrix} \tau \\ \nu_\tau \end{pmatrix} & \begin{array}{r} -e \\ 0 \end{array} \\
\text{quarks} & \begin{pmatrix} u \\ d \end{pmatrix} & \begin{pmatrix} c \\ s \end{pmatrix} & \begin{pmatrix} t \\ b \end{pmatrix} & \begin{array}{r} +\frac{2}{3}e \\ -\frac{1}{3}e \end{array}
\end{array}
$$

Quarks and leptons are considered fundamental for two obvious but nontrivial reasons. First, they and their antiparticles make up matter. Atoms for example, are made up of electrons and nuclei. Nuclei consist of nucleons (protons and neutrons), which in turn are made of quarks. In an oversimplified picture, a proton consists of two up quarks and one down quark, $p = uud$. Similarly, a neutron's composition is $n = udd$. The B meson we study in this thesis is composed of a bottom quark and a light antiquark, *i.e.* $B^- = b\bar{u}$ and $\bar{B}^0 = b\bar{d}$. The second reason we consider the Fermions fundamental is that they are not decomposable. Both leptons and quarks are smaller than $10^{-18}\,m$, many orders of magnitude smaller than the size of atoms, which is approximately $10^{-10}\,m$. At the current experimental level, no compositeness has been observed.

The four interactions between the Fermions are carried by gauge bosons, as listed in Table 1.2. Gluons mediate the strong interactions between any two quarks; photons carry the electromagnetic force between any two quarks or charged leptons; the $W^{\pm}$ and Z^0 mediate the weak interaction within one and between two families of Fermions; and finally the gravitons carry the gravitational force between any two particles with mass. The word gauge arises from the mathematical formalism of quantum field theory, in which every interaction is a consequence of a fundamental symmetry in nature. We now discuss the gauge symmetries that give rise to the four types of interactions within our current theoretical framework — the Standard Model.

Table 1.2: Fundamental Forces and Gauge Bosons

Force	Boson	Symbol	Charge	Spin	Mass (GeV/c^2)
Strong	gluon	g	0	1	0
Electromagnetic	photon	γ	0	1	0
Weak	W	$W^{\pm}$	$\pm e$	1	81
	Z	Z^0	0	1	92
Gravitational	graviton	G	0	2	0

1.2 Theoretical Description of Interactions

The fundamental interactions are formulated mathematically by quantum field theory. Like any other physical system, the Lagrangian defines the dynamics of the interacting particles [4]. The Lagrangian of a certain interaction is constructed from the fundamental nature of that force — gauge symmetry. For a particle with wave function Ψ, the choice of an arbitrary phase (or gauge) α, changes the wave function to $e^{i\alpha}\Psi$, but does not change the observable, the probability $|\Psi|^2$. Gauge symmetry is simply the property that the Lagrangian is invariant under a gauge transformation $\chi(\vec{x},t)$

$$\Psi(\vec{x},t) \rightarrow e^{i\chi(\vec{x},t)}\Psi(\vec{x},t). \tag{1.1}$$

The theory of strong interactions, quantum chromodynamics (QCD), arises from a special unitary symmetry SU(3). The three basic dimensions are named after three colors, red, green and blue. This convention takes advantage of aspects of color theory in optics to represent similar features of the properties of the strong (color) interaction. Quarks are color singlet, and the Lagrangian decribing the "color" force between quark q_α of color α and quark q_β of color β is given by

$$\mathcal{L}_{QCD} = \frac{g_3}{2}\sum \bar{q_\alpha}\gamma^\mu\lambda^\delta_{\alpha\beta}q_\beta G^\delta_\mu. \tag{1.2}$$

In this equation G is the force carrier — the gluon field, g_3 is the coupling strength, and γ and λ are the Dirac and Gell-Mann matrices describing the spin of the quarks and color of the gluons, respectively. The mediating gluon between quarks q_α and q_β must contain both color α and β. The gluons which mediate the strong force bring about color transformations. From the three colors eight independent gluon combinations can be constructed:

$$r\bar{b},\quad r\bar{g},\quad b\bar{g},\quad g\bar{r},\quad \frac{1}{\sqrt{2}}(r\bar{r}-b\bar{b}),\quad \frac{1}{\sqrt{6}}(r\bar{r}+b\bar{b}-g\bar{g}), \tag{1.3}$$

where r, g and b signify the colors, and $\bar{r},\quad \bar{b},\quad \bar{g}$ the corresponding anticolors.

An important feature of the combination is color confinement. When quarks form matter, the particles formed (hadrons) are color singlets (colorless). The color-triplet quarks have been observed to form only two types of hadrons, mesons and baryons. A meson consists of a quark and an antiquark with opposite colors,

$$q_1\bar{q_2} = \frac{1}{\sqrt{3}}(r\bar{r}+b\bar{b}+g\bar{g}). \tag{1.4}$$

Examples include light mesons $\pi^+ = u\bar{d}$, $\pi^- = \bar{u}d$, $\pi^0 = \frac{1}{\sqrt{2}}(u\bar{u}+d\bar{d})$, $K^+ = \bar{s}u$, $K^- = s\bar{u}$, $K^0 = s\bar{d}$, $\bar{K^0} = \bar{s}d$ and heavy mesons $D^+ = c\bar{d}$, $D^- = \bar{c}d$, $D^0 = c\bar{u}$ and

$\bar{D}^0 = \bar{c}u$. The B mesons we study in this thesis contain a b-quark and a light quark: $B^- = b\bar{u}$, $B^+ = \bar{b}u$, $\bar{B}^0 = b\bar{d}$ and $B^0 = \bar{b}d$. A baryon consists of three quarks, with the color combination

$$q_1 q_2 q_3 = \frac{1}{\sqrt{6}} \begin{vmatrix} r_1 & r_2 & r_3 \\ b_1 & b_2 & b_3 \\ g_1 & g_2 & g_3 \end{vmatrix} . \tag{1.5}$$

These include the proton $p = uud$, neutron $n = udd$ and charmed baryon $\Lambda_c^+ = cuu$, and their antiparticle parteners $\bar{p} = \bar{u}\bar{u}\bar{d}$, $\bar{n} = \bar{u}\bar{d}\bar{d}$ and $\Lambda_c^- = \bar{c}\bar{u}\bar{u}$.

Another important feature of QCD is asymptotic freedom. The coupling strength decreases as the momentum involved in the interaction increases, and at infinite momentum the coupling vanishes. This, on one hand, makes it possible to do perturbative expansions when calculating many processes. The much stronger coupling at smaller momenta, on the other hand, is yet to be understood. As B-meson decays involve momentum transfers in the nonperturbative region, phenomenological models are introduced in our discussion in the next section.

The electromagnetic and the weak interactions have been unified into a combined SU(2)×U(1) symmetry. The electroweak Lagrangian for the first generation of Fermions, for instance, is

$$\begin{aligned} \mathcal{L}_{EW} &= \sum_{f=l,q} eQ_f(\bar{f}\gamma^\mu f)A^\mu \\ &+ \frac{g_2}{\cos\theta_W} \sum_{f=l,q} \left[\bar{f}_L\gamma^\mu f_L(T_f^3 - Q_f \sin^2\theta_W) + \bar{f}_R\gamma^\mu f_R(-Q_f\sin^2\theta_W) \right] Z_\mu \\ &+ \frac{g_2}{\sqrt{2}} \left[(\bar{u_L}\gamma^\mu d_L + \bar{\nu_{eL}}\gamma^\mu e_L)W_\mu^+ + (\text{Hermitian Conjugate}) \right], \end{aligned} \tag{1.6}$$

where A, Z and W are the fields for the photon and the two weak gauge bosons Z and W; g_2 is the weak charge or coupling strength; L and R are the helicities of the Fermions (the left- or right-handedness of their spins with respect to their direction of motion). T is a matrix which combines the electric and weak charge for Fermions. The Weinberg angle θ_W represents the relative strength of the electromagnetic interaction

g_1 in the unified theory:

$$\sin\theta_W = \frac{g_1}{\sqrt{g_1^2 + g_2^2}}, \tag{1.7}$$

so that $e = g_1 \cos\theta_W = g_2 \sin\theta_W$. At the energy scale below 100GeV, $\sin^2\theta_W \approx 0.23$.

The interactions represented by the Lagrangian can be expressed graphically with the Feynman diagrams, in which the Fermion fields are straight lines, and the intermediate bosons curly lines. They interact by a connected vertex or "current". The photon and Z boson carry the neutral current between a Fermion and its anti-Fermion, as shown in Fig. 1.1a. The W bosons carry the charged currents, as in Fig. 1.1b. This interaction

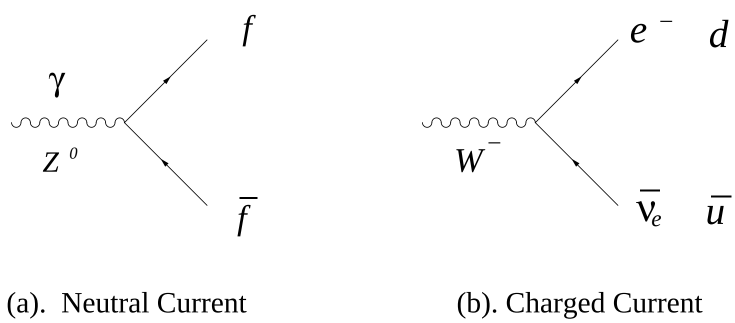

Figure 1.1: Electroweak currents.

results in the change of quark flavors, or the interchange of leptons and their neutrinos. The charged current for leptons is expressed as

$$J_\mu = (\bar{\nu_e} \quad \bar{\nu_\mu} \quad \bar{\nu_\tau})\gamma_\mu(1-\gamma_5)\begin{pmatrix} e \\ \mu \\ \tau \end{pmatrix}. \tag{1.8}$$

The charged current happens not only to Fermions within a family, but also between different quark families. When a b quark decays, for example, it can decay either to a charm quark, $b \to cW^-$, or to an up quark, $b \to uW^-$, as in Fig. 1.2. The charged

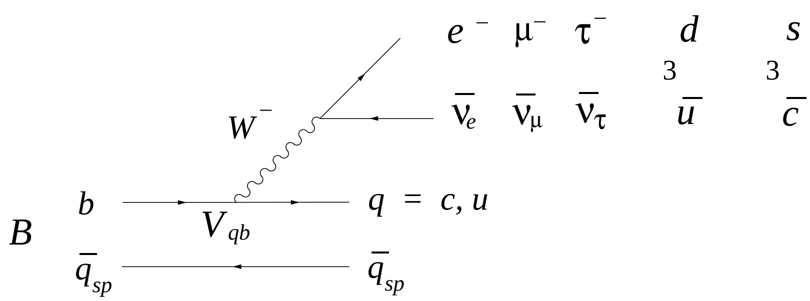

Figure 1.2: Spectator decays of B mesons.

current for quarks is similar to Eq. 1.8 except for the additional factor V_{ij}:

$$J_\mu = (\bar{u} \quad \bar{c} \quad \bar{t})\gamma_\mu(1-\gamma_5)V_{ij}\begin{pmatrix} d \\ s \\ b \end{pmatrix}. \tag{1.9}$$

The V_{ij} are elements of the Cabibbo-Kobayashi-Maskawa matrix. This unitary matrix describes quark mixing, and can be approximately represented by the following parametrization suggested by Wolfenstein:

$$\begin{pmatrix} V_{ud} & V_{us} & V_{ub} \\ V_{cd} & V_{cs} & V_{cb} \\ V_{td} & V_{ts} & V_{tb} \end{pmatrix} \approx \begin{pmatrix} 1-\frac{1}{2}\lambda^2 & \lambda & A\lambda^3(\rho - i\eta) \\ -\lambda & 1-\frac{1}{2}\lambda^2 & A\lambda^2 \\ A\lambda^3(1-\rho-i\eta) & -A\lambda^2 & 1 \end{pmatrix}. \tag{1.10}$$

The parameters must be determined experimentally. It is found that both A and λ are smaller than one, with $A \approx 0.94 \pm 0.10$ and $\lambda = 0.22$. As shown in the above parametrization, the diagonal elements V_{ud}, V_{cs}, V_{tb} are close to unity (0.97-1.00), and the farther away an element is from the diagonal, the smaller its magnitude. The amplitudes of the two b-quark decay processes in Fig. 1.2, for instance, are proportional to V_{cb} and V_{ub}. One of the goals of the analyses described in this thesis is the determination of the values of these two CKM elements through our measurement of the decay rates of $b \to qW^-$, $W^- \to \ell^- \bar{\nu}_l$ for $q = c$ and u.

The existence of the CKM matrix is a direct consequence of the fact that the weak interaction eigenstates are not exactly the mass eigenstates. Quark mixing occurs via this inter-family coupling. Its existence is essential for the electroweak theory to hold, as it is the only way to allow charge-parity symmetry violation. CP violation is observed in neutral kaon decays, in which the width of K^0 and that of its anti-particle $\bar{K^0}$ differ by about 1%. A similar difference is expected in neutral B-meson decays. Under the assumption that CPT is a good symmetry, the violation of CP also demands the non-conservation of time reversal T. In quantum theory, time is the observable of the operator t in $e^{-\frac{i}{\hbar}Et}$. If time reversal symmetry is broken, our theory must contain a complex phase. This is exactly incorporated in $V_{ub} = A\lambda^3(\rho - i\eta)$ in the CKM matrix. The tiny amount of CP asymmetry may hold the key to the question of why there is an excess of matter in our universe over antimatter. While we have a description of CP violation in the Standard Model, its underlying origin is yet to be understood.

In spite of the tremendous success we have achieved so far, we must concede that our understanding of the fundamental interactions is primitive. We are compelled to find the answers to many important unanswered questions. One of the most crucial is what gives mass to the Fermions? The gauge symmetry $\mathrm{SU}(2) \times \mathrm{U}(1)$ is invariant only if the Fermions are massless. The very fact that they have mass breaks the symmetry at our energy scale. The Higgs mechanism was proposed to explain this symmetry breaking. We hope that the Large Hadron Collider (LHC), being planned at the European particle physics laboratory (CERN), will lead to an understanding of this mechanism. Another fundamental question was raised above: what is the nature of CP violation? The B factories under construction at the Stanford Linear Accelerator Center (SLAC), and at the Japanese laboratory KEK, as well as the upgrade of the Cornell Electron Storage Ring (CESR), are aimed at seeking the answer. Still another question is why there seem to be three and only three families of Fermions? Last, we currently do not have either a theory that includes gravity, or any experimental evidence of gravitational quanta.

Just as electricity and magnetism were unified by Maxwell, and electromagnetism and the weak forces were unified by Weinberg, Salam and Glashow, we seek the ultimate unification of all of the interactions. At our current laboratory energy scale (below 200 GeV), the strengths of the four forces come in the order of strong, electromagnetic, weak and gravitational. The strengths of the interactions $g_1 \cdots g_4$ change with changing energy scale, however. At higher energies, the differences decrease, which leads to the idea of a unified interaction from a very simple symmetry. We believe that the four interactions are just different manifestations of this symmetry at lower energy scales. Even though we are far from this goal, we currently have several different theories which help to expand our horizon, such as supersymmetry and string theory. All of them greatly demand experimental information. Among many efforts on the experimental front, this thesis addresses a very simple but important question, which we discuss next: what is the probability that a B meson decays to a lepton?

1.3 Semileptonic Decay of B Mesons

The B meson is a bound state of a b quark and a light antiquark $\bar{u}$ or $\bar{d}$. Studying the decays of B mesons provides information about the interactions of the b quark, since it dominates the B meson. The lifetime of the B mesons has been measured to be about 1.5×10^{-12}s. They decay quickly after they are produced. The dominant mechanism is the weak decay of the b quark to either a c quark or a u quark plus a W boson via the charged current depicted in Fig. 1.2. The W boson can in turn decay into lepton pairs $(e, \bar{\nu_e})$, $(\mu, \bar{\nu_\mu})$, $(\tau, \bar{\nu_\tau})$ and quark pairs $(\bar{u}, d)$, $(\bar{c}, s)$, as shown in Fig. 1.2. The factors of 3 for the decay modes with quarks are due to the contribution from all three colors in the strong interaction. Of all the possible decay channels, we study $B \to X\ell\nu$, where $\ell = e$ or μ. There are two principal reasons. First, the quark channels involve a lot of complicated strong interactions. Second, electrons and muons are the easiest particles to identify in our experiment with high purity and efficiency, as we will show in Chapter 2. The question we ask is: what fraction of all B-meson decays are final states with leptons? The quantity we measure is the inclusive semileptonic branching fraction of the B meson $\mathcal{B}(B \to X\ell\nu)$ for $\ell = e$ or μ. From now on we will use the word "lepton" for electrons and muons. We will call the τ lepton explicitly τ.

1.3.1 The Inclusive Branching Ratio

Semileptonic decays play important roles in B-meson physics. They are the simplest to understand, and are the foundation for understanding hadronic decays. They also provide means to determine the CKM matrix elements V_{cb} and V_{ub}, as the decay amplitudes are proportional to these two elements.

The inclusive semileptonic ratio itself is one of the longstanding puzzles of B physics as measurements have consistently been significantly smaller than theoretical expectations [5, 6]. The latest theoretical advances based on heavy quark expansions have greatly increased the urgency for understanding this discrepancy [7]. If this difference can not be resolved within the framework of the Standard Model, we will be compelled to attribute it to indications of new physics.

In the simple spectator description (Fig. 1.2), the b quark decays into lepton pairs or quark pairs. The decay rate for each one of these pairs is proportional to its phase space factor r, reflecting the mass of the pair. The total decay width is then the sum:

$$\Gamma(B) = \frac{G_F^2 |V_{cb}|^2 m_b^5}{192\pi^3} \eta_{QCD}(2r_l + r_\tau + 3r_{ud} + 3r_{cs}) \tag{1.11}$$

where $G_F = \sqrt{2}g_2^2/8M_W^2$ is the Fermi constant, and $\eta_{QCD} \approx 0.94$ is a QCD correction factor [8]. The semileptonic fraction for $B \to X\ell\nu$ ($\ell = e$ or μ) is therefore simply r_l divided by the sum of the phase space factors:

$$\mathcal{B}(B \to X\ell\nu) = \frac{r_l}{2r_l + r_\tau + 3r_{ud} + 3r_{cs}}. \tag{1.12}$$

The masses of the leptons are precisely measured. The masses of their neutrinos are negligiblly small and quite possiblly zero. Therefore $r_l = 0.45$ and $r_\tau = 0.12$ are well defined. The phase space factors for the quark pairs bear ambiguities, due to the uncertainties of the quark masses. Assigning the mass values from the best of our knowledge [9], $m_u \approx m_d \approx 0$, $m_s = 0.5\,\mathrm{GeV/c^2}$, $m_c = 1.4\,\mathrm{GeV/c^2}$, we obtain $r_{ud} \approx r_l \approx 0.45$ and $r_{cs} \approx 0.12$. Substituting these values into Eq. 1.12, we find $\mathcal{B}(B \to X\ell\nu) = 16.5\%$.

The spectator model assumes that the light quark u or d in the B meson does not participate the interaction, acting only as a spectator. This is very naive. Corrections must be introduced to account for gluon radiation and exchange between all quarks in the decay processes [10]. This enhances the hadronic channels, and in turn reduces the semileptonic ratio to

$$\mathcal{B}(B \to X\ell\nu) = \frac{r_l}{2r_l + r_\tau + 1.24 \times 3(r_{ud} + r_{cs})} = 14.5\%. \tag{1.13}$$

In this equation, the factor 1.24 is the result of QCD corrections.

After strong indications from earlier measurements that the branching fraction is lower than this prediction, the estimate of the above equations are reassessed. It was observed that choosing a lower charm quark mass m_c would enhance the (c, s) channel, and reduce the semileptonic ratio even more. If we stretch the c-quark mass to the extreme, *i.e.*, a lower boundary of $m_c \approx 1.2\,\mathrm{GeV/c^2}$, we obtain the lower limit of the theoretical expectation

$$\mathcal{B}(B \to X\ell\nu) > 12.5\%. \tag{1.14}$$

Recent theoretical developments on heavy quark expansion have demonstrated great potential for calculating B semileptonic and hadronic decays from fundamental principles. These efforts led to the same conclusion, that this branching ratio must be greater than 12.5% with our present knowledge of heavy quark interactions.

All the experimental measurements [1, 5] have been below 12.5% (Table 1.3). Almost all are significantly below. The two experiments at the B-meson production threshold in $e^+ e^-$ collisions, CLEO at CESR [11] and ARGUS at the German Electron Synchrotron

(DESY) [12] provide the best precision, and the clearest indication of a significant discrepancy. Before discussing such measurements in great detail, we must first review the theoretical picture of semileptonic B-meson decay more thoroughly.

Table 1.3: Results from Previous Experiments

Experiment	$\mathcal{B}(B \to X\ell\nu)(\%)$	$\mathrm{E}_{\mathrm{C.M.}}$ (GeV)
Mark-II	$11.2 \pm 0.9 \pm 1.1$	15–50
MAC	$15.5^{+5.4}_{-2.0}$	
Mark J	$10.5 \pm 1.5 \pm 1.3$	
DELCO	$11.9 \pm 0.4 \pm 0.7$	
TASSO	$11.7 \pm 2.8 \pm 1.0$	
JADE	$11.7 \pm 1.6 \pm 1.5$	
TPC	$10.8 \pm 0.4 \pm 0.7$	
ALEPH	$10.3 \pm 0.7 \pm 0.5$	$M(Z^0) \approx 92$
L3	$11.9 \pm 0.3 \pm 0.6$	
OPAL	$10.4 \pm 0.3 \pm 0.6$	
DELPHI	$10.6 \pm 0.5 \pm 0.6$	
ARGUS	$10.2 \pm 0.4 \pm 0.2$	$M(\Upsilon(4S)) \approx 10.6$
CLEO 1.5	$10.5 \pm 0.2 \pm 0.4$	

1.3.2 Theoretical Work on Semileptonic B Decays

The decay rate of a certain particle reaction such as those we have discussed so far, is calculated from the scattering matrix element M. The rate is proportional to $|M|^2$, similar to the probability $|\Psi|^2$ for a particle represented by wave function Ψ in quantum mechanics. The simplicity of B semileptonic decay is reflected in the factorized expression of its matrix element

$$M = J_{lep} \cdot J_{had}, \tag{1.15}$$

where the J's stand for the leptonic and hadronic currents. The leptonic current is well understood in electroweak theory, as is expressed in Eq. 1.8. Calculation of the hadronic current J_{had} from first principles is not possible with our present theory, due to the lack of knowledge about the non-perturbative QCD interactions involved. It is possible, however, to simulate the dynamic system with phenomenological methods. The hadronic current J_{had} can be treated in two different ways: inclusively or exclusively.

Inclusive Models The inclusive models treat B-meson decays at the quark level. The interaction of the b quark with the spectator and other quarks involved, is described by

$$J_{had} = < \bar{q}|j^{\mu}_{had}|b > . \tag{1.16}$$

The model we use was developed by Altarelli, Cabibbo, Corbò, Maiani and Martinelli [13] (ACCMM). The B semileptonic width in this model is

$$\frac{d\Gamma(B \to X\ell\nu)}{dx} = \frac{G_F^2|V_{cb}|^2 m_b^5}{96\pi^3}\left[\Phi(x,\epsilon) - G(x,\epsilon)\right], \tag{1.17}$$

where $x = 2E_\ell/m_b$ for lepton energy E_ℓ, $\epsilon = m_c/m_b$ and Φ is a function which describes the free-quark decay distribution:

$$\Phi(x,\epsilon) = \frac{x^2(1-\epsilon^2-x)^2}{(1-x)^3}\left[(1-x)(3-2x) + (3-x)\epsilon^2\right]. \tag{1.18}$$

The ACCMM model includes two modifications to the free-quark model: the effect of gluon radiation, as represented by function $G(x,\epsilon)$, and the Fermi motion inside the B meson. First, gluon corrections account for higher order QCD effects. We show two typical Feynman diagrams in Fig. 1.3. The one on the left represents real gluon

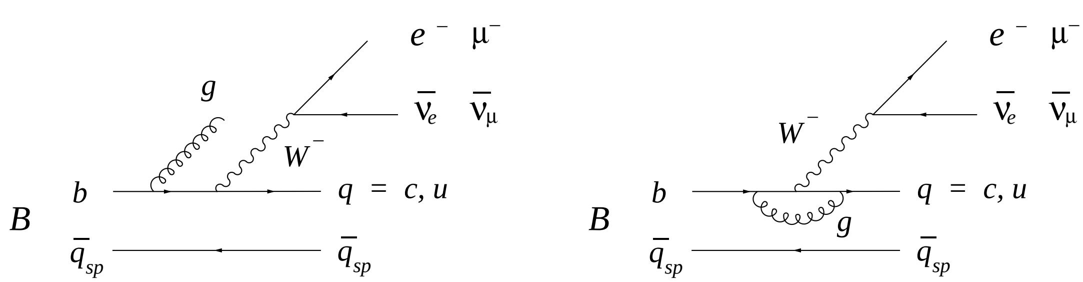

Figure 1.3: QCD radiative corrections.

radiation, and the one on the right, virtual gluon exchanges or corrections on the vertex.

The resulting correction [14] to the free-quark calculation is a complicated function $G(x, \epsilon)$ that changes the free-quark lepton spectrum only slightly for most values of x. In the end-point region, where $x \to x_M = 1 - \epsilon^2$, the correction is significant since G involves a logarithmic divergence:

$$G(x, \epsilon) = (\text{finite terms}) + 2\ln(x_M - x)\,[2x_M + (2 - x_M)\ln(1 - x_M)]\,. \tag{1.19}$$

The choice of the b-quark mass in Eq. 1.17 introduces sizable uncertainties due to the 5th power of m_b. In the ACCMM description, the B meson is a two-body system of the b quark and the spectator quark q_{sp}. The internal meson dynamics is described phemonenologically by introducing relative motion characterized by a quark momentum $\vec{p}$. Since the effects represent a nonperturbative region of QCD, the momentum p cannot be uniquely specified. It is modelled statistically with a gaussian distribution:

$$\phi(|\vec{p}|) = \frac{4}{\sqrt{\pi} P_F^3} \exp(-\frac{|\vec{p}|^2}{P_F^2}), \tag{1.20}$$

where the width P_F is called the Fermi momentum. This parameter must be determined from our data. To satisfy energy-momentum conservation in B-meson decay, the b-quark mass is allowed to vary. It is replaced in Eq. 1.17 with the expression

$$m_b^2 = m_B^2 + m_{q_{sp}}^2 - 2m_B\sqrt{p^2 + m_{sp}^2}. \tag{1.21}$$

In Fig. 1.4a–c we show on an arbitrary scale the electron spectra from the ACCMM model for the three main processes that contribute leptons in $\Upsilon(4S)$ events. In the figure, we used $p_F = 300\,\mathrm{MeV/c}$ for $b \to c\ell\nu$ and $b \to u\ell\nu$ as an example. For $b \to c \to x\ell\nu$, we used $282\,\mathrm{MeV/c}$, as this value was favored by data from a previous experiment [11] (to be described in Chapter 3).

Exclusive Models The exclusive models all assume that B semileptonic decays are saturated by a few resonant final states. After the b-quark decays into a c quark, the c quark recombines with the spectator to form hadrons. Possible final states include the ground state 1^1S_0 (the D meson), the first excited state 1^3S_1 (the D^*), and the higher states such as 1^3P_2, 1^3P_1, 1^3P_0, 1^1P_1, 2^1S_0 and 2^3S_1 (collectively refferred to as D^{**}). The hadronic current J_{had} for the exclusive channels is expressed in terms of form factors. In the case of $b \to c\ell\nu$, for a hadronic current $j_\mu = V_\mu - A_\mu$, they are

$$
\begin{aligned}
< D|A_\mu|\bar{B} > &= 0 & (1.22)\\
< D|V_\mu|\bar{B} > &= f_+(p_B + p_D)_\mu + f_-(p_B - p_D)_\mu & (1.23)\\
< D^*|A_\mu|\bar{B} > &= f\epsilon^*_\mu + a_+(\epsilon^* \cdot p_B)(p_B + p_{D^*})_\mu + a_-(\epsilon^* \cdot p_B)(p_B - p_{D^*})_\mu & (1.24)\\
< D^*|V_\mu|\bar{B} > &= ig\epsilon_{\mu\nu\rho\sigma}\epsilon^{*\nu}(p_B + p_{D^*})^\rho(p_B + p_{D^*})^\sigma. & (1.25)
\end{aligned}
$$

Calculation of these unknown form factors a, f and g varies from model to model. They are generally functions of the 4-momentum transfer (q^2) between the initial- and the final-state mesons. The quantity q^2 in B semileptonic decays is just the mass of the virtual W (virtual, because there is not enough energy to produce a real W boson). The models choose a convenient q^2 to calculate the form factors, and then extrapolate to other q^2 values.

Isgur, Scora, Grinstein and Wise (ISGW) [15] argue that the heaviness of the b quark makes it possible to use nonrelativistic approximations in modelling B-meson decay. At minimum recoil of the final-state meson, or equivalently maximum q^2, the form factors are obtained by solving the Schrödinger equation with a Coulumb plus linear potential for the bound state B,

$$V(r) = -\frac{4\alpha_s}{3r} + c + br, \tag{1.26}$$

where $\alpha_s = 0.5$, $c = -0.84$ GeV and $b = 0.18\,\mathrm{GeV/c^2}$. The q^2 dependence of the form factors F is modelled to be exponential,

$$F(q^2) \propto F(q^2_{max}) \exp(\frac{q^2 - q^2_{max}}{\kappa Q^2}), \tag{1.27}$$

where κ is a parameter introduced to account for relativistic effects. ISGW determined a value $\kappa = 0.7$ from measured pion form factors. The resulting relative fractions of the three B semileptonic decay channels are 27%, 62% and 11% for $D\ell\nu$, $D^*\ell\nu$ and

$D^{**}\ell\nu$ respectively, as is shown in Fig. 1.5. The ISGW prediction for the overall lepton momentum spectrum is also shown in Fig. 1.4.

Other form-factor models also exist, such as the Wirbel-Stech-Bauer (WSB) [16] and the Körner-Schuler (KS) [17] models. The WSB model calculates form factors at minimum q^2 and extrapolates them according to pole dominance. The KS model is particularly designed to study polarizations of the D^* for $B \to D^*\ell\nu$ decays. We choose to use the ISGW model since it is the only model that has included the D^{**} states.

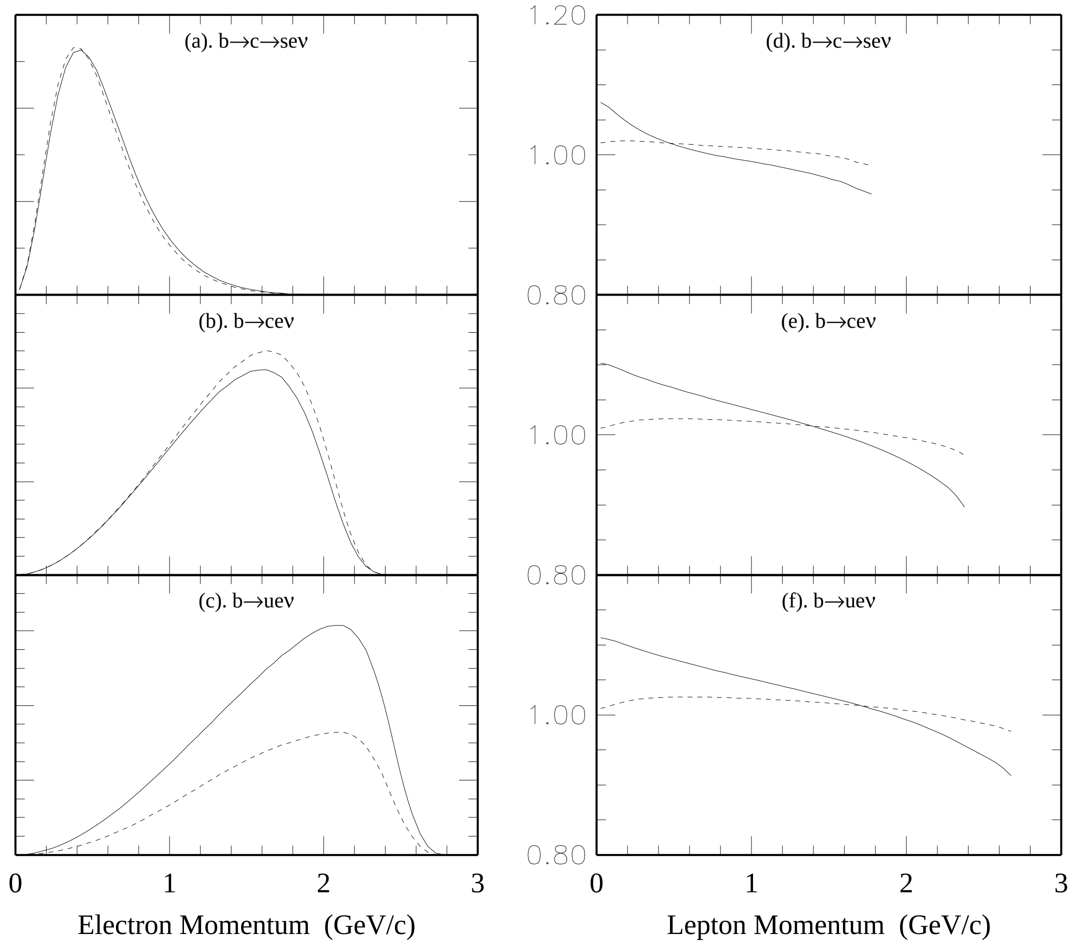

Figure 1.4: Lepton spectra and electroweak radiative corrections. On the left, the ACCMM (solid) and ISGW (dashed) spectra are shown. On the right, relative spectral changes due to electroweak corrections are shown for electrons (solid) and muons (dashed).

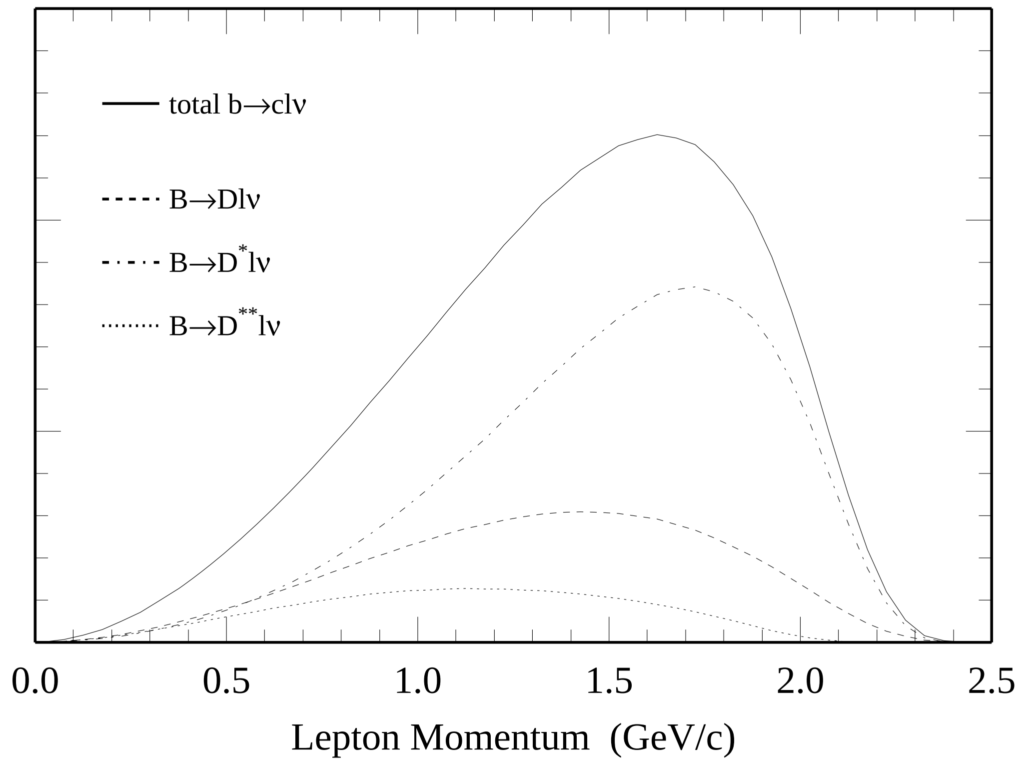

Figure 1.5: Lepton spectra for $b \to c\ell\nu$ in ISGW model.

Recent Theoretical Progress Even though, it is very difficult to calculate B decays from fundamental principles, two important theoretical advancements have been made in the last couple of years: the discovery of heavy quark symmetry, which led to the heavy quark effective theory (HQET) for exclusive decays, and the heavy quark expansion method for inclusive decays.

For a meson made of a heavy quark Q (t, b or c) and a light antiquark $\bar{q}$ (u, d or s), the dynamics is controlled by an SU(3) flavor symmetry and an SU(2) spin symmetry [18]. In the limit that the heavy quarks are infinitely heavy, the light quark and the remainder of the meson behave the same way regardless of the flavor of Q (quark type, either t, b or c), regardless of the spin of Q (spin $+1/2$ or $-1/2$). This is very similar to atomic hydrogen. The orbiting electron does not notice the difference if more neutrons are added into the nucleus or if the nuclear spin is flipped. Based on this symmetry, an effective field theory has been developed. It expresses all of the form factors in terms of a single universal function, called the Isgur-Wise function. This greatly reduces the model dependence of the exclusive calculations, especially for $B \to D^* \ell\nu$, which is used for detemination of $|V_{cb}|$ [19]. The form of this function is not known, and the need to consider several alternative forms introduces some model dependence. Besides, the $B \to D^{**} \ell\nu$ calculations are not yet available, and work is still in progress to correct for the fact that the b and the c quarks are not infinitely heavy. We therefore have to wait until the future to use the full power of HQET in our inclusive analyses.

The heavy quark expansion method also takes advantage of the heaviness of the b quark and the large amount of energy release in $b \to cW$ and $b \to uW$ decays [20]. It is a breakthrough in inclusive heavy quark decay theory. The method is based on expanding the weak transition operator into a series of local operators of increasing dimensions. The coefficients of this series contain increasing powers of $1/m_Q$, similar to a Taylor expansion. With this method it is possible to interpret the ACCMM model at a fundamental level and to go beyond. Its derived lepton spectrum for $b \to cl\nu$, for example, is very close to that from the ACCMM model, which fits data well, as we discuss in Chapter 3. This QCD expansion explains the Fermi motion in terms of kinetic energy. Yet it reveals that the ACCMM modeling of the internal motion is not consistent with QCD, as the momentum distribution of internal motion in QCD should be asymmetric instead of being gaussian. The expansion method is unable to derive this distribution, just as HQET does not itself give rise to the form of the Isgur-Wise function. Approximations must be used, with input from the mass difference of the B^* and B mesons to fix the color magnetic moment of the b quark G_b, and from the mass difference of the B and D mesons to estimate the kinetic energy K_b. Technically, the lepton spectrum derived from this Wilson Operator Product Expansion contains δ functions which diverge near the high momentum end-point region. Even though the theory can calculate the integrated rate in this region, this is difficult to use in fitting data. We therefore did not use it in measuring $\mathcal{B}(B \to X\ell\nu)$. We will, however, use it in calculating the CKM matrix element V_{cb} in Chapter 4 and discuss it in Capter 5 when reviewing the result of our measurements.

1.3.3 Electroweak Radiative Corrections

The last theoretical ingredient of our measurement is the electroweak radiative corrections for the processes we have described. They are calculated to account for higher order effects, similar to those shown in Fig.1.3, except that this time the loop lines are for electroweak gauge bosons γ and Z^0 instead of gluons. This is a second order effect, supressed by g_1^2 and g_2^2, but it amounts to a few percent, and is very important due to the precision nature of our measurement. One requirement of flavor symmetry is lepton universality. In our case, the measured electron and muon branching fractions must be consistent. With the high statistics of our data sample, this correction must be implemented to demonstrate lepton universality.

Atwood and Marciano [21] calculated the three main effects of this type: virtual loops at higher energies; Coulomb interaction for the initial meson if it is neutral, such as B^0 or D^0; and low energy bremsstrahlung. The first two change the total decay rate or normalization, and only the last changes the shape of lepton spectrum for $X \to Y\ell\nu$. In our measurement described in Chapter 3, we use the lepton spectral shapes from theoretical models to fit the data. The fitted normalization gives the branching fraction. So only the third correction, internal bremsstrahlung, affects our measurement.

Although the calcuation itself is complicated, it is easily implemented in our analyses. The correction can be simply expressed by [11]

$$\mathrm{EWcor} = (\frac{E_{max} - E_l}{CE_l})^r \, , \tag{1.28}$$

in which

$$r = \frac{2\alpha}{\pi}\left[\ln(\frac{2E_l}{m_l}) - 1\right] . \tag{1.29}$$

In these equations the m_l and E_l are lepton mass and energy, C is a factor that changes the shape of the spectrum, but not the normalization, which is specified in terms of the maximum and average energies of the lepton spectrum

$$C = \frac{E_{max} - \bar{E}_l}{\bar{E}_l}. \tag{1.30}$$

This correction introduces a 2-10% difference in the spectrum for muons and electrons, depending on the momentum, as is illustrated in Fig. 1.4 by the solid and dashed curves for electrons and muons, respectively.

1.4 Experimental Techniques and Objectives

In this last section, we outline how the measurements of semileptonic B decay have been carried out, including the production of B mesons in the laboratory, and the techniques we used in detecting the decays.

1.4.1 Production of B Mesons

Our sample of B mesons has been obtained with the Cornell Electron Storage Ring CESR, and studied with the CLEO-II detector. The production mechanism is electron-positron annihilation through the $\Upsilon(4S)$ resonance: $e^+e^- \to \gamma^* \to \Upsilon(4S) \to B\bar{B}$, where the γ^* represent a virtual photon. As is shown schematically in Fig. 1.6, CESR has three main components. A linear accelerator (linac) uses a continuous line of small radio frequency cavities to accelerate electrons emitted from an electron gun cathode to approximately 200 MeV. It can also produce positrons, when its electron beam is directed at a tungsten target, and the resulting positrons are collected and themselves accelerated to 200 MeV. The electrons and positrons are injected into the synchrotron for acceleration to approximately 5 GeV. In the synchrotron the e^+ and e^- beams are accelerated by the same few megawatt RF cavities as they travel in circular orbits in a high vacuum chamber. A periodic arrangement of dipole and quadrupole magnets keep the electrons in their orbits, confined within small well formed bunches. After they achieve full energy the bunches are transferred to the storage ring, which shares the synchrotron underground tunnel. The storage ring functions in much the same way as the synchrotron, except that its RF system primarily restores the energy lost to synchrotron radiation, and its extremely good vacuum and optics allow stored beams to be maintained for several hours.

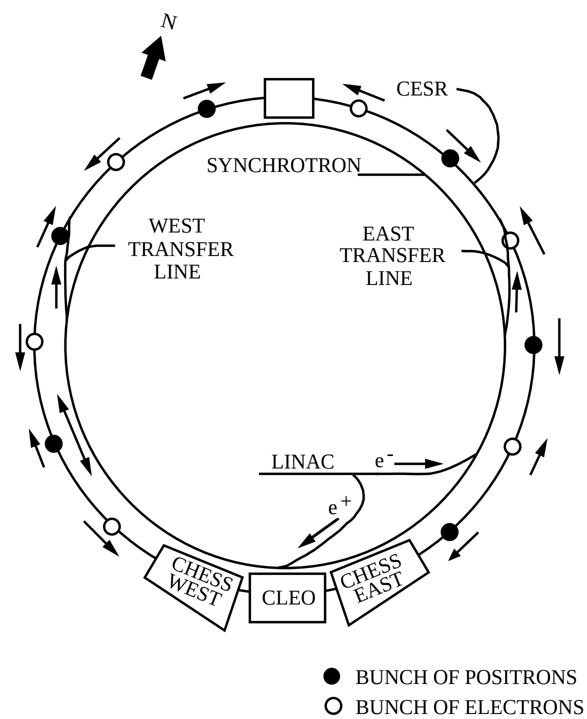

Figure 1.6: The Cornell Electron Storage Ring.

The typical stored beam in CESR represents a current of about 100mA. The bunches are roughly the size of a flattened needle ($0.01mm \times 0.1mm \times 1.0mm$ in the horizontal, vertical and the beam motion directions). Filling the machine takes 10–30 minutes in normal operation and each “fill” lasts approximately one hour.

The bunches of e^+ and e^- circulating in the storage ring are then brought into collision once every revolution at the interaction point in the center of the CLEO detector. The detector electronically collects information about the debris of the collisions, conducts online analyses, and stores the data for subsequent detailed analyses. By repeating this procedure, millions of B events have been recorded, providing a huge data sample for B physics analyses.

The rate of e^+ e^- collision is described by the peak luminosity defined as [22]

$$\mathcal{L} = nf\frac{N(e^+)N(e^-)}{A(e^+e^-)} \tag{1.31}$$

where $N \approx 10^{11}$ is the number of electrons/positrons in a bunch and $A(e^+e^-) \approx 5 \times 10^{-4} cm^2$ is the effective area of the beams. The number of bunches n was 7 for most of the data runs we used, and 9 for the rest. The orbital frequency for the electron and positron bunches in CESR is $f \approx 400$ kHz. Typical peak luminosity at CESR during this period of operation was $\mathcal{L} = (1-3) \times 10^{32} cm^{-2} s^{-1}$. The integrated luminosity over time determines the total number of events collected for any process. For example, the number of multihadron events is given by $N_{had} = \sigma \int \mathcal{L} dt$, where σ is the cross section of the reaction (unit is barn, $1\,b = (10^{-12} cm)^2$).

The hadronic cross section in the e^+e^- annihilation energy region near 10 GeV is shown in Fig. 1.7. At a center-of-mass energy of 10.58 GeV, the total hadronic cross section is about 4 nb where one quarter is due to resonant production of the $b\bar{b}$ bound state Υ(4S) and the remaining 3 nb is due to "continuum" production of lighter quarks. A data sample with an integrated luminosity of $1/fb$, for instance, contains about one million Υ(4S) decays to $B\bar{B}$ pairs. In order to estimate the continuum contamination from the other 3 million events, we also collect data at a lower energy, about 60 MeV below the Υ(4S). As this energy is about 30 MeV below the production threshold of $B\bar{B}$ pairs ($m(B) = 5.280\,\mathrm{MeV/c^2}$), no B mesons are produced. It thus provides a good estimate of the continuum contribution underneath the Υ(4S) peak to any process of interest. In the following context, we call the data samples collected on the Υ(4S) the "ON" samples, and those collected 60 MeV below the resonance the "OFF" samples.

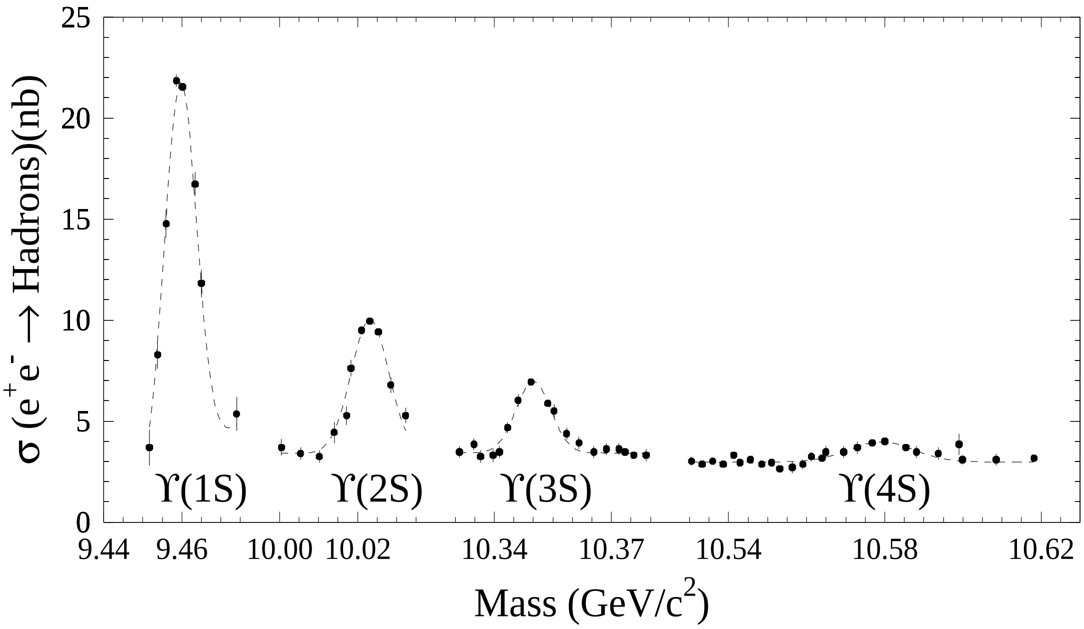

Figure 1.7: The Υ resonance states.

1.4.2 Objectives of the Measurements

The objective of our measurement is to count the number of leptons from B decays and the number of B events. We interpret the ratio of the two as the semileptonic branching fraction of the B mesons. If the $\Upsilon(4S)$ meson decays only to $B\bar{B}$ pairs, the denominator is simply the number of $\Upsilon(4S)$ events, determined by integrated luminosity and cross section, as was described in the previous section. The numerator would be the number of detected leptons if only B mesons give rise to leptons at the $\Upsilon(4S)$. Unfortunately, the D mesons produced in B decays can also decay semileptonically, contributing to the leptons collected. We name semileptonic decays of the B "primary" and those of the D "secondary". Our goal is to measure the portion of primary leptons in $\Upsilon(4S)$ events by separating the primary spectra $b \to c\ell\nu$ and $b \to u\ell\nu$ from the secondary $b \to c \to x\ell\nu$.

In our first analysis, described in Chapter 3, we separate the primary from the secondary with the help of theoretical models. As is shown in Fig. 1.4, the primary and secondary lepton spectra have distinctive shapes and dominate the higher and lower momentum regions, respectively. By fitting the inclusive lepton spectra with predicted spectral shapes from models, we can use the overal normalization to measure the B semileptonic branching fraction in a model-dependent way.

In our second analysis, described in Chapter 4, we use an additional high momentum lepton as a tag of the decay of the second B meson in the event. This ensures that the denominator in the branching ratio calculation is the number of B mesons in our sample. Taking advantage of charge and kinematic correlations of leptons from the two B mesons, we separate the primary lepton spectrum from that of the secondary. By integrating over the primary spectrum we obtain the numerator. The B semileptonic branching fraction is therefore measured by experimental means, without having to rely on theoretical models.

Chapter 2

Lepton Detection

Overview: We briefly review the CLEO-II detector in this chapter and describe the lepton identification used in our analyses.

2.1 Objectives of the Detector

The B mesons decay within a few picoseconds after they are produced in CESR. Among the possible decay products, the charged particles $e^{\pm}$, $\mu^{\pm}$, $\pi^{\pm}$, $K^{\pm}$, p and $\bar{p}$, and the neutral particle γ are directly detectable through their interactions with detector material. The other particles either can not be easily detected (for example, ν, n and K_L^0), or like the B's they decay too quickly to be observed. Among these latter particles are the charmed mesons ($D^{\pm}$, D^0, $\bar{D}^0$, $D_s^{\pm}$), many other mesons and baryons ($\Lambda_c^{\pm}$, J/ψ, π^0, K_s^0, $\Lambda^{\pm}$, ϕ, ρ, *etc.*) and the $\tau^{\pm}$ lepton. Although these particles are not directly detectable, their production can be inferred from the information about the detected particles in an event. The J/ψ, for example, decays to $\mu^+\mu^-$ or e^+e^-, each about 6% of the time. These leptons are particularly important, because they contribute to the background of our measurements. We can recognize and suppress this background by computing the effective mass of the detected lepton pairs, and identifying as likely J/ψ

decay products those pairs which are near the known mass. Even the B meson itself can be reconstructed from many different decay channels, ranging from the relatively favored modes such as $B \to D^{*}\pi$ or $B \to J/\psi K$, to the rare decays $\bar{B}^{0} \to K^{-}\pi^{+}$, $\bar{B}^{0} \to \pi^{+}\pi^{-}$ and $B \to K^{*}\gamma$.

CLEO II is a general-purpose magnetic spectrometer [23]. Its primary objectives are the detection of $e^{\pm}$, $\mu^{\pm}$, $\pi^{\pm}$, $K^{\pm}$, p, $\bar{p}$, and γ. The specific information we would like to obtain include all of the following: (1) position measurement (trajectory reconstruction); (2) momentum measurement; (3) energy measurement; (4) identity among the possible types of detectable particles listed above. To obtain as complete a picture of the event as possible, we would like to accomplish these tasks with maximum solid angle coverage, and good efficiency. The CLEO-II detector achieves these goals within technological and economic constraints.

2.2 The CLEO-II Detector

CLEO-II is made of the following components (shown in Fig. 2.1 and 2.2): central tracking detectors (CD), time-of-flight scintilators (TF), and crystal calorimeters (CC). All of these components reside inside a 1.5-Tesla magnetic field provided by a superconducting solenoidal magnet. Outside the magnetic field the only active components are the muon detectors (MU). We discuss the principles and some technical details of these components in succeeding subsections. Briefly, the tracking chambers inside the magnetic field measure the momenta of $e^{\pm}$, $\mu^{\pm}$, $\pi^{\pm}$, $K^{\pm}$, p and $\bar{p}$, and distinguish the positively charged from the negative. The inner chambers also provide information about the origin, or vertex, of these charged particles. The calorimeter simultaneously measures the energy deposit and the position for photons and charged particles. Complicated particle identification involves essentially all elements of the detector.

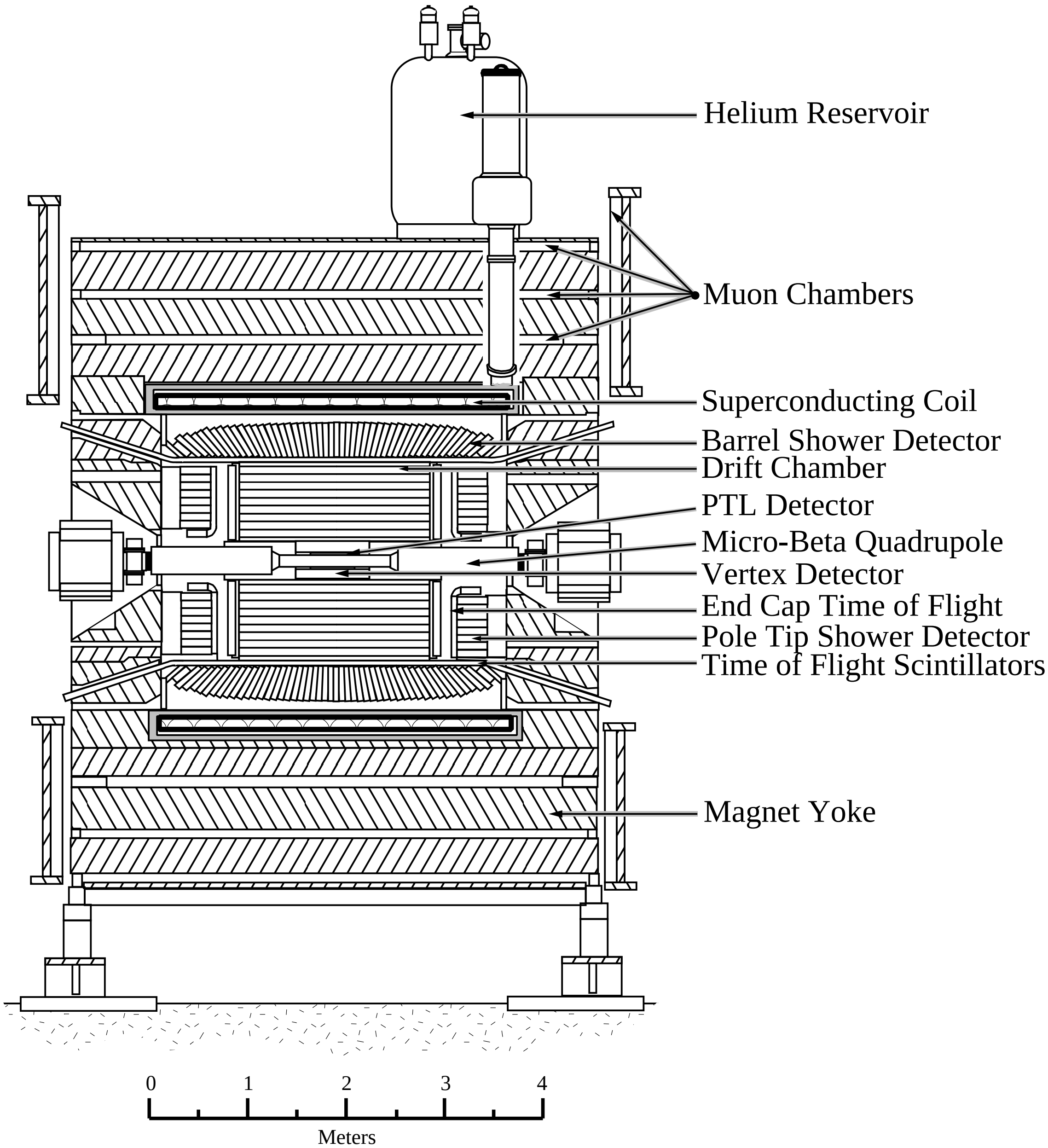

Figure 2.1: CLEO-II detector side view.

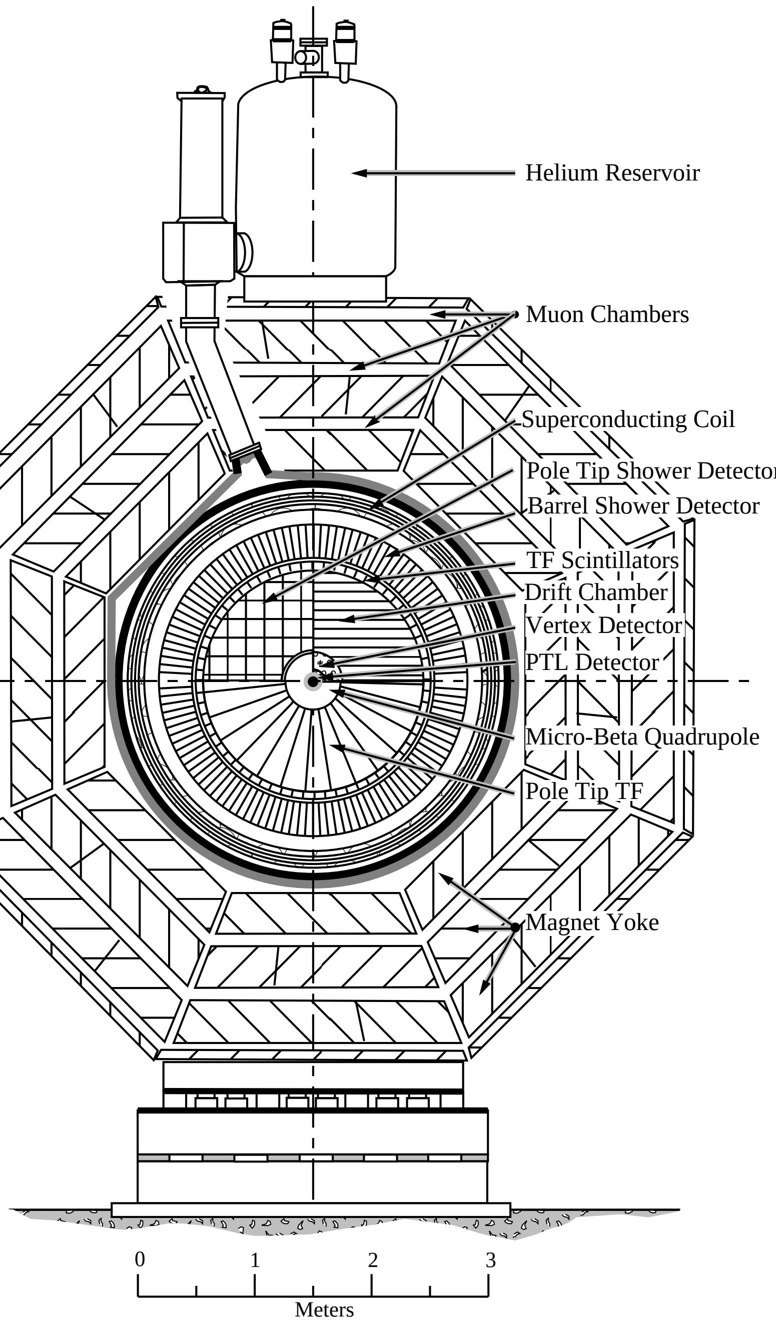

Figure 2.2: CLEO-II detector end view.

2.2.1 Tracking

Charged particles are detected by the central tracking chambers: PT (the precision tracker), VD (the vertex detector), and DR (the outter drift chamber). The particle trajectories through these devices are helical, because of the 1.5-Tesla magnetic field. When a charged particle travels through a volume of gas, it ionizes gas atoms, thus leaving a trail of electrons and ions — a track in the gas. All the three chambers work by collecting and amplifying this ionization. Take the DR as an example. It is a cylindrical volume (radius 1m, length 2m) filled with a gas mixture of Argon (50%) and Ethane (50%). Thousands of $20\mu m$ gold-plated tungsten sense and anode wires are stretched along the axis of the cylinder, and applied with a potential of a few thousand volts. The free electrons from ionization drift forward to the nearest anode. As they gain energy in the electric field of the anode wire and the surrounding field-shaping wires, secondary ionization occurs and a detectable "avalanche" forms. The resulting electronic pulse is detected by electronics at both ends of the wires. If the pulse is large enough, it is called a "hit". When viewed from the end of the cylinder, as shown in Fig. 2.3, a track is a sequence of consecutive hits in the $r-\phi$ plane, where z is along the axis of the cylinder.

When the magnetic field along the z axis is applied, charged particles are bent in the $r-\phi$ plane by the Lorentz force. The clockwise or counterclockwise bending of the track naturally tells its charge. The radius of its curvature is the measure of its momentum p_t transverse to the beam axis. There is no bending in the $r-z$ plane, so the direction (the polar angle θ with respect to the z-axis), combined with p_t, provide a measurement of the magnetude of the momentum. The determination of θ involves three techniques. (1) Every sixth layer of sense wires is inclined at a small angle $(3-7^o)$ with respect to the z-axis. The hit position in the $r-\phi$ plane is slightly different from what would be observed in an axial layer. The resulting "small-angle stereo" effect provides the z information needed. (2) On the inner and outer DR and VD walls, cathode strips are wrapped around along the ϕ direction. The signal induced on a strip by nearby ionization tells the z position of a track going through that wall. (3) The pulses produced on a wire by a particle-induced avalanche travel to both ends of the wire. The relative sizes of charge signals collected at the two ends can also be used to obtain information about the z position of the track on this wire. This effect is used in the VD.

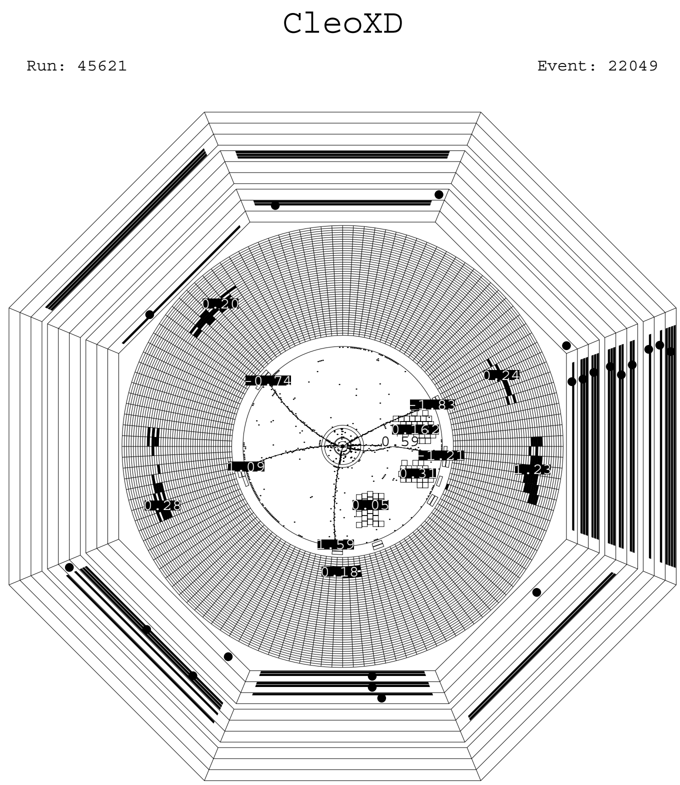

Figure 2.3: An event display viewed from end.

The geometry and potential of the sense and field wire are designed to to make the electric field as uniform as possible so that there is a simple connection between the measured elapsed time and the position in the cell. To make an accurate measurement of the trajectory, these position measurements must be as precise as possible, and there must be a large number of space points. In total, we have 51 layers of wires in the DR, 16 in the VD and 6 in the PT. The inner two chambers also provide information about where a track originates. This information is necessary to reconstruct vertices — where a short-lived particle decayed to charged tracks, such as $K_s^0 \to \pi^+\pi^-$ and $\Lambda \to p\pi^-$.

Two factors determine the tracking resolution, in addition to the intrinsic uncertainty in the position measurements. At low momenta, the track hits only a small number of layers. This reduces the precision of the curvature measurement. At higher momenta the curve is distorted from a helix (circle in $r - \phi$) by multiple scattering of the charged particle with material in the chambers, including gases, wires and walls. The momentum resolution is approximately modelled as

$$(\delta p/p)^2 = (0.0011 p_t)^2 + (0.0067)^2 \tag{2.1}$$

for p in GeV/c. For tracks at 5 GeV/c, this is fairly close to the measured value $\delta p \approx 65$ MeV/c. The angular resolution is $\delta\phi \approx 1$ mrad and $\delta\theta \approx 4$ mrad. The bigger $\delta\theta$ is expected, as there is only one stereo layer for every five axial layers. These tracking resolutions serve our experiment very well. Right now, the PT is being upgraded to a 3-layer double-sided silicon vertex detector that will improve the vertex position resolution.

2.2.2 Calorimetry

The calorimeter records the passage of charged particles, and measures the energy of photons and electrons in the CLEO-II detector. When a photon is incident on a block of material three processes can occur. If the photon energy E_γ is low, up to approximately 100 KeV, production of photoelectrons from the atoms of the material dominates. As E_γ goes higher, Compton scattering of the photon with atomic electrons takes over. Once E_γ passes the threshold of $2m_e \approx 1.02$ MeV, e^+e^- pair creation from the interaction of the photon with the material nuclei becomes the main process. At our energy scale typical photon energies are in the range 10 MeV – 5 GeV, so the photons immediately produce e^+e^- pairs. The electrons and positrons in turn undergo bremsstrahlung leading to a "shower" of particles, until the energy is totally dissipated in the material. At CLEO, we use cesium iodide (CsI) crystals doped with thallium as the calorimeter material. The light produced by scintillation caused by the many electrons and positrons in the shower can be collected as a measure of the energy of the incident particle. The 30 cm depth of crystals is about 17 radiation lengths. This ensures that nearly all of the energy of electrons and photons in our 5 GeV range is deposited in the calorimeter.

Muons have a much smaller cross section in material than electrons and hadrons. Typically only 100-200 MeV is lost through electromagnetic interactions in the calorimeter. The electromagnetic energy loss for charged hadrons, π, K, p and $\bar{p}$, is similar. Sometimes, these hadrons will initiate a hadronic shower when they undergo nuclear interactions with the crystal nuclei. It is rare even in this case, however, for hadrons to deposit all of their energy in the calorimeter, except low-energy $\bar{p}$'s, which annhilate with protons in the crystal and leave an excess of energy. This is one of the backgrounds in our electron identification.

The 7800 invidual CsI crystals ($5cm \times 5cm \times 30cm$) in the CLEO-II calorimeter provide energy resolution which is unequaled among general purpose detectors, about 1.5% at 5 GeV and 3.8% at 100 MeV for the best part of the acceptance (barrel region). In the endcap region it is slightly worse, about 2.6% at 5 GeV and 5% at 100 MeV, due to the amount of material between the calorimeter and tracking chambers. The fine granularity also gives good position resolution for showers, which is vital for electron identification and π^0 reconstruction. In the barrel region, $\delta\phi \approx 3 - 5\,\mathrm{mrad}$, and $\delta\theta \approx 2.5 - 4\,\mathrm{mrad}$. The angular resolution is slightly worse in the endcap region, and the detailed performance depends on the energy of the shower.

2.2.3 Hadron Identification

Identifying charged hadron species ($\pi^{\pm}$, $K^{\pm}$ and $p/\bar{p}$) has been one of the most difficult challenges in collider experiments. In the current CLEO-II detector, two components are used for particle identification, the time-of-flight detector (TF) and drift chamber measurement of the rate of energy loss due to ionization (dE/dx).

The time-of-flight detector measures the time interval between a beam crossing and when the particle strikes the outer shell of the drift chamber. It consists of strips of plastic scintilators in the barrel, and pie-shaped pieces in the endcap. The beam crossing is timed by two "beam buttons" at the ends of the interaction region near the beam pipe. These register a small induced electric pulse when the electron and positron beams pass. When a particle strikes the TF detector, the plastic scintilates. The flight time is determined from the time that the light output is collected by photomultipliers at both ends of the scintilator, with corrections for propagation delay and other factors. For our barrel TF system, the resolution varies from 139 ps for 5 GeV electrons to 155 ps for pions in hadronic events.

Knowing the arc length of a track in CD, the time of flight can be determined as the reciprocal of the velocity of the particle $1/\beta$. At the same momentum, p, K and π have different masses and thus different velocities. As shown in Fig. 2.4, their $1/\beta$ distributions give good separation of the three species below 1.5 GeV/c. The separation is poor at higher momenta, as the particles become highly relativistic. In short, the combination of momentum and velocity of a charged track provides a meaurement of its mass.

The second technique in particle identification is the measurement of dE/dx by the outer drift chamber. When a charged particle goes through the tracking chamber gas, it loses a small amount of energy to ionize the gas atoms. The energy loss per unit distance is a function of the particle mass, as is illustrated in Fig. 2.4. The separation of p, K and π is generally good below 0.8–1.2 GeV/c.

Combining the two constraints on particle mass results in adequate identification of p, K and π below 1.5 GeV/c. Above that the present CLEO-II detector is incapable of separating K and π. Such separation would be very useful, for example, in

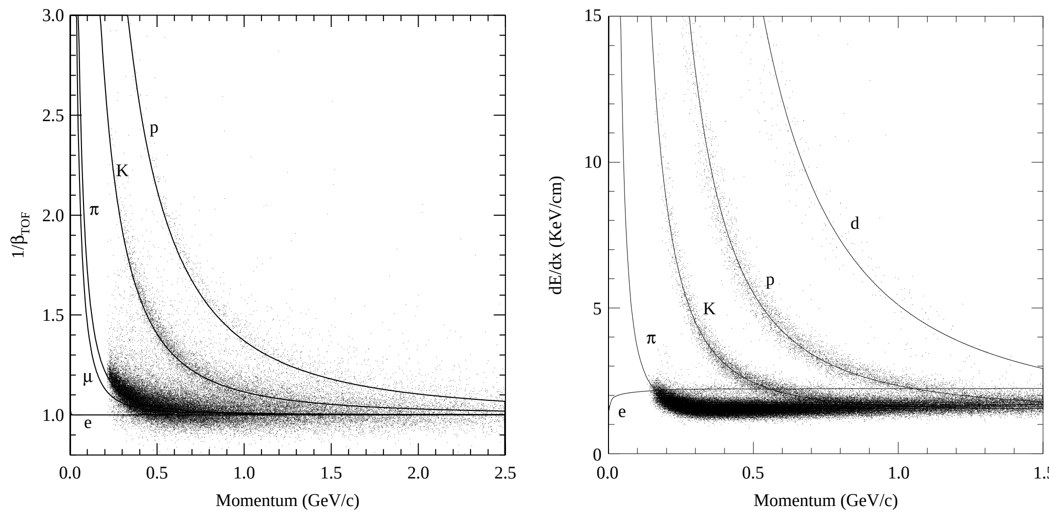

Figure 2.4: Time-of-Flight and dE/dx distributions.

distinguishing the important decay channels $B \to K\pi$ and $B \to \pi\pi$. Improved particle identification using Cerenkov light is a hope for a future CLEO upgrade.

2.2.4 Data Taking and Simulation

CESR beams cross once every 2.5 μs, a rate of 400 kHz. Interesting collision reactions do not happen on every crossing, and our data acquisition system can only read in about 40–50 events per second. These two factors require us to filter online to reduce the event rate from 400 kHz to 40 Hz by selectively triggering the electronics when there are reactions we are interested in. The criteria used include energy deposition in the CC, hits in the TF, track segments in the CD and inner chambers, and hits in the MU. Once an interesting reaction triggers the read-out electronics, the data acquisition system digitizes all electronic channels connected to the hits in the detector components. The digital records of this "event" are analyzed online, and subsequently written on tapes for more detailed off-line analysis. On average, we collect $300 - 500\ nb^{-1}$ for each beam fill, corresponding to about an hour and a half. Since we run the accelerator in excess of 200 days per year, this results in an annual data sample of $1000 - 2000\ pb^{-1}$.

In order to estimate the detection efficiencies and backgrounds, Monte Carlo simulations of data are systematically produced in parallel with data taking. This usually involves three steps. First, a physics generator (QQ), produces interesting particle reactions and generates final state particles in an event, for example $e^+e^- \to \Upsilon(4S) \to B\bar{B}$ and $B \to X\ell\nu$. Second, the generated particles are put through a simulated detector by the CLEO GEANT Monte Carlo package CLEOG. This simulates all the interactions of the particles with detector material, such as ionization in CD gas, and electromagnetic showering in the CC. The output of CLEOG is almost identical to the raw data we collected in real data taking runs. Finally, the simulated data are processed in the same way as e^+e^- annihilation data were through the data compressing program PASS2. So now, knowing the input to QQ and output of PASS2 on our Monte Carlo, we can calculate the efficiencies and study background contributions. More detail on efficiency and background determination will be discussed in Chapters 3 and 4.

2.3 Lepton Identification

The remainder of this chapter discusses the lepton-identification methods as well as their efficiencies and misidentification probabilities. This is the most crucial aspect of the detector performance for this thesis, since our analyses involve mostly leptons.

2.3.1 Muon Identificaion

Muon identification [24] is performed by the outermost part of CLEO II — the muon detector (MU). It takes advantage of the fact that $e^\pm$ deposit nearly all of their energy in the calorimeter, and $\pi^\pm$, $K^\pm$, p and $\bar{p}$ experience nuclear interactions in the calorimeter and flux return iron surrounding the magnet. The muon detector consists of three layers of proportional wire chambers embedded in the iron absorbers at thickness of 36, 72 and 108 cm. The iron thickness are roughly equivalent to 3, 5 and 7 nuclear absorption lengths. In the endcap region, there is only one layer of chambers, installed at a depth of roughly 7 absorption lengths. The three layers of chambers provide the detector with flexibility. Depending on the need of a specific measurement, one can maximize efficiency at the expense of higher background (depth 3), maximize purity at the expense of efficiency (depth 7), or strike a compromise (depth 5). Each of the three chamber layers contains three wire layers, providing a level of redundancy which ensures high detection efficiency. The wires in the rectangular MU cells are stretched along the z direction, similar to the those in the CD. A hit therefore clearly marks the coordinates in the $r - \phi$ projection. The z position is derived from the induced current in copper strips aligned perpendicularly with respect to the wires, and also from charge division at both ends of each wire hit.

The identification procedure has two steps. First, each charged track in the CD is extrapolated into the muon chambers. Then a search is made in the muon chambers to see if there are hits within a few centimeters of the track projection. For our measurement of semileptonic B decays, we require that a muon candidate have hits at a depth of at least 5 absorption lengths. We restrict our sample to the barrel region, which covers $|\cos(\theta)| < 0.61$. In this region we have all three layers of chambers, with a well understood acceptance and efficiency. The rest of the MU, in the polar angle range $|\cos(\theta)| = 0.61$ to 0.88, is less well understood and less appropriate for precision studies.

2.3.2 Electron Identificaion

The electron identification package [25] combines information from different parts of the detector to calculate a likelihood ratio:

$$\texttt{R2ELEC} = \sum_i \ln(P_e/P_h)_i \tag{2.2}$$

where i represents the several information sources used. These include the ratio of the CC energy deposit to the measured momentum (E/p), dE/dx, track-shower matching, shower shape, and TF information. P_e and P_h are the probabilities of a charged track being identified as an electron or hadron based on that source i. They are determined from a data sample of pure electrons from Bhabha events ($e^+e^- \to e^+e^-$) and a pure sample of hadrons from $\Upsilon(1S)$ decays. The electron and hadron samples have distinctive distributions for each one of the sources we use in electron identification. E/p, for example, shows a narrow disribution near 1 for electrons. For hadrons, E/p is most often small, with a large tail corresponding to hadronic showers. This is the principal tool we have to discriminate electrons from hadrons. The second most powerful handle is dE/dx. As shown in Fig. 2.4, there is separation of electrons from hadrons at lower energies. The showers caused by hadrons are in general more widely distributed than electron showers, which are narrowly contained in a few crystals. Additional information which contribute to the disciminating power of `R2ELEC` is obtained from several sources. Some TF information is included, simple cuts on the time of flight which help reject $K^\pm$ at lower energies. Based on our studies of the efficiencies and background discrimination of our electron identification package, we have standardized our `R2ELEC` selection criteria. In the barrel region $|\theta| = 45 - 90^o$, we require `R2ELEC` > 3.0 for an electron candidate.

2.3.3 Efficiencies

The efficiency for muon identification is determined by the chamber efficiencies and the momentum-dependent energy loss experienced by muons in the material in front of each chamber (mainly iron absorber). Our Monte Carlo simulates the chamber efficiency for each layer to within $\pm 1\%$. The energy loss in the material is more difficult, but is now understood at a level of 10 MeV [26]. We plot the Monte Carlo muon identifcation efficiencies in Fig. 2.5. Overall, the MC simulation provides excellent agreement with data in muon efficiency, with an estimated systematic error of less than 2%.

Measuring the efficiency of electron identification is a difficult task. We choose tracks from radiative Bhabha events in data and embed them into hadronic events from data to assess electron identification in the evironment of $B\bar{B}$ events. The measured efficiencies for embedded tracks are shown in Fig. 2.5. They are generally above 90%. The systematic error in this efficiency has been estimated to be $\pm 2\%$ from the difference of the efficiencies before and after embedding.

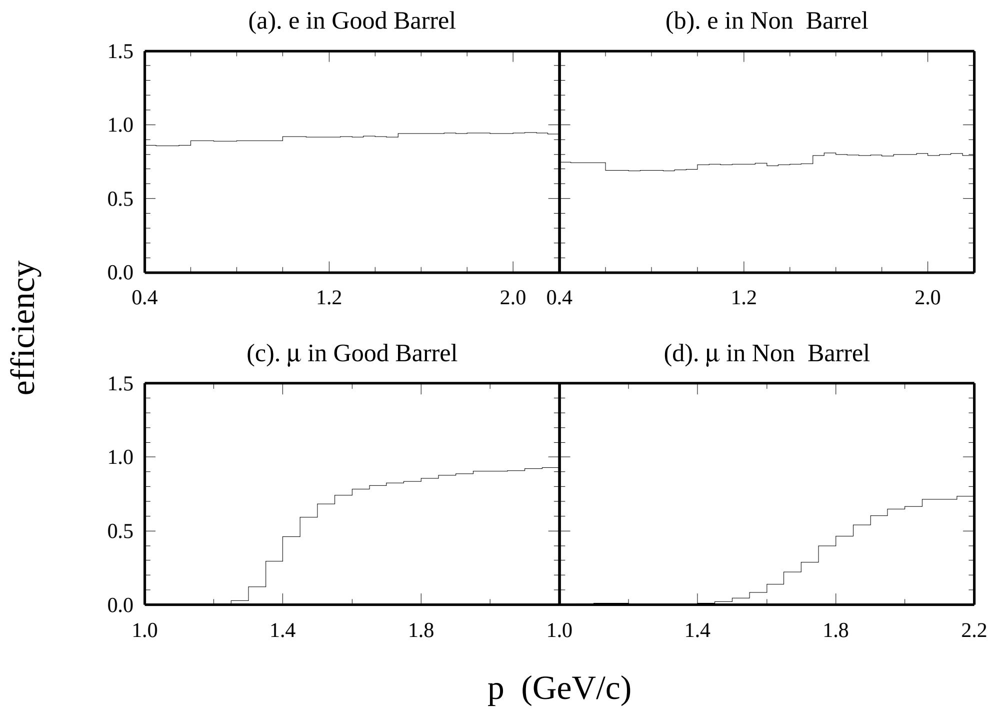

Figure 2.5: Lepton identification efficiencies.

2.3.4 Fake Rates

Fakes are hadronic tracks misidentified as leptons. Fake rates are the probabilities of misidentification. They are generally momentum and charge dependent. To determine the average misidentification probability for tracks from $\Upsilon(4S)$ decays, we need to know the individual misidentification probabilities for pions, kaons and protons, and their abundances. The appropriate fake rate can thus be expressed by the following weighted sums:

$$f_\ell^{\pm}(\vec{p}) = \sum_{i=p,K,\pi} Y_i^{\pm}(\vec{p}) \cdot f_i^{\ell\pm}(\vec{p}) \tag{2.3}$$

where Y_i is the fractional abundance of particle i, and $f_i^{\ell\pm}$ is the probability of $i^\pm$ being misidentified as $\ell^\pm$.

Pure p, $\bar{p}$, $K^\pm$ and $\pi^\pm$ samples are first selected from data by using specific decay processes which provide these particles. The individual fake probabilities are then determined by running lepton identification on these hadronic tracks. The cuts we use in selecting the hadron samples are listed in Appendix B. Briefly, we identify protons from $\Lambda \to p\pi$ secondary-decay vertices using the vertex finder. From the combined ON and OFF data samples 43,000 p and $\bar{p}$ were selected. The candidate mass peak, Fig. B.1a, demonstrates that the sample of Λ candidates has a negligible contamination. The p and $\bar{p}$ fake probabilities as functions of momentum are shown in Figs. B.2a and B.2b. The peak for $f_{\bar{p}}^{e^-}$ around 1.2 GeV/c for $\bar{p}$ is due to the crossing of the electron and proton dE/dx bands, together with the large E/p values which can result from $\bar{p}$ annihilations in the calorimeter.

Pions are selected by the vertex finder from the secondary vertices of $K_s^0 \to \pi^+\pi^-$. Our sample includes about 390,000 K_s^0 with very good purity, as indicated by the mass peak in Fig. B.1b. The pion fake probabilities are shown in Figs. B.2e and f.

We select charged kaons from the decay chain $D^{*\pm} \to D^0\pi^\pm, D^0 \to K^\mp\pi^\pm$. By cutting on the $D^{*+} - D^0$ mass difference and then applying cuts to the resulting D^0 mass peak, we obtain a sample of 14,000 kaons with a small contamination due to random combinations, as is shown in Fig. B.1c. The kaon fake probabilities are shown in Fig. B.2c and B.2d.

The above fake probabilities of p, K and π are then combined together, using the measured abundances for the $\Upsilon(4S)$ [27], which are shown in Fig. B.3. In Fig. 2.6 we show the resulting fake rates as a function of momentum with the dots and error bars. The size of the error bars clearly reflects the low efficiency for selecting kaons. While this procedure in principle offers the best estimate of the fake rates, in practice it is limited by our ability to obtain large pure samples of tagged hadrons. As an alternative,

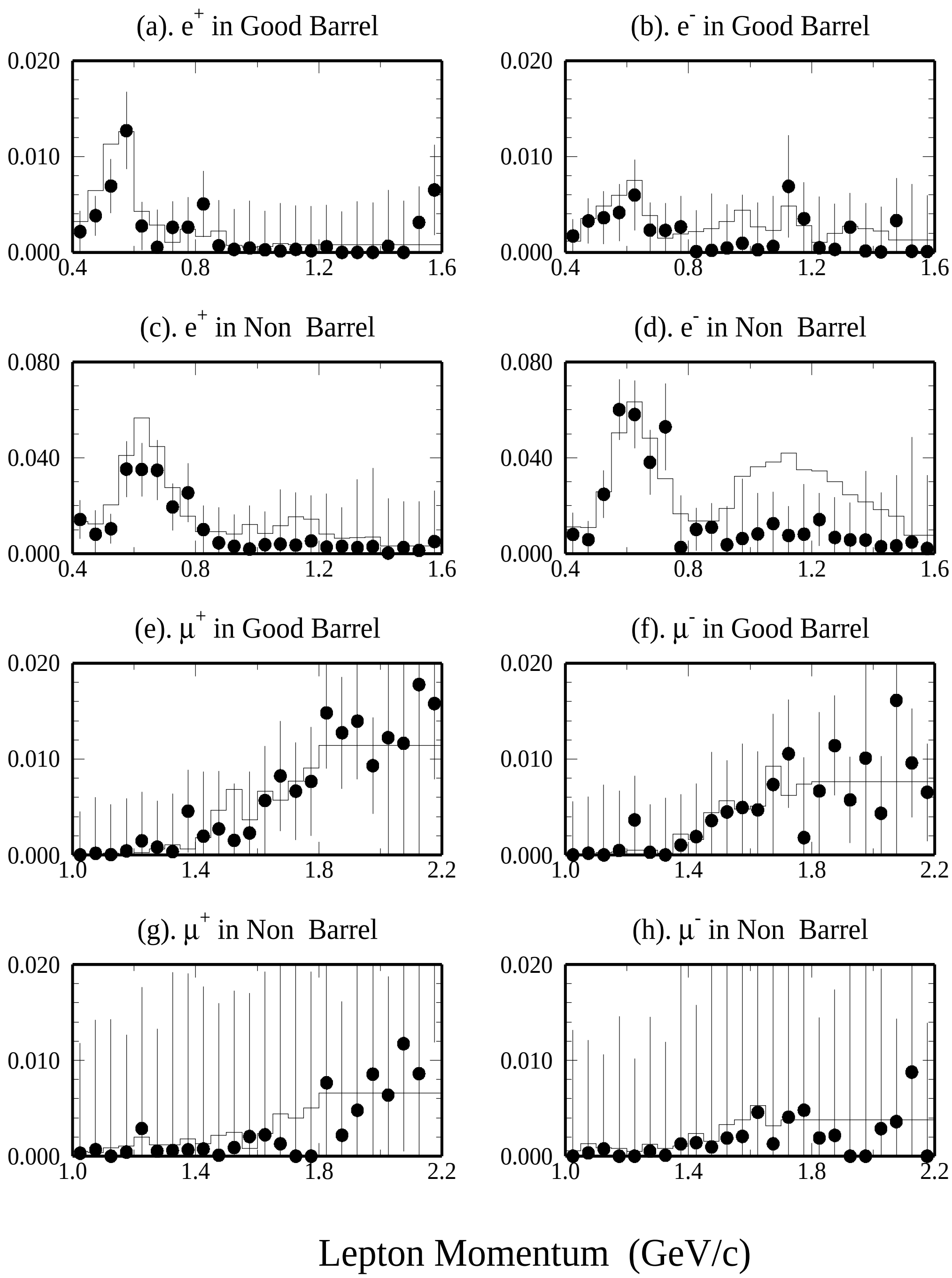

Figure 2.6: Lepton fake rates from $\Upsilon(1S)$ data (histograms) and $\Upsilon(4S)$ data (dots).

we chose to evaluate our fake rates by using a data sample collected at the $\Upsilon(1S)$.

Unlike the $\Upsilon(4S)$, hadronic decays of the $\Upsilon(1S)$ are not expected to produce leptons. Therefore fake rates can be calculated simply by counting tracks which are selected by the lepton identification packages. The high cross section at the $\Upsilon(1S)$ makes this procedure feasible even with a limited $\Upsilon(1S)$ data sample. We expect that the only source of real leptons is from the decay $\Upsilon(1S) \to \gamma^* \to q\bar{q}$. These single virtual photon processes represent the same physics as the continuum, and contribute a calculable enhancement to the usual continuum rate. We can remove this source of real leptons together with the continuum contribution by using our OFF data sample. The appropriate luminosity scale factor is as follows:

$$\alpha_{\mathcal{L}}(1S) = \frac{\int \mathcal{L}(1S)dt}{\int \mathcal{L}(OFF)dt} \frac{E^2_{beam}(OFF)}{E^2_{beam}(1S)}(1+r)\,, \tag{2.4}$$

where the "over-subtraction" factor $r = 0.52 \pm 0.04$ is calculated in Appendix C.

Other lepton contributions from $\Upsilon(1S)$ decays include electrons from converted photons in the beampipe and in the material between the tracking devices, electrons from π^0 Dalitz decays and lepton pairs from J/ψ decays. These are all corrected in the $\Upsilon(1S)$ fake-rate study by using methods identical to those we describe in Chapters 3 and 4.

The lepton identification fake rates from the $\Upsilon(1S)$ are illustrated as the histograms in Fig. 2.6. The overlaying of the $\Upsilon(4S)$ fake rates on these plots clearly shows both the agreement and the lack of statistics for the $\Upsilon(4S)$ study. We have chosen to use the $\Upsilon(1S)$ fake rates in this analysis. We estimate the systematic errors from the difference between the $\Upsilon(1S)$ and $\Upsilon(4S)$ measurements.

Conclusion: The basic ideas and techniques in our experiment have been introduced. In the next two chapters we discuss the two measurements in detail. As CLEO terminology can not be easily avoided, we use `typewriter` style to distinguish them. They can be looked up from Appendix A for reference, though they will in most cases be explained when they first appear.

Chapter 3

Measurement with Spectral Fitting

Abstract We report a model-dependent measurement of the inclusive B-meson semileptonic branching fraction from 2.057 fb^{-1} of $\Upsilon(4S)$ data collected with the CLEO-II detector. By fitting the inclusive lepton spectra to the refined quark model of Altarelli *et al.*, we obtain $\mathcal{B}(B \to X\ell\nu) = (10.56 \pm 0.04 \pm 0.22)\%$. With a modified version of the form-factor model of Isgur *et al.*, in which the fraction of $B \to D^{**}\ell\nu$ is allowed to float, we find $\mathcal{B}(B \to X\ell\nu) = (10.96 \pm 0.07 \pm 0.22)\%$. The original Isgur model yields a lower branching ratio, $\mathcal{B}(B \to X\ell\nu) = (10.26 \pm 0.03 \pm 0.22)\%$, but with a higher χ^2. Using the measured semileptonic branching ratios, we have also obtained the CKM matrix element $|V_{cb}|$ and confirmed the CLEO measurement of $|V_{ub}/V_{cb}|$.

3.1 Introduction

Semileptonic decay of B-mesons plays an important role in understanding both the electroweak and strong interactions. This process provides a straightforward (if model dependent) way to measure the CKM matrix elements V_{cb} and V_{ub} and to probe non-perturbative QCD [5]. Previous measurements of the B-meson semileptonic branching fraction have given values which are significantly below theoretical expectations, as reviewed in Chapter 1. The simple spectator quark model predicts this branching ratios to be 16.5%, and while QCD corrections can bring this down to 12.5% or so, the experimental values have consistently been below 12%. This chapter presents the results of our study of B-meson semileptonic decays with CLEO II [28]. In addition to the intrinsic physics interest of the B semileptonic decay momentum spectrum and branching fraction, this study also provides a rigorous test of the performance and our understanding of CLEO's lepton identification.

This chapter presents a detailed description of our analysis. It parallels the procedures we followed. We first discuss the data sample and the specific event- and lepton-selection criteria. Discussion of corrections to the observed lepton spectra follows, beginning with the estimation of "fakes", hadrons misidentified as lepton candidates. We then describe the subtraction of leptons from processes, which are not of interest to this analysis, and the correction for identification efficiency. After the discussion of these corrections, we describe the fitting procedure which we use to measure the direct contribution of semileptonic B decays (primary leptons), and of semileptonic decays of the charmed mesons produced in B decays (secondary leptons). We then discuss the theoretical framework used to develop the functions which we employ to extract the branching ratios, summarize the systematics of the measurement, and present our results. To conclude we calculate the CKM matrix elements $|V_{cb}|$ and $|V_{ub}|$.

3.2 Data Sample and Lepton Selection

The data sample used for this analysis consists of 2,057 pb^{-1} collected at the $\Upsilon(4S)$ (ON), and 958 pb^{-1} taken at CM energies ~ 60 MeV below resonance (OFF). The ON data include $2,202,000 \pm 11,000$ $\Upsilon(4S)$ decay events. In this study we assume that all the $\Upsilon(4S)$ mesons decay into $B\overline{B}$ pairs. We studied efficiencies and backgrounds with 5 million generic $\Upsilon(4S) \to B\overline{B}$ Monte Carlo events. In addition, about 60 pb^{-1} of $\Upsilon(1S)$ data were used to estimate the lepton identification fake rates.

Lepton candidates are selected from multihadron events (referred to as `KLASGL` = 10), with five or more charged tracks. We put the candidates into two categories: "identified" leptons, which pass stringent identification requirements, are used for the signal, and "loose" leptons, which are less stringently identified, are used for background studies. Since most of the background sources give two oppositely charged leptons (such as $J/\psi \to \ell^+\ell^-$, and $\pi^0 \to e^+e^-\gamma$), looser cuts on the second lepton increase the efficiency for determining these backgrounds. For this analysis our primary objective is to study semileptonic B decay with minimal background and maximum understanding of efficiencies and systematic effects. In what follows "lepton" will signify "identified lepton" except as explicitly indicated.

For both lepton categories we require the candidate track to have good quality [29]. We reject "ghost" tracks which result when the hits produced by a single charged particle are erroneously reconstructed as two tracks. We also eliminate "curlers", low momentum tracks that spiral in the CD, and are therefore reconstructed as several tracks. The "residual" of the track fit is required to be less than 1 mm ($\texttt{RESICD} < 1mm$). The track is required to originate near the expected vertex, with an impact parameter in the $r - \phi$ plane of less than 5 mm ($|\texttt{DBCD}| < 5mm$), and an impact parameter in the $r - z$ plane of less than 5 cm ($|\texttt{ZOCD}| < 5cm$). Finally, we require that there be at least one valid hit in the PT and VD ($\texttt{NHITPT} + \texttt{NHITVD} > 0$), and that no fewer than 40% of the DR layers which should have hits for a particular track actually registered valid hits ($\texttt{RHITDR} > 0.4$). These track-quality cuts individually are not extremely stringent. Identified leptons are required to satisfy all four of these requirements, while loose leptons need only satisfy any three.

After the track quality cuts, we apply the standard CLEO-II lepton identification packages with the selection criteria listed in Table 3.1. As described in Chapter 2, electrons are identified with a likelihood ratio `R2ELEC` that combines information on E/p, dE/dx, TF and shower shapes. Muon candidates are selected from tracks matched to all expected muon chamber hits (with quality code $\texttt{muqal} = 0$). In order to reduce misidentification from kaons and pions that have penetrated the inner absorber, we require hits beyond 5 absorption lengths ($\texttt{dpthmu} > 5$). We use only the good-barrel part of the calorimeter for signal electrons. Similarly we select muon candidates from only the barrel region of the muon detector, where we have all three layers of muon chambers. The end-cap regions are not used for signal leptons because of inferior track finding and lepton identification.

Table 3.1: Lepton Identification

	Lepton Candidates	Loose Leptons
e	$45° \leq \theta \leq 135°$	$25° \leq \theta \leq 155°$
	$\texttt{R2ELEC} \geq 3.0$	$\texttt{R2ELEC} \geq 0.0$
μ	$\lvert cos\theta \rvert \leq 0.61$	$\lvert cos\theta \rvert \leq 0.88$
	$\texttt{muqal} = 0$	$\texttt{muqal} = 0$ or $\texttt{muqal} \geq 10^4$
	$\texttt{dpthmu} \geq 5.0$	$\texttt{dpthmu} \geq 3.0$

Using the lepton-identification criteria described above, we obtain the raw uncorrected lepton spectra shown in Figs. 3.1 (electrons) and 3.2 (muons). The OFF spectra are used to estimate the shape and amount of the contribution from continuum processes to the ON spectra. It is usually possible to use criteria based on overall event topology to supress the continuum contribution. In this study, no continuum-suppression cuts have been employed, because the statistical error introduced by the continuum subtraction is not a significant limitation on the precision of our measurement, and the use of continuum suppression might alter the spectral shape in ways which are not perfectly modeled by Monte Carlo. The scale factor for the continuum subtraction is given by

$$\alpha_{\mathcal{L}}(4S) = \frac{\int \mathcal{L}(ON)dt}{\int \mathcal{L}(OFF)dt} \frac{E^2_{beam}(OFF)}{E^2_{beam}(ON)} = 2.124 \pm 0.011 \tag{3.1}$$

Figs. 3.1b and 3.2b show the result of this subtraction, *i.e.* leptons from Υ(4S) $B\overline{B}$

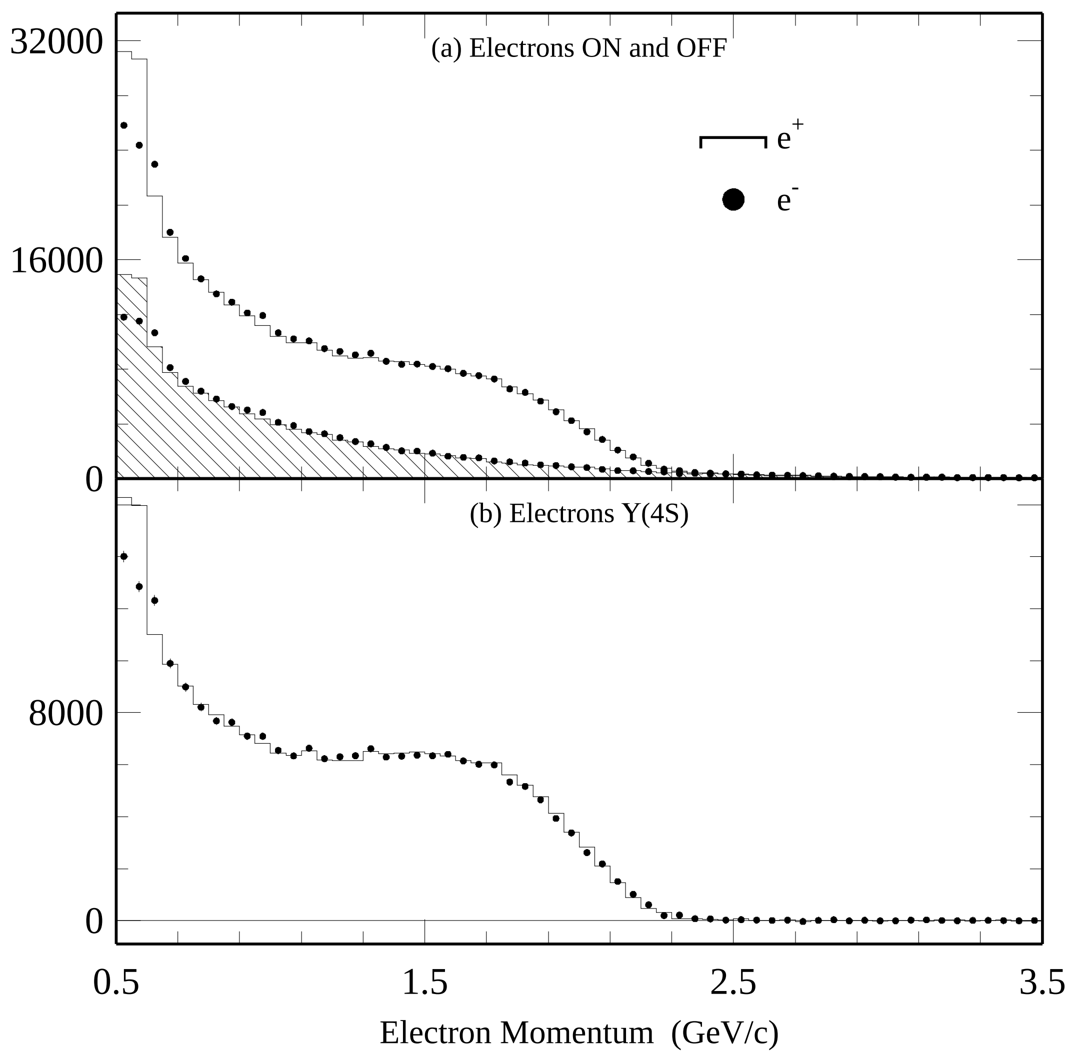

Figure 3.1: Raw spectrum of identified electrons (a) for ON and luminosity scaled OFF (shaded), and (b) for the $\Upsilon(4S)$. The histograms are e^+, and the dots are e^-.

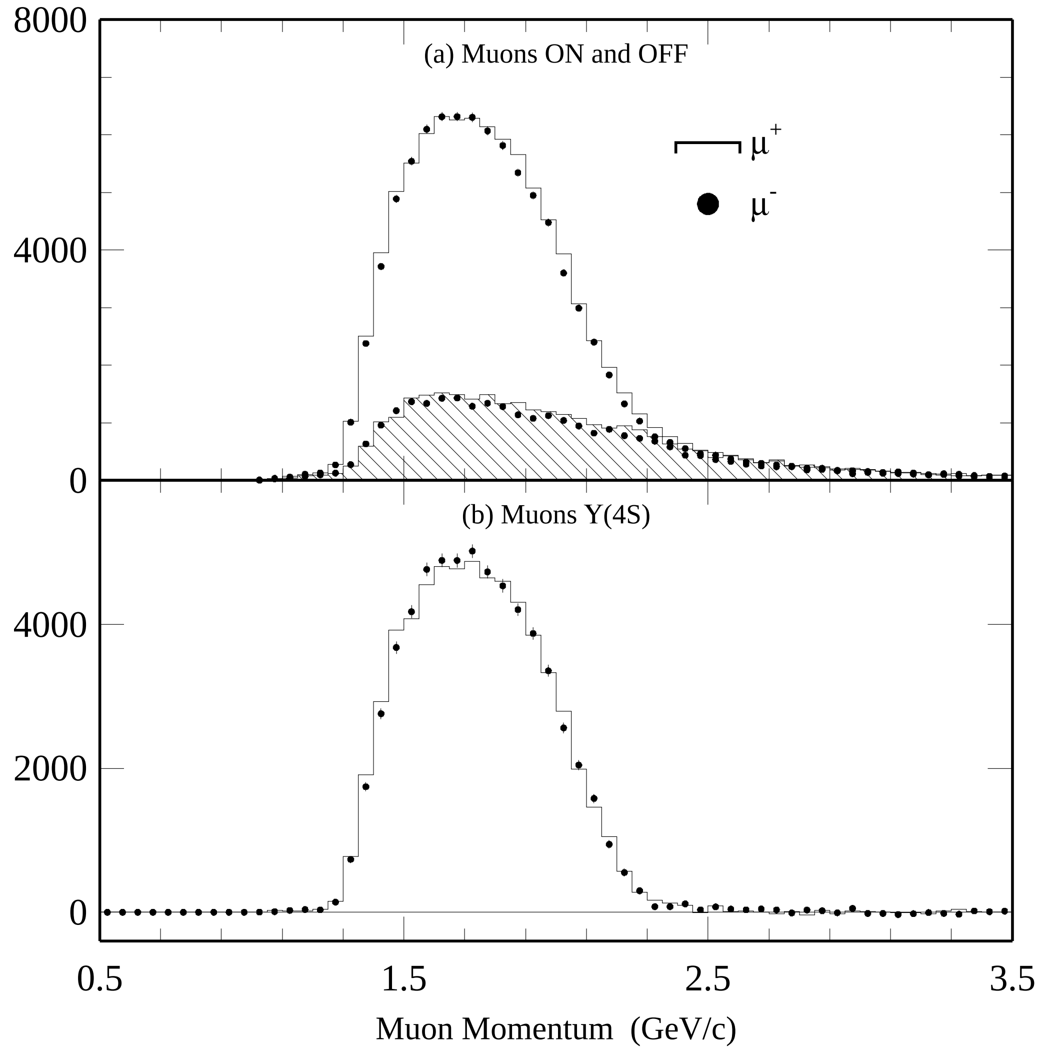

Figure 3.2: Raw spectrum of identified muons (a) for ON and luminosity scaled OFF (shaded), and (b) for the $\Upsilon(4S)$. The histograms are μ^+, and the dots are μ^-.

decays. Table 3.2 shows the total number of raw lepton candidates in the momentum and geometric region used in this study.

Table 3.2: Lepton Candidate Raw Yields

	e^+	e^-	μ^+	μ^-
p(GeV/c)	$0.6 - 3.5$		$1.3 - 3.5$	
geometry	$\lvert cos(\theta)\rvert \leq 0.71$		$\lvert cos(\theta)\rvert \leq 0.61$	
ON	295,374	300,946	91,750	88,854
continuum	100,411	104,738	29,739	26,984
Υ(4S)	194,963	196,208	62,011	61,870

3.3 Fake Corrections

Fakes are hadronic tracks misidentified as leptons. The following equation describes the relationship between the true numbers of electrons, muons, and hadrons, and the numbers of detected electrons, muons and charged tracks:

$$\begin{bmatrix} n_t \\ n_e \\ n_\mu \end{bmatrix} = \begin{bmatrix} 1 & 1 & 1 \\ f_e & \epsilon_e & 0 \\ f_\mu & 0 & \epsilon_\mu \end{bmatrix} \begin{bmatrix} N_h \\ N_e \\ N_\mu \end{bmatrix} \tag{3.2}$$

The quantities appearing in this equation are defined as follows:

- N_h, N_e, N_μ are the true numbers of hadrons, electrons and muons;
- n_t, n_e, n_μ are the numbers of detected tracks, identified electrons and muons;
- f_e and f_μ are the fake rates for electron and muon identification;
- ϵ_e and ϵ_μ are the lepton identification efficiencies.

The fake contamination in the identified lepton sample can be estimated by multiplying the fake probability per track by the number of hadron tracks:

$$N^{\ell\pm}_{fake} = f^{\pm}_{\ell} \cdot N^{\pm}_{h}, \tag{3.3}$$

where $\ell = e, \mu$. All the above quantities are functions of lepton momentum. In other words, $N_\ell^\pm$ or $N_h^\pm$ are actually the momentum spectra of leptons and hadrons. Introducing $R_{\mu/e} = N_\mu/N_e$ as the ratio of muon and electron yields, we solve Eq.3.2 to obtain

$$N_h = \frac{n_t - (1 + R_{\mu/e}) \cdot (n_e/\epsilon_{eID})}{1 - (1 + R_{\mu/e}) \cdot (f_e/\epsilon_{eID})}. \tag{3.4}$$

In the following subsections, we describe the procedures to determine the parameters which appear in these equations.

3.3.1 Fake Rates

Fake rate is the average probability of misidentifying a hadron as an electron or muon. It is charge and momentum dependent. As described in Chapter 2, we studied the fake rates with a data sample of hadron tracks at the $\Upsilon(4S)$ and a sample at the $\Upsilon(1S)$. As is shown in Figs. 2.6, f_e in the barrel region is about 0.2% above 1.4 GeV/c, and between 0.2% and 1.2% at lower momenta. f_μ is about 1% in the barrel. Due to the lack of statistics for the $\Upsilon(4S)$ sample, we use the fake rates obtained from the $\Upsilon(1S)$ sample. There is good agreement between the two measurements, and we have used the difference as an estimate of the systematic error in the fake correction.

3.3.2 Yields Ratio of μ and e

In principle, $R_{\mu/e}$ is equal to 1, as a result of lepton universality. Three factors contribute to its deviation from 1. First, bremsstrahlung for electrons and muons is different. Second, at lower momenta the processes $\pi^0 \to e^+e^-\gamma$ and γ conversions contribute only to the electron yield. Finally, the electroweak radiative corrections to the lepton spectrum are different for electrons and muons. According to Atwood and Marciano [21], this makes $R_{\mu/e}$ rise by 5-10% at high momentum, and drop by the same amount at low momentum.

The first two factors in $R_{\mu/e}$ are estimated by using generic $\Upsilon(4S) \to B\overline{B}$ Monte

Carlo. We obtain this by a simple division of the spectra for tagged prompt muons and electrons from the Monte Carlo, with our track quality cuts applied. Fig. 3.3a shows the result of this division.

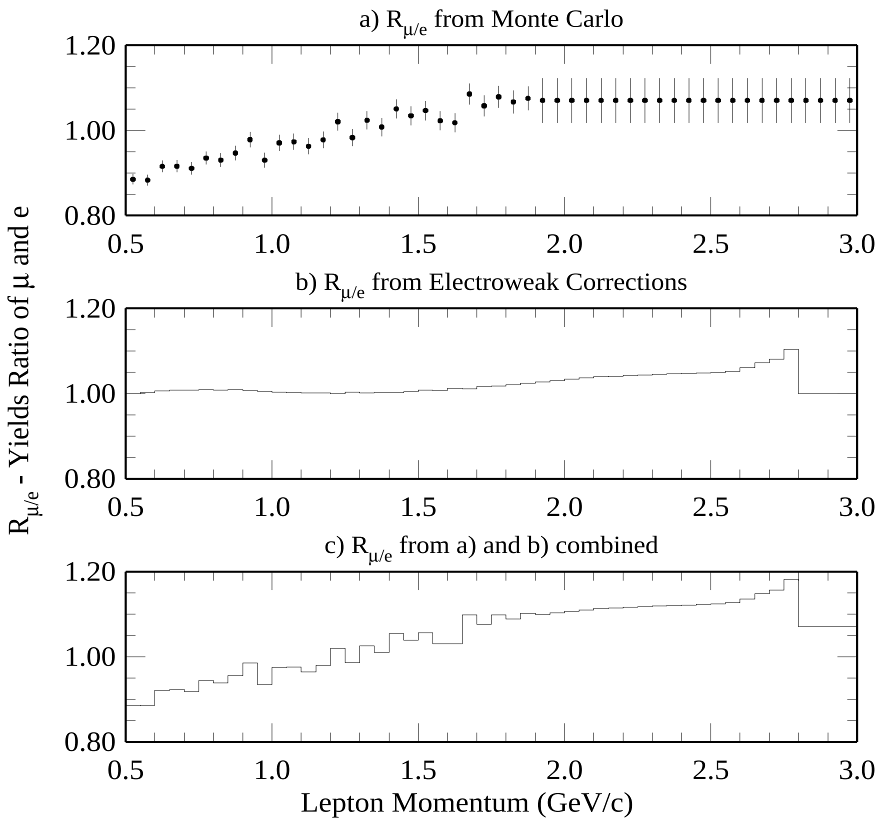

Figure 3.3: Yields ratio of e and μ, $R_{\mu/e}(p)$. Note the zero of the vertical scale.

To simulate the radiative effect we first use the ACCMM model [13] to generate lepton spectra for primary and secondary decays. We then apply the electroweak radiative corrections for electrons and muons, as prescribed by Atwood and Marciano. The primary and secondary lepton spectra are then combined according to the branching ratios from previous measurements to get the inclusive electron and muon spectra. By dividing them we get the correction on $R_{\mu/e}$ due to radiative effects, as shown in Fig. 3.3b. The function in Fig. 3.3c is the combined $R_{\mu/e}$ which we use in this analysis.

3.3.3 Computation of Fake Correction

The remaining ingredient needed for Eq. 3.4 is the electron identification efficiency ϵ_{eID}. We use the results from a data sample made by embedding radiative Bhabha tracks into $\Upsilon(4S)$ hadronic events [25], as is discussed in Chapter 2.

With the above momentum dependent functions $R_{\mu/e}$, $f_l^{\pm}$ and $\epsilon_e^{\pm}$, we subtract the fakes according to Eqs. 3.3 and 3.4. The tracks and fakes are shown in Fig. 3.4. The correction is summarized in Table 3.3. For convenience we have presented the results

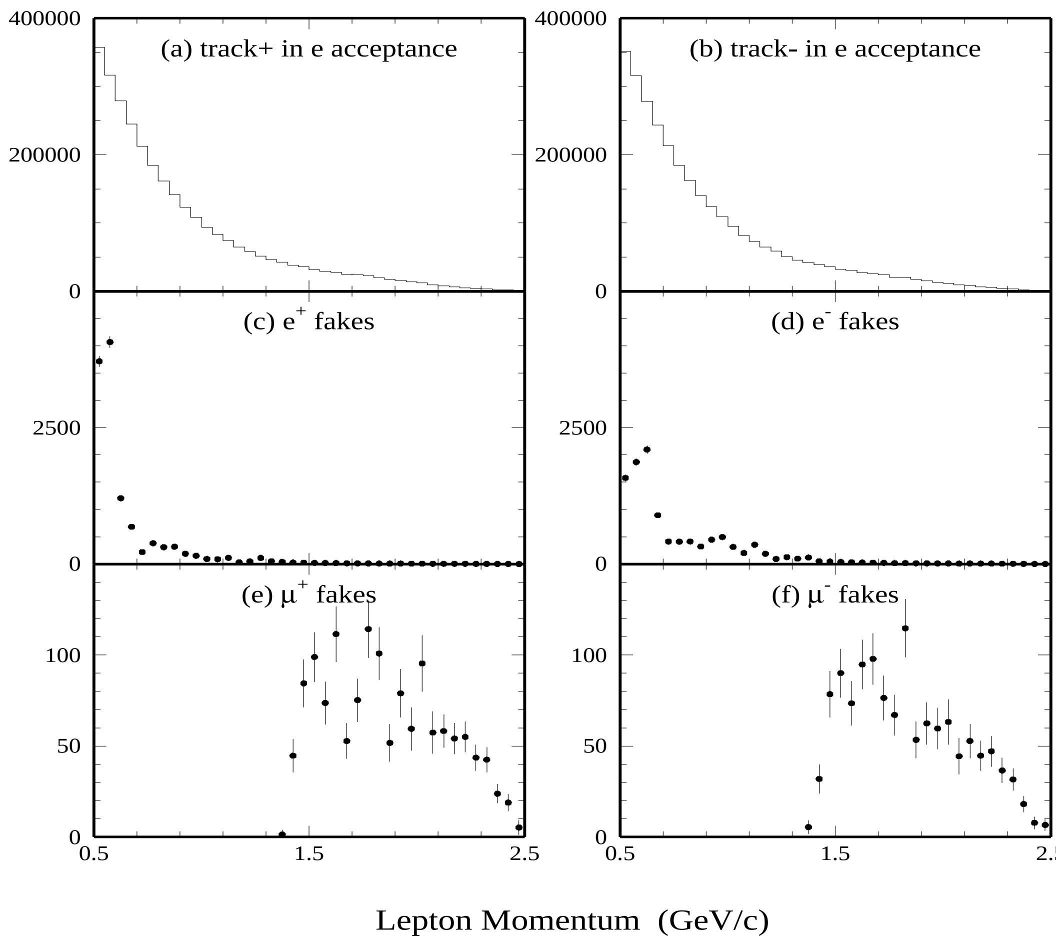

Figure 3.4: Spectra of tracks (a), (b); fake electrons (c), (d) and fake muons (e), (f).

in two coarse momentum regions, low (0.6-1.3 GeV/c) and high (1.3-3.5 GeV/c).

Table 3.3: Summary of Fake Correction

lepton	low e^+	low e^-	high e^+	high e^-	high μ^+	high μ^-
n_t	1,876,000	1,875,500	438,914	139,173		
N_h	1,647,150	1,645,720	240,775	241,510	207,711	208,345
N_f	3,932	6,746	308	603	1,390	1,218
n_{raw}	106,200	108,240	88,763	87,968	62,011	61,870

3.4 Background Corrections

We define all sources of leptons other than $B \to X\ell\nu$ (primary leptons) or $B \to DX, D \to Y\ell\nu$ (secondary leptons) as background leptons. We remove each source separately as described below.

3.4.1 $J/\psi \to \ell^+\ell^-$

The decay chain $B \to J/\psi X$, $J/\psi \to \ell^+\ell^-$ contributes both electrons and muons between 0.8 and 2.6 GeV/c. This is a major background to the higher momentum side of the inclusive spectra, and thus particularly affects the $b \to u\ell\nu$ piece of the spectrum. We combine each lepton candidate with any accompanying oppositely charged loose leptons of the same flavor to calculate the two-body invariant mass $M(\ell^+\ell^-)$ which is shown in Fig. 3.5. No corrections for energy loss in the tracking chamber have been applied to the tracks when calculating the dilepton mass. A second-order polynomial and a bifurcated Gaussian are used to fit each mass plot. The parameters of the J/ψ fits are $3,099.2^{+9.8}_{-29.2}$ MeV/c^2 and $3,092.7^{+12.6}_{-14.5}$ MeV/c^2 for electrons and muons respectively. From these fits we define the 3σ J/ψ mass peak and its sidebands in such a way that a sideband is separated from the peak by another σ.

We determine the momentum spectra for leptons from detected J/ψ's by a sideband subtraction. To account for the contribution of J/ψ's which are not detected, we correct by the efficiency for detecting leptons from inclusive J/ψ's which we determine from

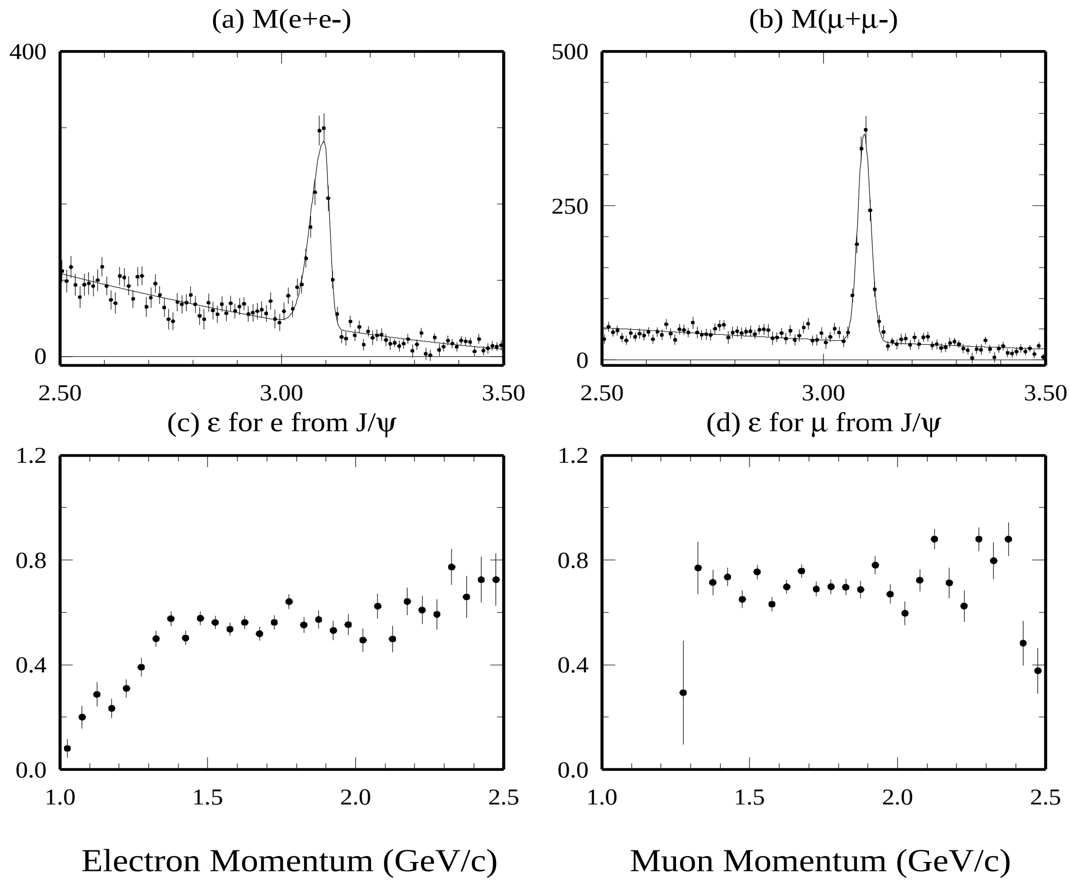

Figure 3.5: Correction for lepton pairs from ψ decays. Dielectron mass is (a) and dimuon (b). The efficiencies are shown in (c) and (d).

Monte Carlo. This efficiency is approximately $(63 \pm 4)\%$ for the dielectron decays, and $(59 \pm 4)\%$ for the dimuon decays, as is shown in Fig. 3.5c–d. The efficiency-corrected spectra of leptons from J/ψ are shown in Fig. 3.6a–b. They are directly subtracted from the inclusive lepton spectra.

3.4.2 Photon Conversion Correction

There is a significant contribution to the low momentum electron signal from the conversion of photons in the beam pipe and in material between the tracking chambers. Our track quality cuts eliminate 95% of the conversions. The remainder must be subtracted

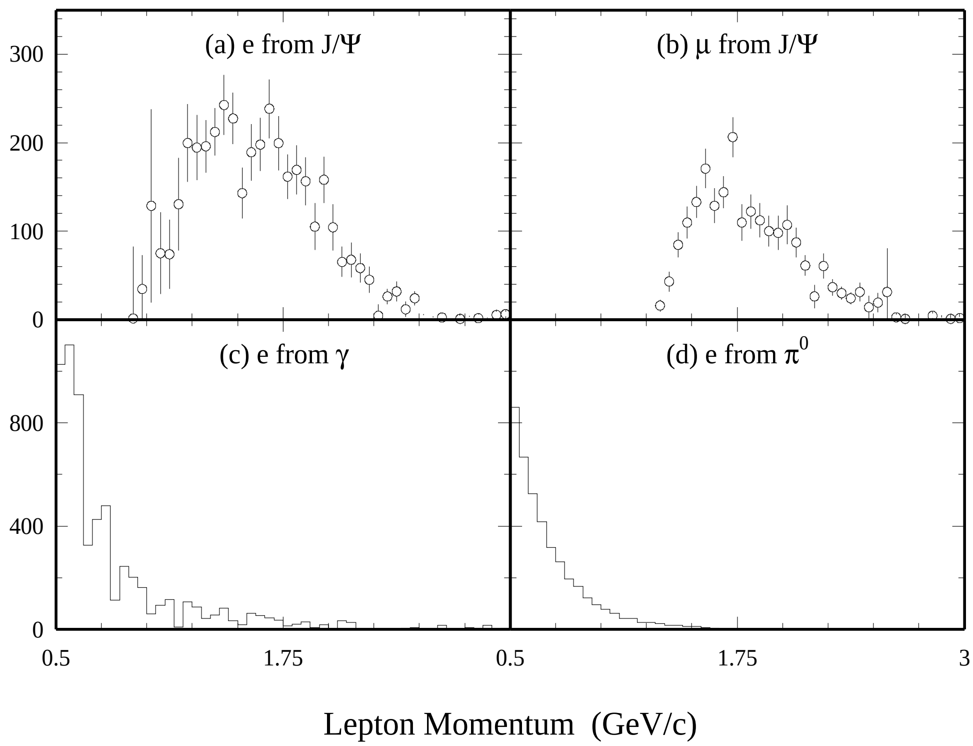

Figure 3.6: Background corrections which are subtracted from the inclusive lepton spectra. Leptons from $B \to J/\psi X, J/\psi \to \ell^+\ell^-$ are shown in (a) and (b); electrons from π^0 Dalitz decays and from photon conversions are shown in (c) and (d).

from the electron spectra, just as the fakes are.

The pair-conversion finder [30] is used to flag identified electrons which are the product of photon conversions. Its efficiency rises linearly from 50% at 0.5 GeV/c to one at 1.3 GeV/c. The photon conversion correction is obtained by correcting the observed momentum spectrum of vetoed electrons by the conversion finder efficiency. The resulting correction is shown in Fig. 3.6c.

3.4.3 π^0 Dalitz Decays

At lower momentum, the Dalitz decay $\pi^0 \to e^+e^-\gamma$ is another background which produces e^+e^- pairs. We deal with it in almost the same way as the J/ψ background, except that we form a three-body invariant mass $M(e^+e^-\gamma)$ instead of $M(e^+e^-)$. The selection criteria for the photons are listed below:

- shower not matched to a track; • energy > 25 MeV; • $45° \le \theta \le 135°$
- photon not from $\pi^0 \to \gamma\gamma$ • shower contained mostly in 3×3 crystals

The three-body mass is fitted with a Gaussian and a second-order polynomial to get the width of the π^0, and to define sidebands for subtraction, as was described in the previous subsection. We obtain $m(\pi^0) = 135 \pm 6$ MeV and the efficiency from Monte Carlo is $(13 \pm 3)\%$. Due to the lack of statistics, we use the Monte Carlo momentum spectrum shape of such electrons. This spectrum is then normalized to the number of such Dalitz decays found in data with the above invariant mass method. The subtracted electron spectrum from Dalitz decays is shown in Fig. 3.6d.

3.4.4 Leptons from D_s and Λ_c

Leptons from the decay $B \to D_s X$, $D_s \to \ell Y$ are subtracted by using the Monte Carlo sample. The momentum spectrum of D_s is tuned to match that from data and normalized to the measured branching ratio $\mathcal{B}(B \to D_s X) = (11.81 \pm 0.43 \pm 0.94)\%$ [51]. The spectrum of electrons from D_s is shown in Fig. 3.7a.

Similarly, leptons from charmed baryons, mainly Λ_c, are also subtracted by using Monte Carlo. The production of Λ_c from B decays is modeled to include 20% charmed baryon pair production through the channel $B \to \Xi_c \Lambda_c^- n\pi$, in addition to the decays $B \to \Lambda_c \bar{p}(\bar{n}) n\pi$. The Λ_c spectrum from this model matches data in both shape and rate $\mathcal{B}(B \to \Lambda_c X) = (6.4 \pm 1.1)\%$ [52]. The subtracted leptons from charmed baryons are shown in Fig. 3.7b.

3.4.5 τ Decays and Other Backgrounds

The contribution of leptons from $B \to X\tau\nu, \tau \to \ell\nu\nu$ can be calculated from the inclusive $B \to X\ell\nu$ branching ratio. We use the previously measured result $\mathcal{B}(B \to X\ell\nu)$ [11] combined with the phase space factor for $B \to X\tau\nu$, which gives $\mathcal{B}(B \to X\tau\nu) = 2.5\%$.

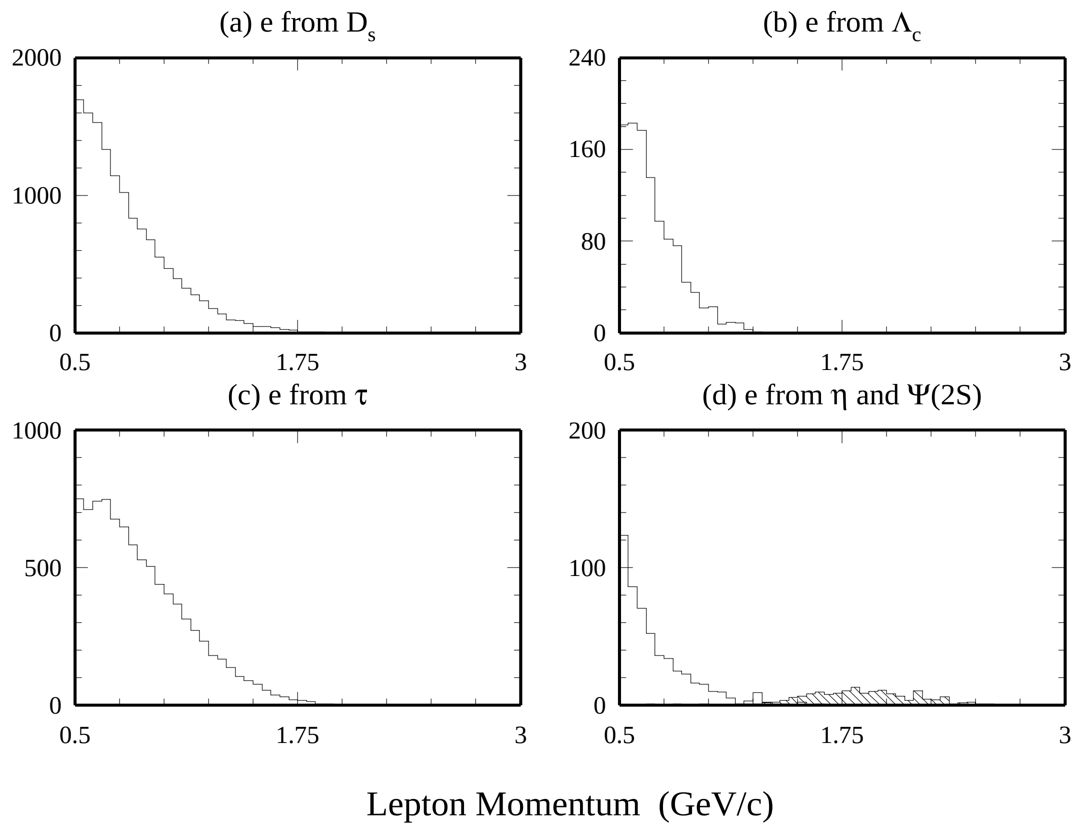

Figure 3.7: Electrons from (a) D_s, (b) Λ_c, (c) τ and (d) η (at lower momenta) and $\psi(2S)$ (higher momenta).

This is in good agreement with a recent measurement of this quantity by the ALEPH experiment [32]. The calculated spectra of e and μ from τ decays are subtracted from the inclusive spectra as in Fig. 3.7c.

Contributions from other background sources, such as $B \to \psi(2S)X$, $\psi(2S) \to \ell^+\ell^-$ and $B \to \eta X$, $\eta \to e^+e^-\gamma$, are also subtracted by using Monte Carlo. They are plotted in Fig. 3.7d.

3.4.6 Summary of Backgrounds

We summarize the above background corrections in Table 3.4. In the high momentum region, leptons from charmonium states are the main contributions. At lower momenta,

Table 3.4: Summary of Background Leptons

Sources	e 0.6–2.8 GeV/c	μ 1.3–2.8 GeV/c
J/ψ	$3,868 \pm 210$	$2,098 \pm 95$
π^0	$2,473 \pm 1,328$	—
γ	$3,783 \pm 342$	—
D_s	$10,300 \pm 84$	551 ± 32
Λ_c	721 ± 17	0
τ	$7,401 \pm 58$	388 ± 27
$\psi(2S)$	165 ± 8	120 ± 7
η	317 ± 18	—
total	$29,028 \pm 1,391$	$3,127 \pm 104$

all other sources contribute. The small errors reflect the high statistics of the Monte Carlo sample. We also list in Table 3.5 leptons in three momentum regions after these background corrections. B-meson decays at the Υ(4S) can not produce tracks with momentum above 2.8 GeV/c. Our results are consistent with this expectation.

Table 3.5: Number of Leptons from Background Subtracted Spectra

p GeV/c	0.6-1.3	1.3-2.8	2.8-3.5
e	$204,445 \pm 1,632$	$170,645 \pm 645$	64 ± 105
μ		$118,131 \pm 554$	15 ± 112

3.5 Efficiency Corrections

We must correct the lepton spectra for the inefficiencies in event selection and lepton identification. The overall efficiency is given by the following equation:

$$\epsilon = \underbrace{(\epsilon_{K10} \cdot \epsilon_{tr5})}_{\epsilon_{evt}} \cdot \epsilon_{geo} \cdot \underbrace{(\epsilon_{tracking} \cdot \epsilon_{TQ} \cdot \epsilon_{\ell ID})}_{\epsilon_{\ell}}. \tag{3.5}$$

From our Monte Carlo sample, the efficiency for choosing class 10 events with at least 5 charged tracks is determined to be $\epsilon_{evt} = (97.2 \pm 0.7)\%$ for generic $B\bar{B}$ events and slightly lower at 96.5% for events with leptons. This difference in event selection is taken into account in the correction procedure. The geometric acceptance ϵ_{geo} is 0.71 and 0.61 for electrons and muons, respectively.

The lepton finding efficiency ϵ_ℓ includes a slightly momentum dependent track finding and quality requirement efficiency of $(96 \pm 1)\%$, and a strongly momentum dependent efficiency of the lepton identification packages. This is particularly the case for muon detection, as $\epsilon_{\mu ID}$ turns on starting from 1.3 GeV/c. $\epsilon_{\mu ID}$ is determined by Monte Carlo. It has been shown [26] that there is good agreement between the simulation and data. The efficiency of the electron identification package ϵ_{eID} was determined with a sample of radiative Bhabha tracks embedded in $\Upsilon(4S)$ hadronic events [25]. We show ϵ_ℓ and efficiency corrected lepton spectra in Fig. 3.8. These efficiencies do not include any radiative corrections.

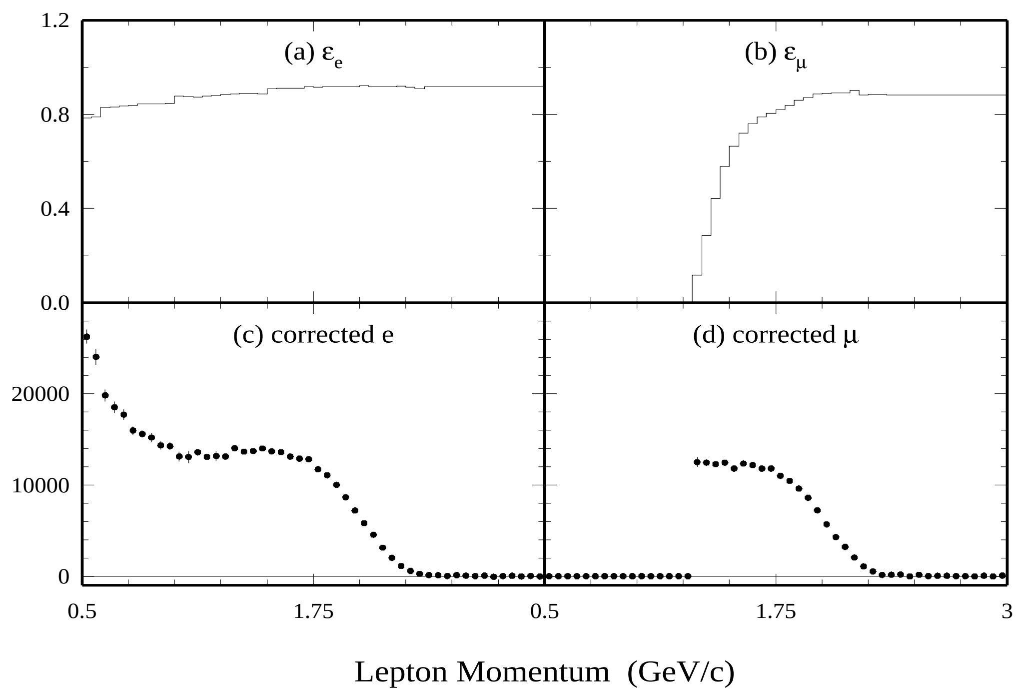

Figure 3.8: Efficiencies ϵ_ℓ and efficiency corrected lepton spectra for electrons (a), (c) and muons (b), (d) respectively.

3.6 Normalization of the Spectra

After the efficiency corrections, we normalize the lepton spectra to the total number of B decays. There are 8,072,790 events passed our event selection in the ON data sample, and 2,791,280 events in the OFF sample. By using the luminosity scale factor derived from equation 3.1, we find the total number of Υ(4S) events that are hadronic, class 10 with at least 5 charged tracks, to be $2,143,430 \pm 10,720$. This 0.5% error comes from the uncertainties in the luminosity and beam energy in calculating $\alpha_{\mathcal{L}}(4S)$.

The absolutely normalized spectra for electrons and muons are shown in Fig. 3.9 (also tabulated in Appendix D after corrections for detector bremsstrahlung). The difference

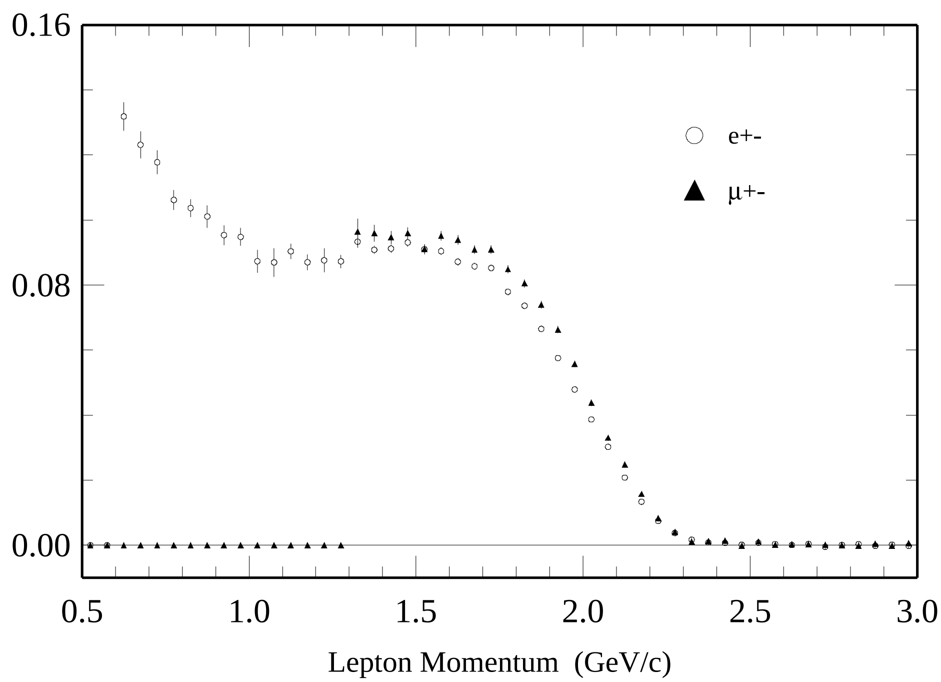

Figure 3.9: Inclusive lepton spectra normalized to the total number of Υ(4S) events after all corrections.

between e and μ is due to internal and external bremsstrahlung. These spectra contain leptons from primary and secondary decays of the B mesons. Theoretical models must next be used to determine how many are directly from B decay, so that the inclusive B semileptonic branching fraction can be extracted.

3.7 Theoretical Functions

The inclusive lepton spectra contain contributions of leptons from primary B decays $b \to c\ell\nu$ and $b \to u\ell\nu$, and from secondary decays $B \to DX$ followed by $D \to Y\ell\nu$. We use theoretical models and available experimental data to calculate the shape of the lepton spectrum expected for each decay process. By fitting our measured specta with these shapes, we can extract information about the $B \to X\ell\nu$ branching ratio.

The theoretical models fall into two categories, inclusive and exclusive, as is discussed in Chapter 1. The inclusive models calculate decay rates at the quark level. The simplest is the free-quark model. When the b quark decays to a c quark and a W^-, the W^- can decay to the following pairs: $(e^-, \bar{\nu_e})$, $(\mu^-, \bar{\nu_\mu})$, $(\tau^-, \bar{\nu_\tau})$, $(\bar{u}, d)$ and $(\bar{c}, s)$. The latter two each enter with a color factor of 3. Naively, we expect the total width to be shared equally by the 9 pairs, except for phase space modifications for the massive final states $(\tau^-, \bar{\nu_\tau})$ and $(\bar{c}, s)$. This gives an expected semileptonic rate of 16.5%, as described in Chapter 1. The smaller measured values suggest that diagrams other than the spectator process contribute significantly to B decays. Altarelli *et al.,* introduced phenomenological internal motion inside the B mesons, as well as QCD corrections, to describe B decays [13]. Recent work based on heavy quark expansion [20] has advanced the calculation in non-perturbative QCD by describing the Fermi motion in terms of the kinetic energy of the b quark. It also demonstrated that the derived lepton spectrum is well represented by the ACCMM prescription in most of the momentum range. This heavy quark expansion diverges, however, near the endpoint region. We therefore did not use it to fit the data in this study.

The exclusive models calculate decay rates based on explicit final meson states, under the assumption that the decays are resonance dominated. The total rates are the sum over a few final-state mesons according to QCD sum rules by Bjorken and Shifman-Voloshin. The calculations are only possible phenomenologically by defining unknown form factors as functions of momentum transfer q^2. The dependence on q^2 differs among models such as ISGW [15], WSB [16] and KS [17]. The form-factor dependence is simplified by the Heavy Quark Effective Theory (HQET) as it expresses the form factors in terms of a single universal function. It provides a means to derive the CKM matrix element V_{cb} by measuring the exclusive semileptonic decays for heavy-light quark systems. It can further be combined with chiral symmetry to calculate nonresonant final states and can be factorized for hadronic decays when applicable. For our study, we use the ISGW model, since it is the only exclusive model currently avalable which takes into account the higher spin states, the D^{**}'s.

3.7.1 The ACCMM Model

The model of Altarelli *et al.* (ACCMM) [13] uses a Gaussian distribution to describe the internal motion inside the B mesons. The root mean square of this momentum distribution is called the Fermi momentum P_F. As a consequence, we do not need to use the initial quark mass as in the free quark model, only the initial meson mass and the Fermi momentum. The final quark mass, however, is not determined, and is left as a second parameter in this model. We determine both the Fermi momentum and final quark mass from the fits to data in the next section. In addition, QCD internal radiation corrections to the free-quark model are included in the ACCMM model.

3.7.2 The ISGW Model

The model of Isgur *et al.* (ISGW) [15], is the first of the exclusive models. In this model, the initial state meson decays semileptonically into final state mesons including the pseudoscalar, vector and a few higher spin states. In the case of $b \to c\ell\nu$, the final states are the D, D^* and four D^{**} states.

The decay rate for pseudoscalar to pseudoscalar transitions ($P \to P$) is determined by two form factors and that for pseudoscalar to vector ($P \to V$) by five. The form factors and their q^2 dependence are simulated by a mock meson similar to a hydrogen atom, in which the wave functions at zero recoil are determined from a Coulomb plus linear potential in the Schrödinger equation. To modify this for relativistic effect, a multiplicative constant κ is introduced which controls the slope of the q^2 dependence. This can be treated as a parameter in the ISGW model.

3.7.3 Electroweak Radiative Corrections

Atwood and Marciano [21] suggest three types of electroweak radiative corrections: virtual loop corrections at high energy, low energy photon internal bremsstrahlung and loops, and Coulomb corrections for neutral initial state mesons. We implement the second into our analysis, as described in Chapter 1, since it is the only one that affects the shape of the momentum spectrum for semileptonic decays. This internal bremsstrahlung correction changes the shape of the spectrum, but not the normalization. It is specified in terms of the maximum and average energies of the lepton spectrum. It introduces a 2-10% difference varying with momentum for muons and electrons, as is illustrated in Fig. 1.4.

3.7.4 Procedure to Generate Theoretical Functions

For each model, we construct the theoretical lepton momentum spectra for $b \to c\ell\nu$, $b \to u\ell\nu$, and $b \to c \to x\ell\nu$ in four steps [11]:

- generate the spectra in the B or D rest frame;
- apply electroweak corrections;
- boost into the lab frame, using the B or D momentum distribution;
- smear the spectra to account for detector resolution and bremsstrahlung.

The first two steps, models and electroweak corrections, have been described in Chapter 1 and summarized in the previous section. We boost the resulting lepton spectra from B decays into the lab with B momenta appropriate for our $\Upsilon(4S)$ sample.

To boost the secondary lepton spectra into the lab, we use the measured momentum spectra for D^0 and $D^{\pm}$ mesons [51], as is shown in Fig. 3.10. We combine the two boosts using the branching ratio information listed in Table 3.6 [51, 52].

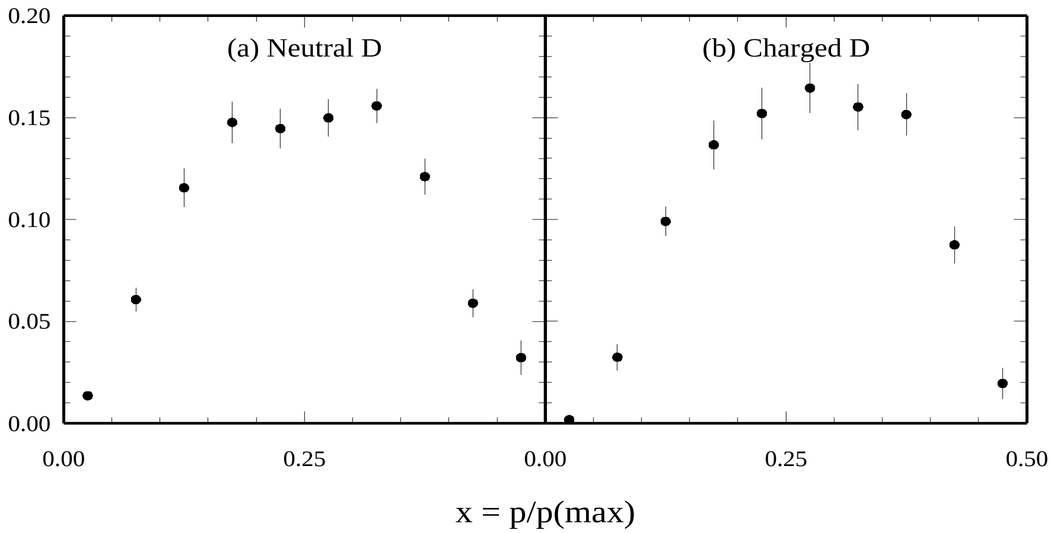

Figure 3.10: Inclusive D meson spectra measured by CLEO. (a) D^0 and $\bar{D}^0$ and (b) $D^{\pm}$. The vertical scale is arbitrary.

Table 3.6: Branching Ratios for Secondary Leptons

D	$\mathcal{B}(B \to DX)\%$	$\mathcal{B}(D \to Y\ell\nu)\%$	$\mathcal{B}(b \to c \to y\ell\nu)\%$
D^0	62.1 ± 2.6	7.0 ± 0.6	4.4 ± 0.4
D^+	23.9 ± 3.7	17.9 ± 1.6	4.3 ± 0.8
sum			8.7 ± 0.9

We simulate the effect of bremsstrahlung and momentum resolution in the detector with response functions determined by Monte Carlo. For each identified lepton track in the Monte Carlo sample we increment an element of a two-dimensional array which corresponds to its generated momentum `PSAV` and its measured momentum `PQCD`. This array is then normalized column by column to produce the smearing matrix. Each entry in the matrix has an associated error which reflects the limited Monte Carlo statistics. These errors are propagated through the smearing process into the final smeared spectra.

After the theoretical functions are generated by the above procedure, we normalize the three shapes to $1/\text{binwidth} = 1/0.05\,\text{GeV}/c$, so that the coefficients determined by fitting the functions to the absolutely normalized data spectra are the branching ratios for the three decay processes.

3.8 Fitting

For each theoretical model we first fit the electron and muon spectra separately to check consistency with lepton universality. Because of the momentum cut-off at 1.3 GeV/c, the muon fit is quite insensitive to the secondary semileptonic branching ratio, which is dominated by the low momentum part of the electron spectrum. For this reason we constrain the muon secondary branching ratio to be the same as the result of that from the electron fit, $\mathcal{B}(b \to c \to y\mu\nu) = \mathcal{B}(b \to c \to ye\nu)$. Once the agreement between e and μ is established, as will be shown in the next section, we then fit the two spectra simultaneously to extract branching ratios. We put lepton universality constraints in the simultaneous fit so that the three branching ratios (two primary ratios: $\mathcal{B}(b \to c\ell\nu)$ and $\mathcal{B}(b \to u\ell\nu)$, one secondary $\mathcal{B}(b \to c \to y\ell\nu)$) for electrons and muons are the same. In all the fits the allowed regions are 0.6–2.8 GeV/c for electrons and 1.3–2.8 GeV/c for muons.

3.8.1 Fit with ACCMM

In fitting to the ACCMM model we have five parameters to be determined. In addition to the branching ratios for $b \to c\ell\nu$, $b \to u\ell\nu$, and $b \to c \to x\ell\nu$, we must determine the best values of the Fermi momentum and the mass of the final-state charm quark. (In a separate step the corresponding quantities for the charm decays are determined by fitting to lower energy data.) Two other parameters of the model, the spectator quark mass, and the u-quark mass, cannot be adequately constrained. We therefore set them both to be 150 MeV/c^2. We vary the combination of P_F and m_c to find the best values of these parameters from the χ^2 distributions.

The parameters for secondary decays are obtained by using DELCO data [33] for $\psi(3770) \to D\bar{D}$ and $D \to X\ell\nu$. The two parameters to be determined are P_F for the D mesons and m_x for the final-state quark, which is mostly strange, with a small Cabibbo-suppressed d-quark component. We generate ACCMM shapes following the steps described in the previous section, except that we do not smear the theoretical spectra by the CLEO-II detector response matrices. The boost for the DELCO spectrum is the mass difference between $\psi(3770)$ and a $D\bar{D}$ pair. The parameter space we explore ranges from 25 to 500 MeV/c in 10 MeV/c steps for P_F, and 50 to 1000 MeV/c^2 in 25 MeV/c^2 steps for m_x. The best fit to the DELCO lepton inclusive spectrum (Fig. 3.11), yields the parameter values $P_F = 282 \pm 75$ MeV/c and $m_x = 50^{+200}_{-50}$ MeV/c^2. The s-

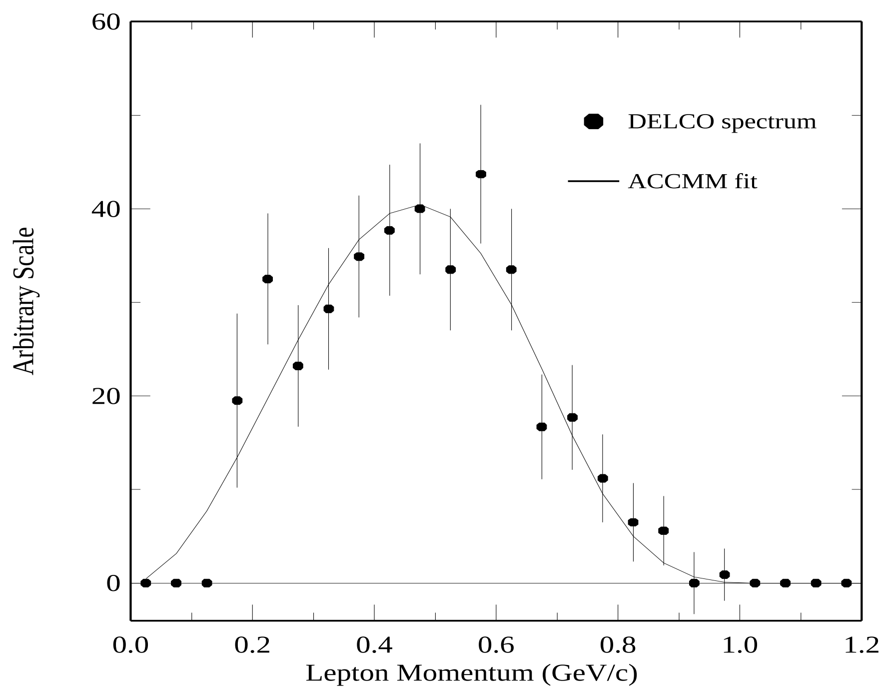

Figure 3.11: Fit to the DELCO lepton spectrum with the ACCMM model. The parameters for this fit are $P_F = 282 \pm 75$ MeV/c and $m_s = 50^{+200}_{-50}$ MeV/c^2.

quark mass is somewhat smaller than we would expect, although the uncertainty is large. This may have reflected the fact that the models do not work so well for charm decays.

To determine the parameters for primary decays we generate ACCMM shapes according to the procedure in the previous section. We vary P_F from 0 to 500 MeV/c in 5 MeV/c steps, and m_c from 1,000 to 2,000 MeV/c in 5 MeV/c steps. From the separate fits to electrons and muons, and from the simultaneous fit, we obtain three groups of values for the two parameters. They are listed in Table 3.7. We show in Fig. 3.12 the

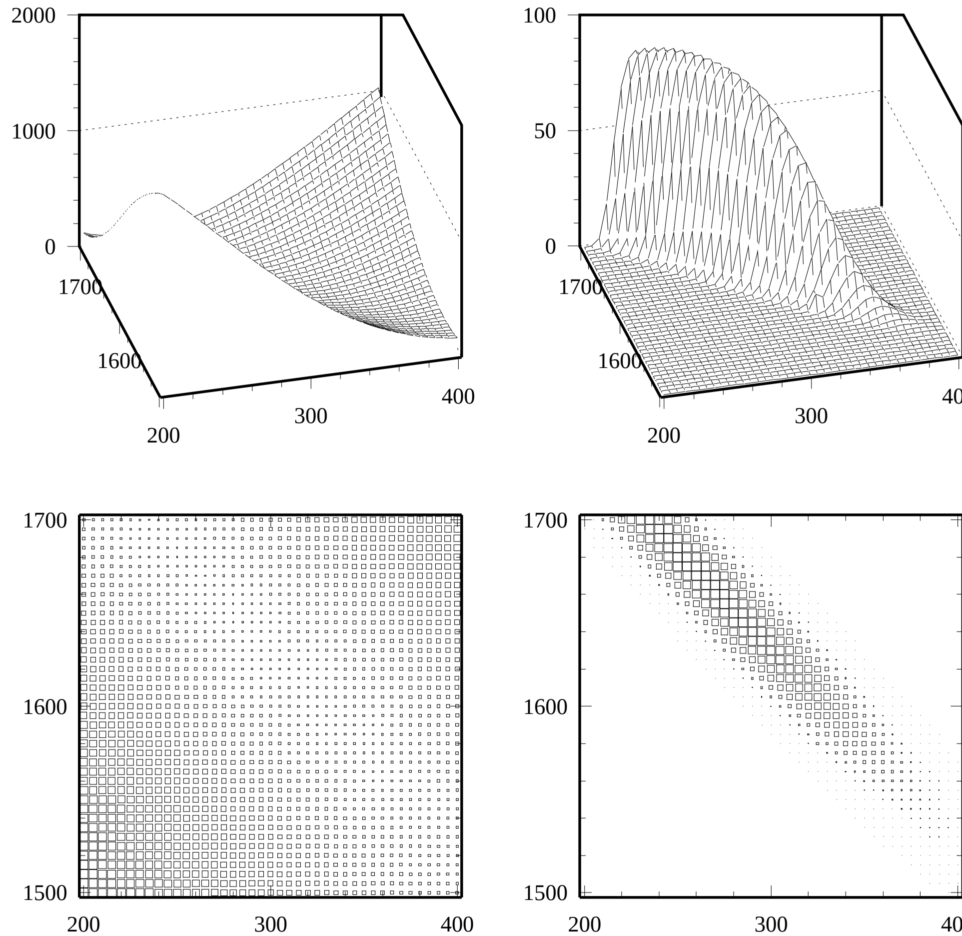

Figure 3.12: 3-D and 2-D views of the χ^2 (on the left) and confidence level in % (on the right) as a function of (P_F, m_c) for the $e + \mu$ simultaneous fits.

χ^2 and confidence level distributions in the (p_F, m_c) plane. Also, we show in Fig. 3.13 the χ^2 projections onto the P_F and m_c axes. Fig. 3.14 shows the result of the best simultaneous fit of the electron and muon spectra to the ACCMM model. The corresponding branching ratios are listed in Table 3.8, with only the statistical errors shown.

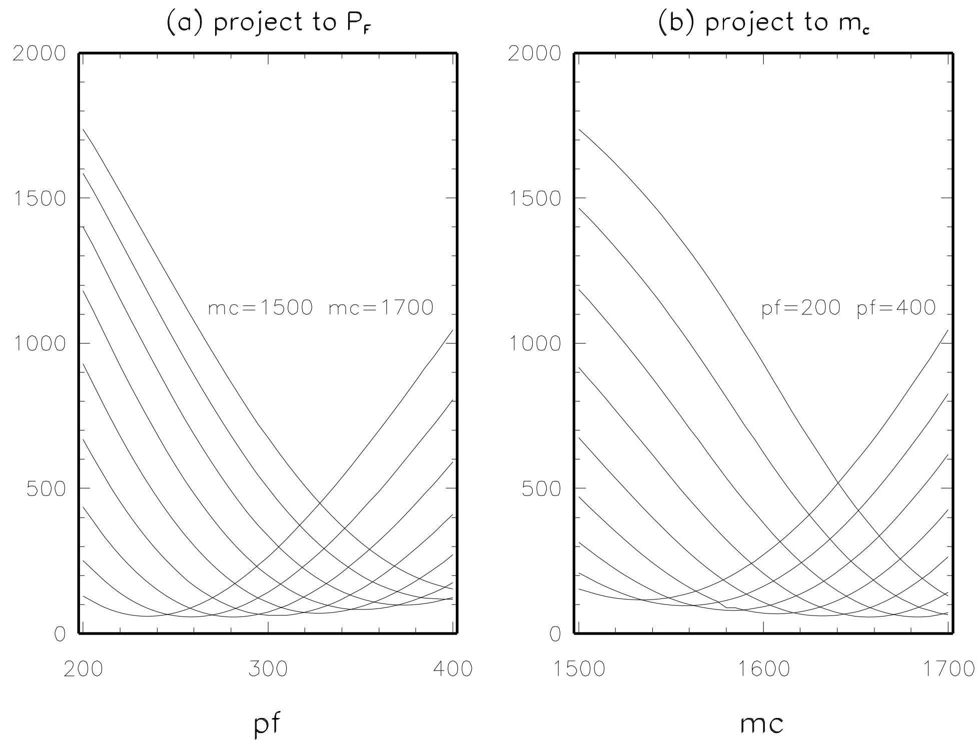

Figure 3.13: χ^2 projections. On the left, $\chi^2(P_F)$ for m_c in 25 MeV/c^2 steps is shown. On the right, $\chi^2(m_c)$ for P_F in 25 MeV/c steps is plotted.

In this table $\rho_{u/c}$ is the error correlation between the $b \to u\ell\nu$ and $b \to c\ell\nu$ branching fractions, which is used to determine the error in the overall inclusive branching ratios. Using the parameters from the best fit, we calculate the mass difference between the bottom and charm quark to be $m_b - m_c \approx 3.35\,\mathrm{GeV/c^2}$. This agrees with the QCD based heavy quark expansion prediction [7, 20, 34], though the definition of quark mass varies.

Table 3.7: ACCMM Parameters for B Decays

Fit	e	μ	$e+\mu$
P_F (MeV/c)	280 ± 25	245 ± 25	265 ± 25
m_c (MeV/c^2)	$1,650 \mp 25$	$1,690 \mp 25$	$1,670 \mp 25$

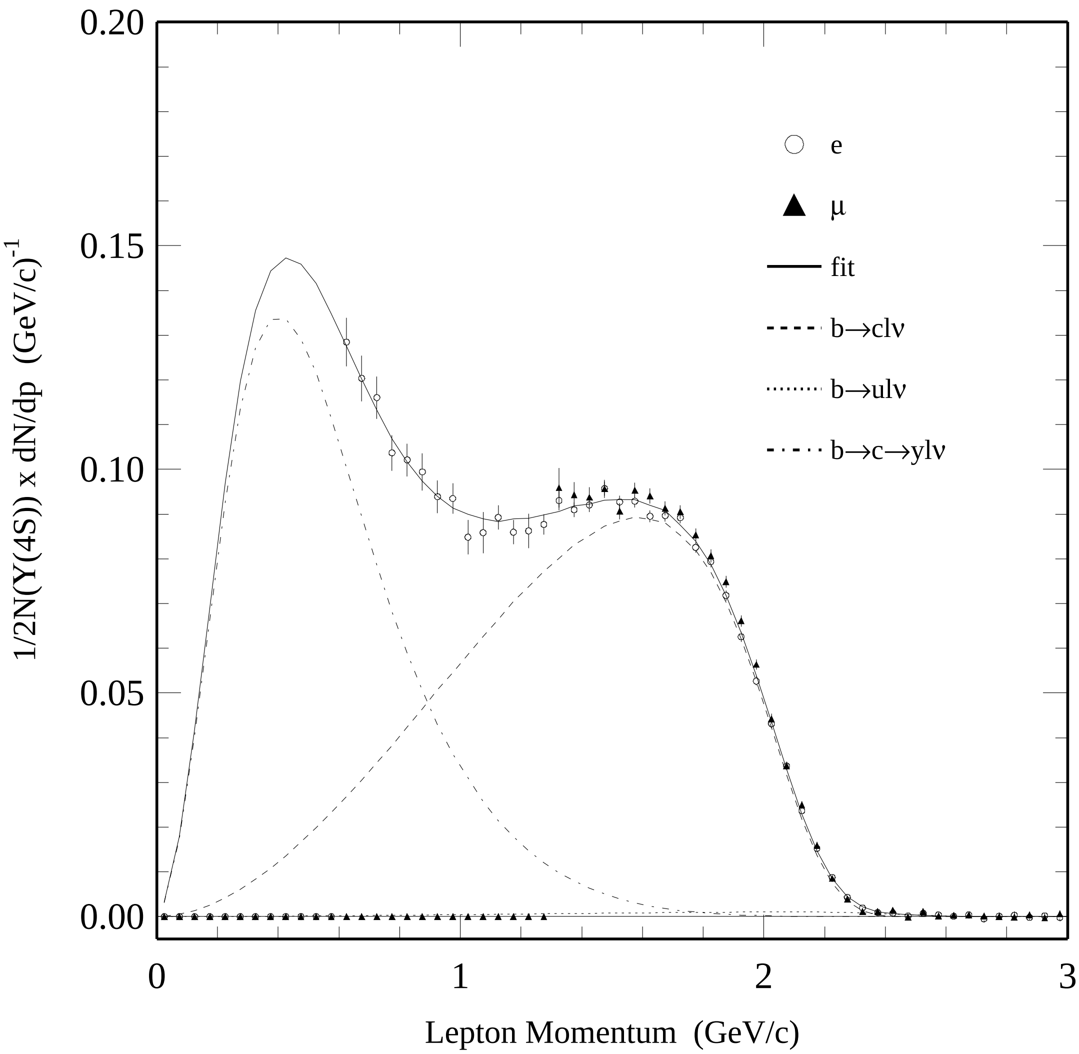

Figure 3.14: Fit to the $\Upsilon(4S)$ lepton spectra with the ACCMM model. This shows the electron part of the best simultaneous fit with the muon spectrum overlaid. In showing the fitting result, detector bremsstrahlung has been corrected for all spectra and functions. The parameters and branching ratios determined from this fit are listed in Table 3.7 and Table 3.8.

Table 3.8: Fitting Results

Model	Quantity	e	μ	$e+\mu$
ACCMM	$\chi^2/d.o.f.$	$31.3/44-3$	$24.7/30-2$	$59.9/74-3$
	$C.L.\%$	86.2	64.3	82.4
	$p_F\ MeV/c$	280	245	265
	$m_c\ MeV/c^2$	$1,650$	$1,690$	$1,670$
	$\mathcal{B}(b \to c\ell\nu)\%$	10.39 ± 0.06	10.46 ± 0.07	10.41 ± 0.04
	$\mathcal{B}(b \to u\ell\nu)\%$	0.12 ± 0.03	0.13 ± 0.04	0.14 ± 0.02
	$\mathcal{B}(b \to c \to x\ell\nu)\%$	8.96 ± 0.19	8.99	8.92 ± 0.18
	$\rho_{u/c}$	-0.62	-0.61	-0.61
	$\mathcal{B}(b \to x\ell\nu)\%$	10.51 ± 0.04	10.59 ± 0.05	10.56 ± 0.04
ISGW	$\chi^2/d.o.f.$	$102.7/44-3$	$66.4/30-1$	$169.9/74-3$
	$C.L.\%$	0.0	0.0	0.0
	$\mathcal{B}(b \to c\ell\nu)\%$	10.21 ± 0.06	10.28 ± 0.05	10.24 ± 0.05
	$\mathcal{B}(b \to u\ell\nu)\%$	0.03 ± 0.03	0.00	0.01 ± 0.03
	$\mathcal{B}(b \to c \to x\ell\nu)\%$	10.11 ± 0.20	10.11	10.19 ± 0.20
	$\rho_{u/c}$	-0.66	–	-0.66
	$\mathcal{B}(b \to x\ell\nu)\%$	10.25 ± 0.04	10.28 ± 0.05	10.26 ± 0.03
ISGW**	$\chi^2/d.o.f.$	$36.1/44-4$	$27.7/30-3$	$68.5/74-4$
	$C.L.\%$	64.6	42.9	52.9
	$\mathcal{B}(B \to D(D^*)\ell\nu)\%$	8.26 ± 0.10	8.37 ± 0.13	8.32 ± 0.08
	$\mathcal{B}(B \to D^{**}\ell\nu)\%$	2.49 ± 0.15	2.59 ± 0.20	2.50 ± 0.13
	$\mathcal{B}(b \to u\ell\nu)\%$	0.16 ± 0.04	0.11 ± 0.05	0.14 ± 0.03
	$\mathcal{B}(b \to c \to x\ell\nu)\%$	8.78 ± 0.25	8.78	8.73 ± 0.23
	$\rho_{D(D^*)/D^{**}}$	-0.86	-0.87	-0.87
	$\rho_{D(D^*)/u}$	-0.64	-0.66	-0.65
	$\rho_{D^{**}/u}$	0.38	0.40	0.39
	$\mathcal{B}(b \to c\ell\nu)\%$	10.75 ± 0.08	10.96 ± 0.11	10.82 ± 0.07
	$\mathcal{B}(b \to x\ell\nu)\%$	10.91 ± 0.09	11.07 ± 0.12	10.96 ± 0.07
	$\frac{\mathcal{B}(B \to D^{**}\ell\nu)}{\mathcal{B}(b \to c\ell\nu)}\ \%$	23.2 ± 1.3	23.6 ± 1.7	23.1 ± 1.1

3.8.2 Fit with ISGW

Fitting with the original ISGW model is straightforward, since the branching ratios are the only free parameters to be determined. The secondary lepton spectrum is already fixed by the model in the D rest frame and by its boost, the D spectra from CLEO data. The results are listed in Table 3.8. The fit to the muon spectrum favored a small negative value for $\mathcal{B}(b \to u\ell\nu)$ within errors, we thus forced it to be zero in the fit. It is found that the ISGW fits give unsatisfactory confidence levels, however, as is shown in Table 3.8 and Fig. 3.15. This implies that the model needs to be modified to fit the shape of our data. As originally presented, the ISGW model predicts the proportion of the three categories of exclusive decays to be $\mathcal{B}(B \to D\ell\nu) : \mathcal{B}(B \to D^*\ell\nu) : \mathcal{B}(B \to D^{**}\ell\nu) = 27\% : 62\% : 11\%$. $\mathcal{B}(B \to D^*\ell\nu)$ has been measured to be 4–5.5% [35] by fully or partially reconstructing the missing mass to match the undetected neutrino. The latest CLEO result gives $\mathcal{B}(\bar{B}^0 \to D^{*0}\ell^-\bar{\nu}) = (4.5 \pm 0.44 \pm 0.44)\%$. Similarly, $\mathcal{B}(B \to D\ell\nu)$ is measured to be $(1.7 \pm 0.4)\%$ [1]. Evidence for $B \to D^{**}\ell\nu$ has only been seen in one or two of the D^{**} states. It is the least understood, and not all of the D^{**} states have been well measured or even observed yet. While the model has difficulty in fitting the lepton spectra, its vector-to-pseudoscalar ratio $\mathcal{B}(B \to D^*\ell\nu)/\mathcal{B}(B \to D\ell\nu) = 2.3$ is in good agreement with results from exclusive measurements. We therefore make a very simple modification of the model by fixing this ratio to the model prediction and allowing the $B \to D^{**}\ell\nu$ branching fraction to float in the fit. This technique was first used for a previous CLEO measurement, and was dubbed ISGW** [11].

With this modification, the χ^2 value improves, yielding much higher confidence levels, as is shown in Table 3.8 and Fig. 3.16. It is possible to relax the constraints of the ISGW further, by allowing the proportions of $B \to D\ell\nu$, $B \to D^*\ell\nu$, and $B \to D^{**}\ell\nu$ to be completely free, while constrain $B \to u\ell\nu$ to measured values of $|V_{ub}/V_{cb}|$ [36]. Such free fit to the electron spectrum gives branching ratios very close to those from ISGW** with comparable errors and confidence level. It favors a vector-to-pseudoscalar

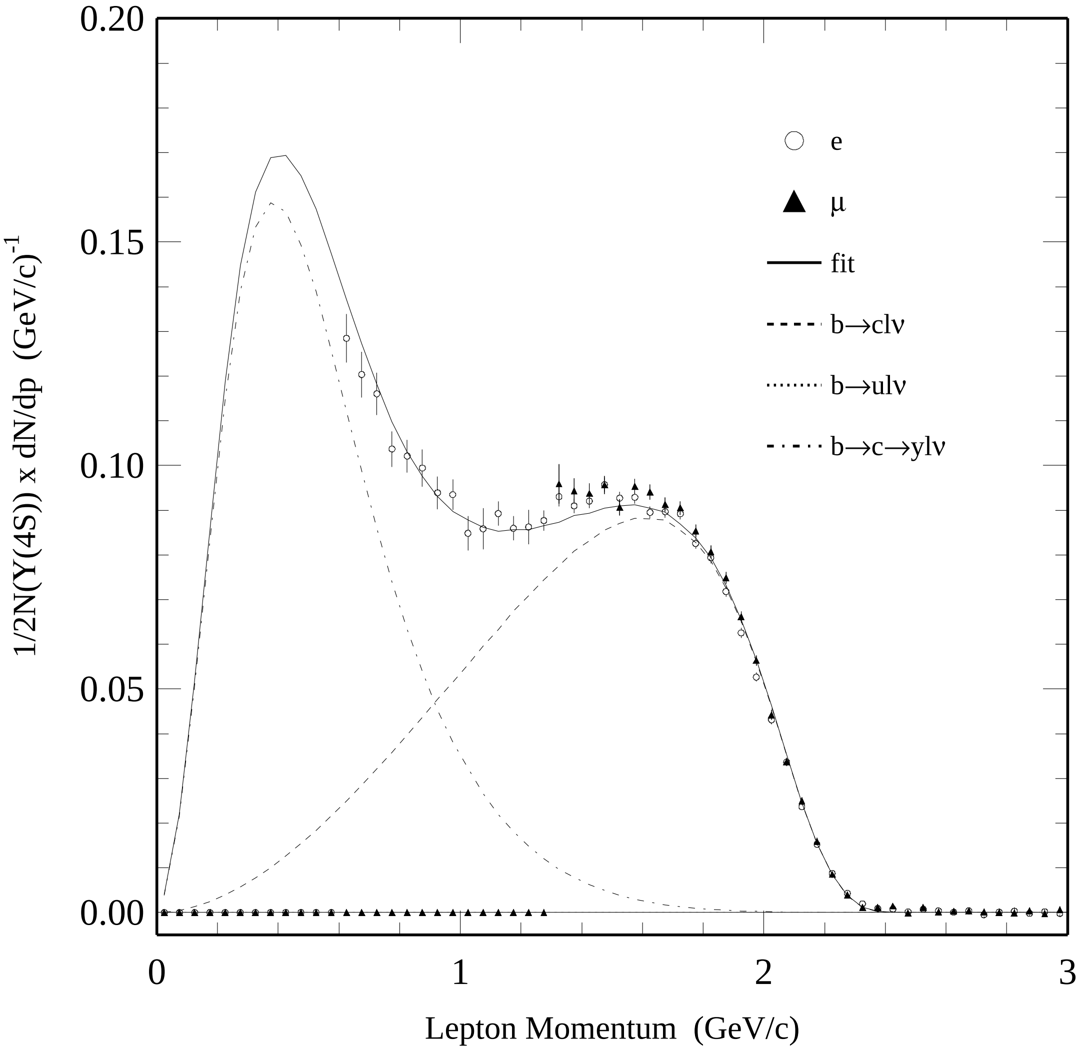

Figure 3.15: Fit to lepton spectra with the original ISGW model. This shows the electron part of the simultaneous fit with the muon spectrum overlaid. In showing the fitting result, detector bremsstrahlung has been corrected for all spectra and functions. The branching ratios determined from this fit are listed in Table 3.8.

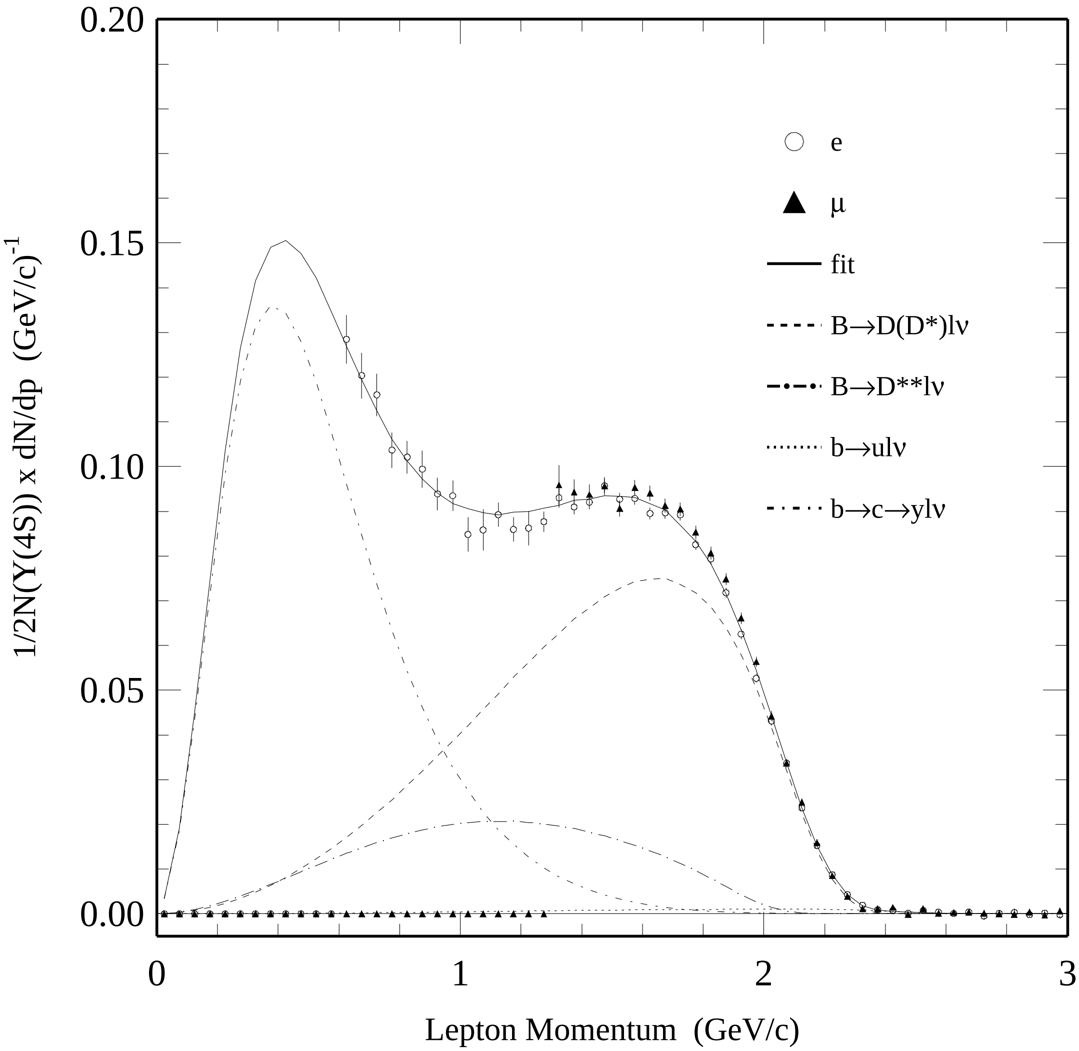

Figure 3.16: Fit to lepton spectra with the ISGW** model, which treats the proportion of $B \to D^{**}\ell\nu$ as a free parameter. This shows the electron part of the simultaneous fit with the muon spectrum overlaid. In showing the fitting result, detector bremsstrahlung has been corrected for all spectra and functions. The branching ratios from this fit are listed in Table 3.8. The fraction of $B \to D^{**}\ell\nu$ from this fit is $(23 \pm 1)\%$ (statistical error only).

ratio exactly 2.3 as in the ISGW model. But the muon spectrum favors a much lower fraction of $B \to D\ell\nu$ decays compared to the measured $\mathcal{B}(B \to D\ell\nu)$. This clearly demonstrates that our inclusive data spectra alone cannot determine these fractions. We therefore do not change the D and D^* parts of the model, keeping both the spectral shapes and the vector-to-pseudoscalar ratio of 2.3.

The amount of D^{**} favored by the ISGW** fits is $(23 \pm 1)\%$ (statistical error only), considerably different from the 11% in the original ISGW model. One must interpret this result cautiously, however, because of the possibility of higher spin states and non-resonant contributions. which are not included in the model. The systematic error on the D** fraction will be estimated in the next section.

3.8.3 $b \to u\ell\nu$ from the Fits

The $b \to u\ell\nu$ fractions are positive for most of the cases considered, except the ISGW muon fit, which is consistent with zero (Table 3.8). If we force $\mathcal{B}(b \to u\ell\nu) = 0$ in the fits, the confidence levels drop in all cases. To understand the implication, we first check the end-point region of the spectra and fits, which are shown in Fig. 3.17. They are consistent with the CLEO $b \to u\ell\nu$ lepton spectrum end-point analysis [36]. This consistency check is the prerequisite for extracting $|V_{ub}/V_{cb}|$ at the end of this chapter. Furthermore, we can use the results of $|V_{ub}/V_{cb}|$ from the end-point analysis to constrain $\mathcal{B}(b \to u\ell\nu)$ in our fits (Table 3.9). The results are consistent with those in Table 3.8, but with reduced degree of freedom.

3.8.4 Inclusive Semileptonic Branching Ratios

The inclusive B semileptonic branching ratios from the fits are summarized in Table 3.10 with statistical errors only. The results are consistent with lepton universality within statistical errors for each model.

Table 3.9: $|V_{ub}/V_{cb}|$ constrained fits compared to free fits.

Model	Quantity	constrained	free
ACCMM	$\chi^2/d.o.f.$	$60.4/74-2$	$59.9/74-3$
	$C.L.\%$	83.4	82.4
	$\mathcal{B}(b\to c\ell\nu)\%$	10.43 ± 0.03	10.41 ± 0.04
	$\mathcal{B}(b\to u\ell\nu)\%$	0.13	0.14 ± 0.02
	$\mathcal{B}(b\to c\to x\ell\nu)\%$	8.91 ± 0.18	8.92 ± 0.18
	$\mathcal{B}(b\to x\ell\nu)\%$	10.56 ± 0.03	10.56 ± 0.04
ISGW	$\chi^2/d.o.f.$	$179.7/74-2$	$169.9/74-3$
	$C.L.\%$	0.0	0.0
	$\mathcal{B}(b\to c\ell\nu)\%$	10.15 ± 0.03	10.24 ± 0.05
	$\mathcal{B}(b\to u\ell\nu)\%$	0.10	0.01 ± 0.03
	$\mathcal{B}(b\to c\to x\ell\nu)\%$	10.25 ± 0.20	10.19 ± 0.20
	$\mathcal{B}(b\to x\ell\nu)\%$	10.25 ± 0.03	10.26 ± 0.03
ISGW**	$\chi^2/d.o.f.$	$69.7/74-3$	$68.5/74-4$
	$C.L.\%$	52.2	52.9
	$\mathcal{B}(B\to D(D^*)\ell\nu)\%$	8.38 ± 0.08	8.32 ± 0.08
	$\mathcal{B}(B\to D^{**}\ell\nu)\%$	2.45 ± 0.14	2.50 ± 0.13
	$\mathcal{B}(b\to u\ell\nu)\%$	0.10	0.14 ± 0.03
	$\mathcal{B}(b\to c\to x\ell\nu)\%$	8.78 ± 0.24	8.73 ± 0.23
	$\rho_{D(D^*)/D^{**}}$	-0.93	-0.87
	$\mathcal{B}(b\to c\ell\nu)\%$	10.83 ± 0.07	10.82 ± 0.07
	$\mathcal{B}(b\to x\ell\nu)\%$	10.93 ± 0.07	10.96 ± 0.07
	$\frac{\mathcal{B}(B\to D^{**}\ell\nu)}{\mathcal{B}(b\to c\ell\nu)}\%$	22.6 ± 1.2	23.1 ± 1.1

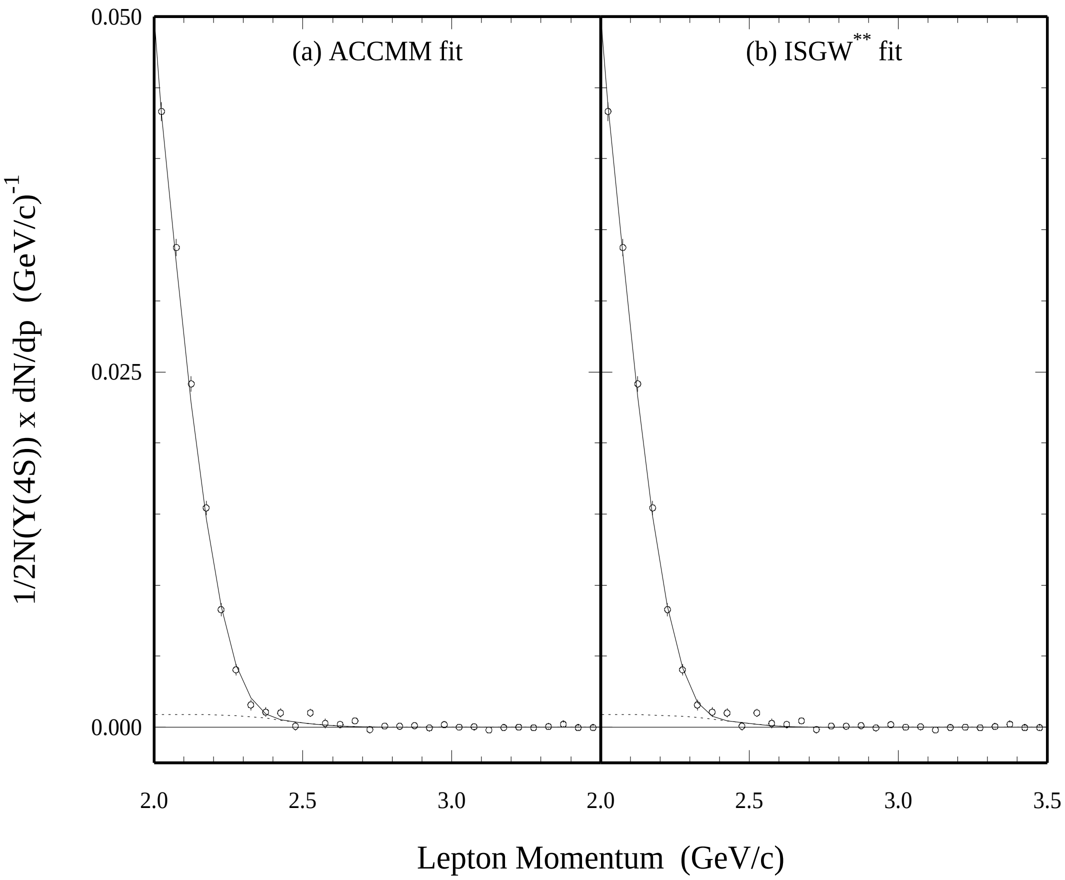

Figure 3.17: Lepton spectrum and fit with ACCMM (a), and ISGW** (b) in the end-point region. The spectrum shown is the average of electrons and muons. The solid curves are the fits while the dashed show the $b \to u\ell\nu$ part of the fits.

3.9 Systematic Studies

We study the systematic errors with the following procedure. For each source of systematic error we vary this quantity up and down by the amount of uncertainty, and repeat the analysis procedure to obtain the results from the fits. The bigger of the two is taken to be the systematic error due to this source. These uncertainties are mostly uncorrelated, so all contributing errors are summed in quadrature to determine the combined systematic error. We list these sources, their uncertainties, and the associated systematic errors in the branching ratios in Table 3.11.

Table 3.10: $\mathcal{B}(B \to X\ell\nu)(\%)$ for $\ell = e$, μ and combined.

Model	e	μ	$e+\mu$
ACCMM	10.51 ± 0.04	10.59 ± 0.05	10.56 ± 0.04
ISGW	10.25 ± 0.04	10.28 ± 0.05	10.26 ± 0.03
ISGW**	10.91 ± 0.09	11.07 ± 0.12	10.96 ± 0.07

In this table, we have made a conservative estimate of the uncertainty in fake rates, taking into account the difference in the two measurements of fake rates in Chapter 2. The uncertainty in $\epsilon_{\mu ID}$ has been discussed in Chapter 2. That for ϵ_{eID} is estimated from the difference in the efficiency for finding electrons from radiative Bhabha events before and after they are embedded in hadronic events. The systematic errors in the $J/\psi(\psi^{'})$ correction include the internal radiation of the $J/\psi(\psi^{'})$. The uncertainty in π^0 Dalitz decays is estimated by using Monte Carlo. This includes a small contribution from uncertainty of the η Dalitz decay correction.

The error in the photon conversion correction is obtained by using a simple veto without applying the efficiency correction as was described earlier. For the deviation of $R_{\mu/e}$ from 1 we estimate the error by forcing $R_{\mu/e} = 1$. A conservatively estimated beam energy shift of 1 MeV would cause a change of 25 MeV/c in the boost of the B. This is also included in the systematic error.

The dependence of the fits on the minimum momentum is studied by changing the low end of the fitting range from 0.5 GeV/c to 1.0 GeV/c in 50 MeV/c steps for electrons, and from 1.3 GeV/c to 1.8 GeV/c in 50 MeV/c steps for muons. The fitting results are quite stable. The difference between our standard result and the average of all the alternative fits is taken to be the systematic error associated with the fitting range. The effect due to the uncertainty in the shape of the secondary spectrum was conservatively estimated by shifting the boosted theoretical curves up and down by 0.05 GeV/c.

Table 3.11: Systematic Errors

Source X	$\Delta X/X$ % or as noted	$\Delta\mathcal{B}(b \to c\ell\nu)$ %	$\Delta\mathcal{B}(b \to u\ell\nu)$ %	$\Delta\mathcal{B}(b \to x\ell\nu)$ %
f_e	± 50	0.045	0.010	0.035
f_μ	± 25	0.012	0.006	0.018
ϵ_{eID}	± 2.0	0.134	0.002	0.133
$\epsilon_{\mu ID}$	± 2.0	0.083	0.002	0.082
$\epsilon_{tracking}$	± 1.0	0.105	0.002	0.107
$\alpha(\mathcal{L})$	± 0.5	0.008	0.009	0.017
$J/\psi(\psi')$	± 30	0.035	0.013	0.040
$\pi^0(\eta)$	± 25	0.008	0.003	0.010
τ	± 30	0.015	0.003	0.015
γ	± 50	0.010	0.001	0.010
D_s	± 30	0.003	0.000	0.002
Λ_c	± 30	0.001	0.000	0.001
$R_{\mu/e}$	forced to 1	0.001	0.000	0.001
E_{beam}	± 1 MeV	0.020	0.030	0.040
p_e^{min}	$+0.5$ GeV/c	0.032	0.005	0.029
p_μ^{min}	$+0.5$ GeV/c	0.040	0.006	0.037
$b \to c \to y\ell\nu$ shape	± 0.05 GeV/c	0.043	0.007	0.044
EW	± 15	0.040	0.002	0.039
Sum		0.215	0.038	0.217

The systematic error in the inclusive branching ratio is clearly dominated by the uncertainties in the efficiency for tracking and lepton identification. In the case of $b \to u\ell\nu$ both the B boost and the J/ψ correction contribute sizable uncertainties. The overall systematic error for the primary B-semileptonic branching fraction is 0.22%, and that for the secondary 1.64%. The later is summarized in Table 3.12.

It is beyond the scope of this analysis to assess the theoretical uncertainties of the models considered. It is appropriate, however, to assess the systematic errors in our determination of the free parameters in these models.

The lack of knowledge of the D^{**} states makes it very difficult to clearly define the fraction of $B \to D^{**}\ell\nu$. This fraction is sensitive to our understanding of the

Table 3.12: Systematic Errors in the Fraction of $D^{**}\ell\nu$ and $\mathcal{B}(b \to c \to y\ell\nu)$.

Source X	$\Delta X/X$ % or as noted	$\Delta\mathcal{B}(b \to c \to y\ell\nu)$ %	$\Delta\frac{\mathcal{B}(B \to D^{**}\ell\nu)}{\mathcal{B}(b \to c\ell\nu)}$ %
f_e	± 50	1.267	1.62
f_μ	± 25	0.011	0.04
ϵ_{eID}	± 2.0	0.260	0.53
$\epsilon_{\mu ID}$	± 2.0	0.069	0.52
$\epsilon_{tracking}$	± 1.0	0.096	0.01
$\alpha(\mathcal{L})$	± 0.5	0.067	0.11
$J/\psi(\psi')$	± 30	0.026	0.18
$\pi^0(\eta)$	± 25	0.287	0.19
τ	± 30	0.220	0.42
γ	± 50	0.861	0.54
D_s	± 30	0.329	0.11
Λ_c	± 30	0.030	0.03
$R_{\mu/e}$	froced to 1	0.002	0.01
E_{beam}	± 1 MeV	0.001	0.01
p_e^{min}	$+0.5$ GeV/c	—	1.31
p_μ^{min}	$+0.5$ GeV/c	—	0.30
$b \to c \to y\ell\nu$ shape	± 0.05 GeV/c	—	1.28
EW	± 15	0.019	0.40
$D^*\ell\nu/D\ell\nu$	2.12-3.54	—	4.67
Sum		1.635	5.40

form factors for $B \to D\ell\nu$ and $B \to D^*\ell\nu$ and the uncertainties in the charm contribution to the inclusive spectra. In addition to the other contributions, we vary the vector/pseudoscalar ratio $D^*\ell\nu/D\ell\nu$ within the current experimental bound as listed in Table 3.12. It dominates the estimated 5.4% uncertainty. Again, exclusive measurements are needed to study the decays $B \to D^{**}\ell\nu$.

3.10 Branching Fractions and CKM Matrix Elements

We summarize the B semileptonic branching ratios from the simultaneous fits to electrons and muons in Table 3.13, where the errors are statistical and systematic, respectively. From these results, we can extract the CKM matrix elements $|V_{cb}|$ and $|V_{ub}/V_{cb}|$.

Table 3.13: Summary of B Semileptonic Branching Ratios

Model	$\mathcal{B}(b \to c\ell\nu)\%$	$\mathcal{B}(b \to u\ell\nu)\%$	$\mathcal{B}(b \to x\ell\nu)\%$
ACCMM	$10.41 \pm 0.04 \pm 0.22$	$0.14 \pm 0.02 \pm 0.04$	$10.56 \pm 0.04 \pm 0.22$
ISGW	$10.24 \pm 0.05 \pm 0.22$	$0.01 \pm 0.03 \pm 0.04$	$10.26 \pm 0.03 \pm 0.22$
ISGW**	$10.82 \pm 0.07 \pm 0.22$	$0.14 \pm 0.03 \pm 0.04$	$10.96 \pm 0.07 \pm 0.22$

The semileptonic width of the B meson is given by the sum of the two partial widths:

$$\Gamma(B \to X\ell\nu) = \Gamma(b \to c\ell\nu) + \Gamma(b \to u\ell\nu), \tag{3.6}$$

where

$$\Gamma(b \to q\ell\nu) = \frac{\mathcal{B}(b \to q\ell\nu)}{\tau_B} = \gamma_q |V_{qb}|^2, \tag{3.7}$$

for $q = c$ or u. The factor γ_q must be determined theoretically. From the branching ratios in Table 3.13 and the average B lifetime [52], $\tau_B = (1.537 \pm 0.021) \times 10^{-12}$ s, we calculate the matrix element V_{cb} and the ratio $|V_{ub}/V_{cb}|$ with different models, and list them in Table 3.14. The first error in each matrix element is due to the error in

Table 3.14: CKM Matrix Elements

Model	$\gamma_c(ps^{-1})$	$\mathcal{B}(b \to c\ell\nu)\%$	$\lvert V_{cb}\rvert$
ACCMM	39.2 ± 7.8	$10.41 \pm 0.04 \pm 0.22$	$0.0416 \pm 0.0005 \pm 0.0042$
ISGW	41.3 ± 8.3	$10.24 \pm 0.05 \pm 0.22$	$0.0402 \pm 0.0005 \pm 0.0040$
ISGW**	46.5 ± 9.3	$10.82 \pm 0.07 \pm 0.22$	$0.0389 \pm 0.0005 \pm 0.0039$
Model	γ_u/γ_c	$\mathcal{B}(b \to u\ell\nu)\%$	$\lvert V_{ub}/V_{cb}\rvert$
ACCMM	2.12 ± 0.42	$0.14 \pm 0.02 \pm 0.04$	$0.081 \pm 0.013 \pm 0.008$
ISGW**	0.93 ± 0.19	$0.14 \pm 0.03 \pm 0.04$	$0.116 \pm 0.022 \pm 0.012$

our branching ratio measurement and in the measured B lifetime. The second error corresponds to an assumed 20% uncertainty in γ_q, as suggested by the authors. In calculating $|V_{ub}/V_{cb}|$ some of the systematic uncertainties cancel. The values for $|V_{cb}|$ are consistent with the previous inclusive measurement, with slightly smaller statistical errors. The $|V_{ub}/V_{cb}|$ values are consistent with the lepton end-point $b \to u\ell\nu$ analysis.

Recently, a less model dependent approach has been proposed [34] to measure $|V_{cb}|$ from the inclusive semileptonic branching ratio. This will be discussed in Chapter 4.

3.11 Conclusion

We have made a new measurement of the inclusive B semileptonic branching fractions by fitting the inclusive lepton spectra from $\Upsilon(4S)$ decays using 2.057 fb^{-1} of data collected by CLEO-II. With this substantially larger data sample and upgraded detector we have improved this measurement both statistically and systematically. We find $\mathcal{B}(B \to X\ell\nu) = (10.56 \pm 0.04 \pm 0.22)\%$ with the refined quark model by Altarelli *et al.,* and $\mathcal{B}(B \to X\ell\nu) = (10.96 \pm 0.07 \pm 0.22)\%$ with a modified version of the form factor model by Isgur *et al.,* in which the $D^{**}l\nu$ fraction is allowed to float. The fraction of $B \to D^{**}\ell\nu$ from this fit is $(23 \pm 1 \pm 5)\%$, somewhat larger than the model prediction. The fit to the original Isgur model yields a lower branching ratio, $\mathcal{B}(B \to X\ell\nu) = (10.26 \pm 0.03 \pm 0.22)\%$, with a higher χ^2. Our result supports previous measurement with improved precision. The good agreement of the electron and muon results is a convincing demonstration of the performance and our understanding of the CLEO-II detector. Further progress requires reduction of the systematic and theoretical uncertainties in this measurement. In the next chapter we describe a complementary analysis which uses lepton-tagged B-decay events to achieve such improvements.

Chapter 4

Measurement with Lepton Tags

Abstract We present a new measurement of $\mathcal{B}(B \to Xe\nu)$ with dilepton events from $2.057 fb^{-1}$ of $\Upsilon(4S)$ data collected with the CLEO-II detector. In events with a high momentum lepton tag and an electron we use charge and kinematic correlations to separate the electron spectra of B decays and secondary charm decays. With a small extrapolation to account for the undetected part of the spectrum at low momentum, we obtain $\mathcal{B}(B \to Xe\nu) = (10.46 \pm 0.17 \pm 0.43)\%$. This measurement is largely independent of theoretical models and assumptions about possible non-$B\bar{B}$ decays of the $\Upsilon(4S)$. The resulting CKM matrix element $|V_{cb}|$ is $0.041 \pm 0.001 \pm 0.002$. By measuring the ratio of inclusive electrons and tagged electrons, we found that the non-$B\bar{B}$ fraction is less than 4% at 95% C.L., assuming no lepton production from such decays [37].

4.1 Introduction

The semileptonic branching fraction of the B mesons has been an unsettled question, as experimental measurements have consistently been smaller than theoretical predictions [1, 6]. Recent theoretical developments, based on heavy quark expansion in QCD [7], reinforce the conclusion that this fraction cannot be accommodated within the framework of the Standard Model at a level below 12.5%. Our latest result from CLEO-II data, on the other hand, confirms the previous measurements with greater statistical significance and improved systematics [28], as was described in Chapter 3. By fitting the inclusive lepton spectra from Υ(4S) decays to the refined quark model of Altarelli *et al.* [13], for example, we obtain $\mathcal{B}(B \to X\ell\nu) = (10.56 \pm 0.04 \pm 0.22)\%$. With a modified version of the form-factor model of Isgur *et al.* [15], in which the fraction of $B \to D^{**}\ell\nu$ is allowed to float, we find $\mathcal{B}(B \to X\ell\nu) = (10.96 \pm 0.07 \pm 0.22)\%$. Further progress on this pressing issue requires alternative approaches, with reduced systematic uncertainty. In this chapter we describe a new analysis using dilepton events in CLEO-II data.

The inclusive lepton spectrum from Υ(4S) decays is shown in Fig. 3.14. It consists of mainly two parts: primary leptons from semileptonic B decays, and secondary leptons from the decays of charmed mesons produced in B decays. In the inclusive spectrum analysis, the primary part is determined by fitting the spectrum with theoretical models that separately describe the primary and secondary semileptonic decays. This introduces model dependence into the measured B semileptonic branching ratio. In addition, it requires the assumption that all the Υ(4S) mesons decay to $B\bar{B}$ pairs, when we normalize the lepton spectra to the total number of B mesons.

Sensitivity to these two effects can be reduced by using an additional lepton in an Υ(4S) event as a tag. Previous CLEO measurements [11] used events with two leptons above 1.4 GeV/c, in which both B mesons decay semileptonically. This eliminates the need for models in calculating the momentum acceptance, and allows the setting of an upper limit on non-$B\bar{B}$ decays of the Υ(4S). Extrapolation to the region below 1.4 GeV/c still requires models, however.

In this analysis, we also use high momentum leptons to tag semileptonic decays of one of the two B mesons in each event. In events with lepton tags, we select additional electrons with momenta as small as 0.6 GeV/c. We are able to separate the primary electrons from the secondary by utilizing the charge correlations between the tag leptons and the signal electrons. The significant background from events in which both the tag lepton and the electron are from the same B can be removed by distinguishing the kinematics of signal and background events. In particular, the opening angle between the tag lepton and additional electron has distinct features when both of them are from the same B, as compared to the case when they are from opposite B mesons. This was demonstrated in a recent ARGUS paper [38], as well as an earlier CLEO analysis using lepton-kaon correlations [39]. Stimulated by these analyses, we explored the correlations in two dimensions to optimize the separation in a measurement of the electron spectrum for B decays. The resulting B semileptonic branching ratio is largely independent of theoretical models and of assumptions about possible non-$B\bar{B}$ decays of the $\Upsilon(4S)$.

In what follows, we first analyze the charge and kinematic correlations in dilepton events from $\Upsilon(4S)$ decays, and then show the data yields and background corrections. Next, we obtain the electron spectra of primary and secondary decays and the resulting branching ratios. Last, we study systematic errors and conclude.

4.2 Analysis with Dilepton Events

The idea of this analysis is to use a high momentum lepton to tag the semileptonic decay of one of the two B mesons in an $\Upsilon(4S)$ event and observe the semileptonic decay of the second B. The tag lepton, with a momentum above 1.4 GeV/c, is most likely from semileptonic B decay (Fig. 3.14). The additional lepton can be from semileptonic decay of the second B in the event, or, especially at lower energies, it can be from the semileptonic decay of a D meson produced in the decay of either B. To develop the specific procedure to distinguish these cases, we have studied charge and kinematic correlations for dilepton events in a sample of 5 million $\Upsilon(4S) \rightarrow B\bar{B}$ Monte Carlo events.

4.2.1 Charge Correlations in Dilepton Events

Leptons in $\Upsilon(4S)$ events come mainly from two types of semileptonic decays: primary ($B \to X\ell\nu$) and secondary ($B \to DX$, $D \to Y\ell\nu$). The combinations of primary and secondary leptons which contribute to the dilepton yields are summarized in Table 4.1. In this table, f_+ and f_0 stand for the production fractions in $\Upsilon(4S)$ decays of charged

Table 4.1: Charge Correlations in Dilepton $\Upsilon(4S)$ Events

Decays	Prob.	$b \to x\ell\nu$ sign	$b \to c \to y\ell\nu$ sign	$b \to c \to y\ell\nu$ side
$\bar{D}\ell^+\nu \leftarrow B^+B^- \to D\ell^-\bar{\nu}$			unlike	same
$\downarrow$ $\qquad\qquad$ $\downarrow$	f_+	unlike		
$\bar{Y}\ell^-\bar{\nu}$ $\qquad$ $Y\ell^+\nu$			like	oppo.
$\bar{D}\ell^+\nu \leftarrow B^0\bar{B}^0 \to D\ell^-\bar{\nu}$			unlike	same
$\downarrow$ $\qquad\qquad$ $\downarrow$	$f_0(1-\chi_0)$	unlike		
$\bar{Y}\ell^-\bar{\nu}$ $\qquad$ $Y\ell^+\nu$			like	oppo.
$D\ell^-\nu \leftarrow \bar{B}^0\bar{B}^0 \to D\ell^-\bar{\nu}$			unlike	same
$\downarrow$ $\qquad\qquad$ $\downarrow$	$\frac{1}{2}f_0\chi_0$	like		
$Y\ell^+\nu$ $\qquad$ $Y\ell^+\nu$			unlike	oppo.
$\bar{\mathrm{D}}\ell^-\nu \leftarrow B^0B^0 \to \bar{D}\ell^-\bar{\nu}$			unlike	same
$\downarrow$ $\qquad\qquad$ $\downarrow$	$\frac{1}{2}f_0\chi_0$	like		
$\bar{Y}\ell^-\bar{\nu}$ $\qquad$ $\bar{Y}\ell^-\bar{\nu}$			unlike	oppo.

and neutral B mesons, respectively. The terms "like" and "unlike" are used to indicate the relationship between the signs of the electric charges of the two leptons. If the two leptons originate from the same B meson, they are called "same side", otherwise they are "opposite side". The mesons carrying a charm quark (D^+, D^0) are represented by D, while those with an anti-charm quark are $\bar{D}$.

The presence in an $\Upsilon(4S)$ event of a lepton with momentum above 1.4 GeV/c indicates that at least one of the two B mesons decayed semileptonically, since only primary leptons contribute to the high momentum region. In addition, the sign of the lepton's electric charge tags the flavor of its parent B meson. For example, if it is positive (ℓ^+), we know that it is from a B meson ($B = \bar{b}q, \bar{b} \to x\ell^+\nu_\ell$). For $\Upsilon(4S) \to B\bar{B}$ (Fig. 4.1a), we expect any additional primary electron to be negatively charged, since this corresponds to the semileptonic decay of a $\bar{B}$ meson ($\bar{B} = b\bar{q}$, $b \to xe^-\bar{\nu_e}$). We could find an e^+ instead, however, and would naturally interpret this as an evidence for a secondary decay ($b \to c \to ye^+\nu_e$). The charge correlations for $B\bar{B}$ events are thus very clear: primary electrons are unlike-sign, and secondary electrons can give like-sign. There is one complication to this simple picture, however. Semileptonic decays of both a B (or $\bar{B}$) meson and the D (or $\bar{D}$) into which it decays lead to an additional unlike-sign contribution. This unlike-sign, same-B background is quite large, and constitutes a major background. Fortunately, these events can be suppressed with kinematic cuts, as is described in the next section.

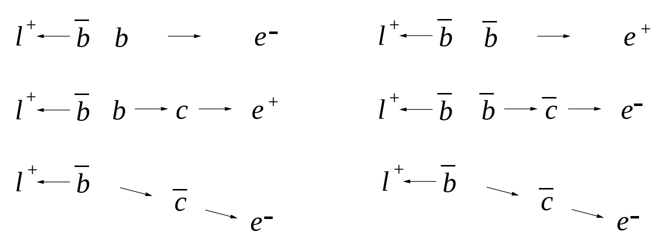

(a). Unmixed (b). Mixed

Figure 4.1: Charge correlations with a high-momentum tag ℓ^+, and an additional e^+ or e^-, as described in the text.

This scenario happens most of the time, but does not hold when $B^0 - \bar{B}^0$ mixing occurs. A neutral B meson can oscillate (mix) into its anti-particle through the two box diagrams in Fig. 4.2. When one of the two neutral B mesons oscillates we have in this event decays of B^0B^0 or $\bar{B}^0\bar{B}^0$, instead of $B^0\bar{B}^0$. In this case (Fig. 4.1b), the charge correlations are flipped, and primary electrons are like-sign, while secondaries are unlike-sign. The probability of $B^0 - \bar{B}^0$ mixing for neutral B events has been measured to be

$\chi_0 \approx 16\%$ [40]. Since the fraction of neutral B pairs produced at $\Upsilon(4S)$ is $f_0 \approx 50\%$, the portion of mixed events in our tagged sample is therefore $\chi = f_0\chi_0 \approx 8\%$. This in turn reduces the unmixed portion to $1 - \chi \approx 92\%$.

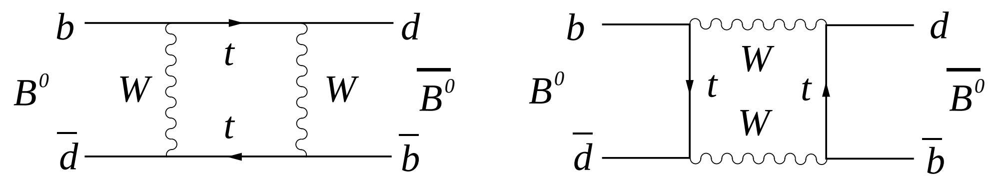

Figure 4.2: $B^0 - \bar{B}^0$ mixing diagrams.

The above discussion relies on the prohibition at $\Upsilon(4S)$ of double mixing, in which both the B^0 and $\bar{B}^0$ oscillate. The $\Upsilon(4S)$ is a $J^{PC} = 1^{--}$ state, with an antisymmetric wave function. Oscillation of one of the B mesons would produce a pair of identical particles in the same quantum state, in violation of the Pauli exclusion principle. For this reason mixing of B^0 or $\bar{B}^0$ can not occur until the accompanying $\bar{B}^0$ or B^0 has already decayed.

The charge correlations in unlike- and like-sign dileptons from $B\overline{B}$ events are summarized in the following equations:

$$\frac{dN(\ell^{\pm}e^{\mp})}{dp} = N_{\ell}\eta(p)\left[\frac{d\mathcal{B}(b)}{dp}(1-\chi) + \frac{d\mathcal{B}(c)}{dp}\chi + \left(\frac{d\mathcal{B}(c)}{dp}\right)_{same\,B}\right], \quad (4.1)$$

$$\frac{dN(\ell^{\pm}e^{\pm})}{dp} = N_{\ell}\eta(p)\left[\frac{d\mathcal{B}(b)}{dp}\chi + \frac{d\mathcal{B}(c)}{dp}(1-\chi)\right]. \quad (4.2)$$

In these equations $\mathcal{B}(b) = \mathcal{B}(b \to x\ell\nu)$; $\mathcal{B}(c) = \mathcal{B}(b \to c \to y\ell\nu)$; N_ℓ is the number of tag leptons; $\eta(p)$ is the momentum dependent efficiency to find the second electron; and $\chi = f_0\chi_0$. The third term in Eq. 4.1 is for primary-secondary combinations from the same side of an event.

In order to study the semileptonic decay spectrum over nearly the full momentum range, we use only electrons as the second lepton. For the tag lepton, both high momentum electrons and muons are used to maximize statistics. The contributions to like- and unlike-sign spectra from a sample of generic $B\overline{B}$ Monte Carlo events are plotted in Fig. 4.3. The like-sign spectrum is dominated by secondary electrons. The

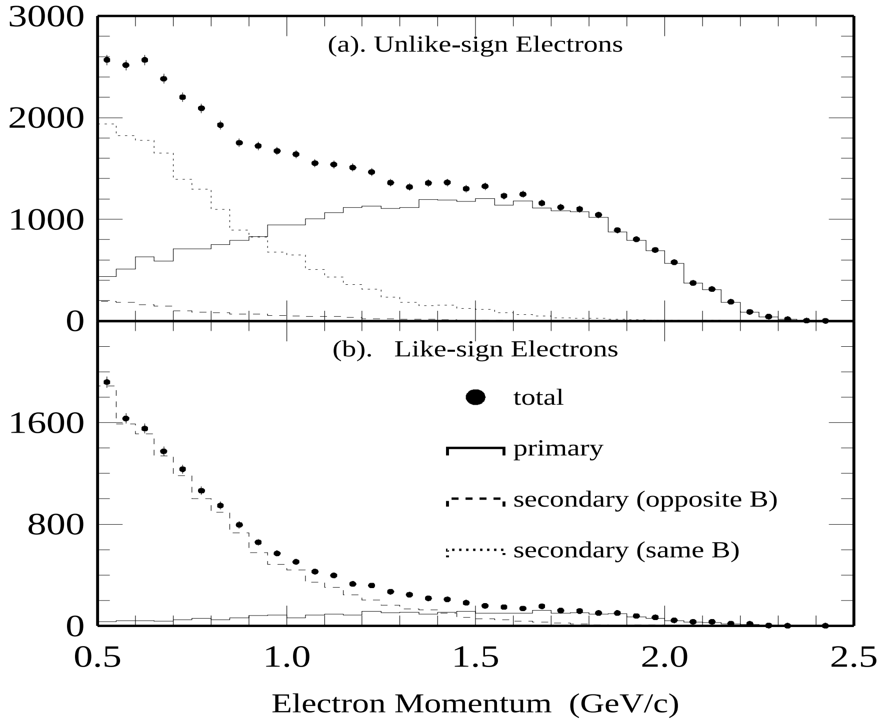

Figure 4.3: Unlike-sign (a) and like-sign (b) electron spectrum for events with high-momentum lepton tags selected from a sample of generic $B\overline{B}$ Monte Carlo events. Both the total spectrum (points) and the separate constituents are shown. The tag leptons were required to have momenta above 1.4 GeV/c, and to be identified in the good barrel regions of the electron and muon acceptance. The electrons which contribute to this plot were also identified in the good barrel region of the calorimeter. Note that there is no like-sign contribution from the same side.

unlike-sign spectrum would be dominated by primaries without the contribution from the same B. In principle the separate spectra for primary and secondary electrons could be obtained from the two equations, but the large contribution from the same B would introduce sizable uncertainties. If we can somehow suppress this term, then the primary electron spectrum obtained would be less dependent on the uncertainties associated with the secondary decays. This is studied in the next section.

4.2.2 Kinematic Correlations in Dilepton Events

Because the B mesons produced at the $\Upsilon(4S)$ are almost at rest, the daughters of different B's are almost completely uncorrelated in direction. Particles produced in the decay of the same B, on the other hand, tend to be produced back-to-back, as is shown in Fig. 4.4. The ARGUS analysis [38] took advantage of this correlation by

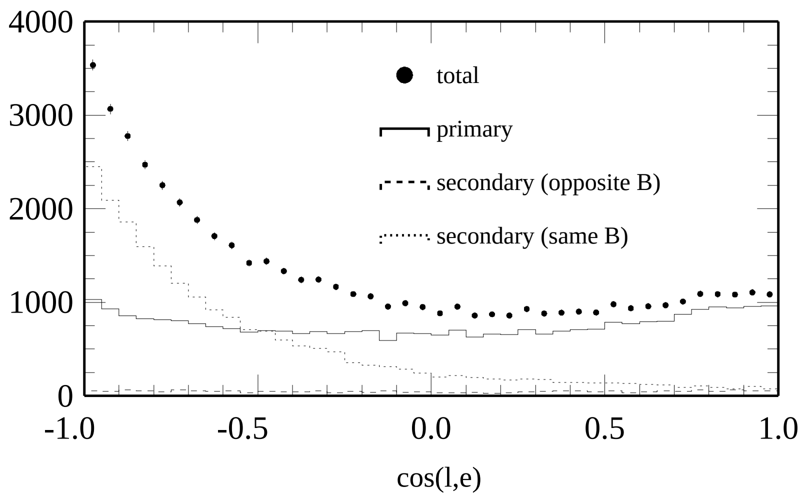

Figure 4.4: The distribution of the opening angle between the tag lepton and an additional unlike-sign electron in each event. Shown in this plot are electrons with momenta less than 1.0 GeV/c from primary decays, and both opposite- and same-side secondary decays. For electrons at higher momenta, the distributions are similar.

requiring unlike-sign electrons to be from the same hemisphere. For electrons above 0.6 GeV/c, this eliminated about 50% of the unlike-sign electrons from the opposite B, while suppressing the same B contribution by a factor of 15 .

We have improved on this procedure by exploring cuts in the two dimensional plane of the electron momentum (p_e) and the cosine of the opening angle between the electron and the tag, ($\cos(\ell, p_e)$). The signal considered is unlike-sign opposite-side electrons, which has an essentially flat distribution in $cos(\ell, e)$ (Fig. 4.5a). The background, electrons from the same B, exhibits a triangular distribution, with the concentration of entries at lower momenta and in opposite hemispheres (Fig. 4.5b). This distribution suggests that diagonal cuts in this plane should be investigated.

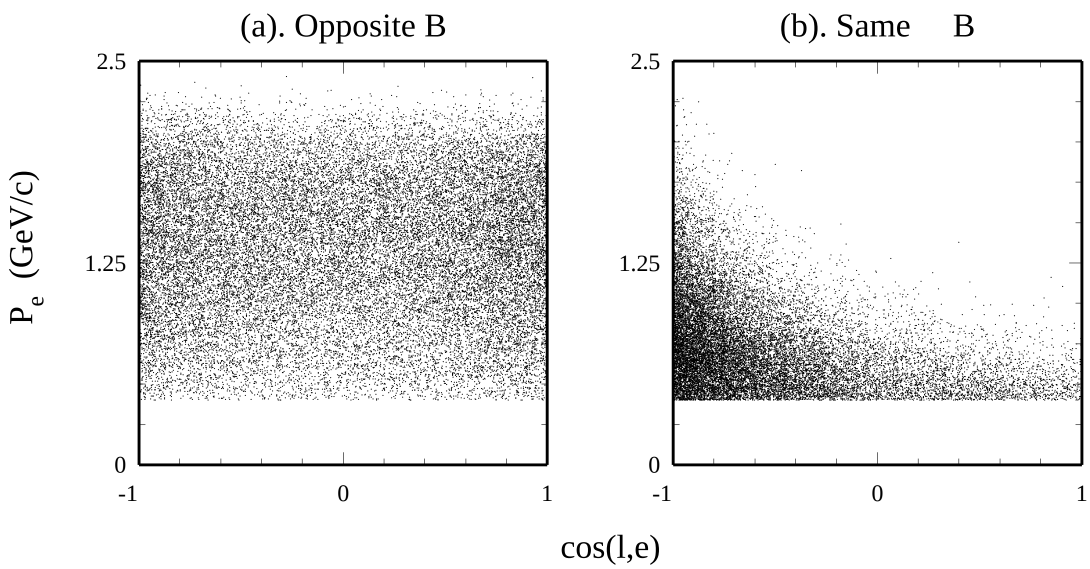

Figure 4.5: The two dimensional distributions of unlike-sign electrons. Shown in (a) are electrons from the opposite side to the tag lepton, and in (b) those from the same side.

The projection of these two dimensional distributions onto electron momentum, without any cuts, is shown in Fig. 4.3a. After a particular cut has been applied in the $(p_e, cos(\ell, e))$ plane, a second set of projections is obtained. The ratio of the two projections gives the efficiency of that cut. Two cases must be considered. For dileptons produced by different B's (either primary-primary or primary-secondary), we label the efficiency $\epsilon(p)$. For dileptons from the same B, we label the efficiency $\delta(p)$. With a cut applied, the unlike-sign spectrum originally given in Eq.(4.1) becomes

$$\frac{dN(\ell^{\pm}e^{\mp})}{dp}_{(cut)} = N_\ell \eta(p)\left[\epsilon(p)\left(\frac{d\mathcal{B}(b)}{dp}(1-\chi)+\frac{d\mathcal{B}(c)}{dp}\chi\right)+\delta(p)\left(\frac{d\mathcal{B}(c)}{dp}_{(same\,B)}\right)\right] \qquad (4.3)$$

The objective for cut design is good suppression of the same B contribution with acceptable $\epsilon(p)$ for the signal. We discuss three possible cuts for comparison. The first is the hemisphere cut, $cos(\ell^{\pm}, e^{\mp}) > 0$, used by ARGUS for their model-independent analysis [38]; the second is a diagonal cut, $p_e + cos(\ell^{\pm}, e^{\mp}) > 1$; and the third is a combination of the two, $(cos(\ell^{\pm}, e^{\mp}) > 0)$ or $(p_e + cos(\ell^{\pm}, e^{\mp}) > 1)$. In Fig. 4.6 we plot the signal spectrum of unlike-sign opposite-side electrons. In Fig. 4.7 we plot the

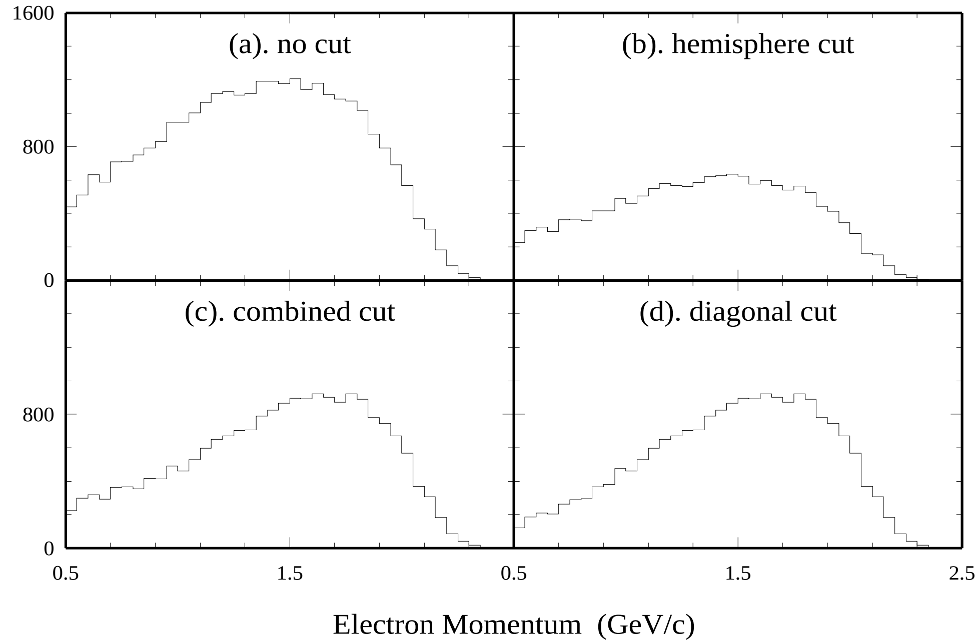

Figure 4.6: Spectrum of unlike-sign opposite-side electrons with (a) no cut, (b) the hemisphere cut, (d) the diagonal cut, and (c) the combined cut.

background spectrum of unlike-sign same-side electrons. By comparing the plots for each cut to those with no cut, we obtain $\epsilon(p)$ and $\delta(p)$. By integrating these functions of p_e from $\min\{p_e\}$(0.6 GeV/c) to $\max\{p_e\}$(2.6 GeV/c) we get the overall efficiencies $\mathcal{E}$ and Δ of signal and background for each cut, which are listed in Table 4.2. The triangular distribution in the $(cos(l,e), p_e)$ plane for electrons from the same B suggests stronger suppression at lower momenta but weaker at higher momenta. Obviously a simple opening angle cut loses an unnecessarily large amount of signal at high momentum. Because of the rapid decrease of the same-side contribution as momentum increases from 1 GeV/c to 2 GeV/c, this cut can be loosened. In this region, the diagonal cut achieves the same suppression of background, but saves about 50% more signal. Below 1 GeV/c it loses slightly more signal, while cutting the background harder. Even in the lowest bin we have 25-30% of the signal left, as is demonstrated by the functions $\epsilon(p)$ and $\delta(p)$ in Fig. 4.8. The combined cut is essentially the diagonal cut above 1 GeV/c,

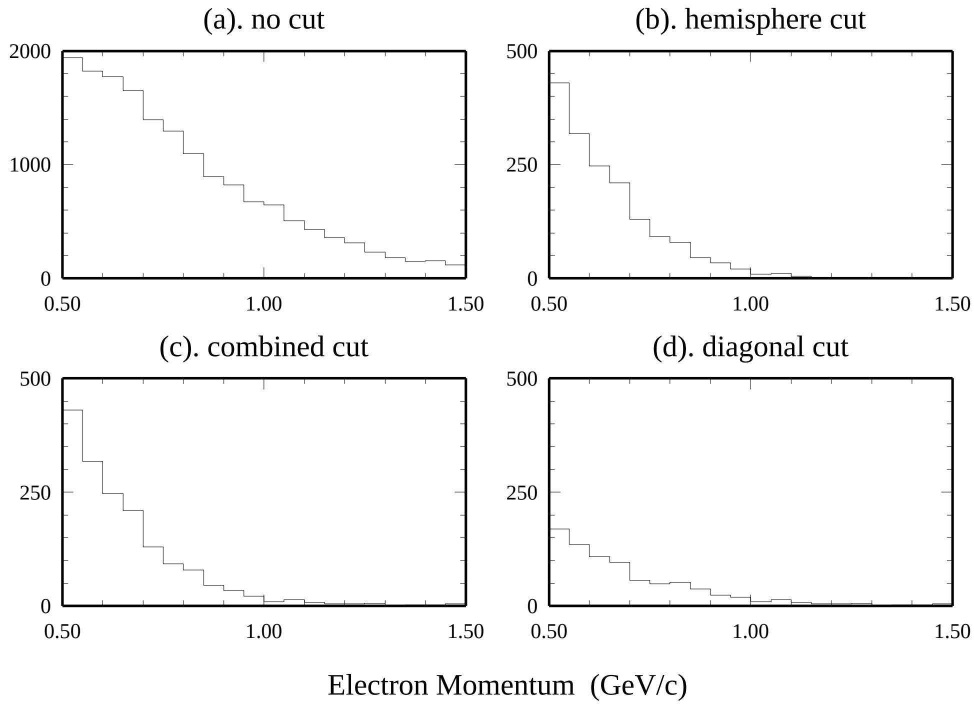

Figure 4.7: Spectrum of unlike-sign same-side electrons with (a) no cut, (b) the hemisphere cut, (d) the diagonal cut, and (c) the combined cut.

and the opening angle cut below that. Based on the efficiencies in Fig. 4.8 and Table 4.2, we choose the diagonal cut in this analysis.

4.2.3 Systematic Errors of Diagonal Cut

The efficiencies $\epsilon(p)$ and $\delta(p)$ which appear in Eq.(4.3) represent the response to our cuts of leptons from several distinct sources. It is necessary to assess the dependence of the diagonal cut efficiency on reasonable variations in these sources, in both signal and background.

Primary lepton production, as modeled in our $B\overline{B}$ Monte Carlo, includes four decay channels: $B \to D\ell\nu$, $B \to D^*\ell\nu$, $B \to D^{**}\ell\nu$ and $B \to D(D^*)(n)\pi l\nu$. The first three use the ISGW model [15], which describes the lepton spectra very well. The fourth, nonresonant, is treated as V-A at the quark level, with phase space used to generate

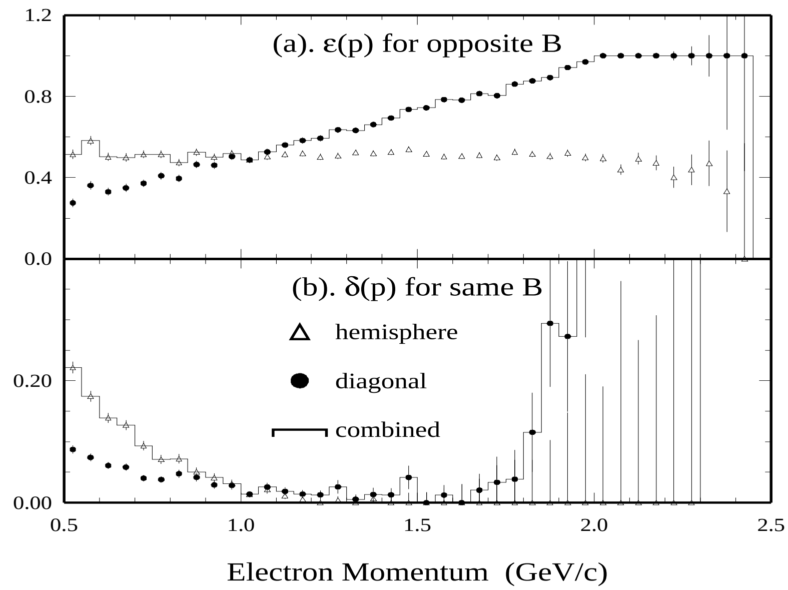

Figure 4.8: Efficiency of cuts as a function of momentum for unlike-sign electrons. The diagonal cut, which is used in this analysis, is shown as the circles. The efficiency for unlike-sign opposite-side electrons (a) is $\epsilon(p)$. That for unlike-sign same-side electrons (b) is $\delta(p)$.

the final-state mesons. The branching fractions for these four modes were taken to be 2.1%, 5.4%, 1.6% and 1.6% in the Monte Carlo. The first two branching ratios are consistent with exclusive measurements, but the decays into D^{**} and nonresonant final states are very uncertain. Variation of these fractions may affect the efficiency of the diagonal cut we use.

We have studied this by separating the generic $B\overline{B}$ Monte Carlo sample into subsamples corresponding to each of the individual channels. We observe that the efficiency $\epsilon(p)$ is the same for all modes, as is shown in Fig. 4.9. No significant deviation in $\epsilon(p)$ for any mode from the combined is present. The efficiency is therefore independent of the fraction of D^{**}, and of the details of the nonresonant final states studied. The efficiency for secondary leptons from the opposite B also agrees with $\epsilon(p)$. From our observation of no significant variation of this efficiency within our Monte Carlo statistics, we conclude that the systematic uncertainty in $\epsilon(p)$ is neligible.

Table 4.2: Integrated Efficiencies of Cuts

effic. and cut	hemisphere	combined	diagonal
$p_e > 0.5$ GeV/c			
$\mathcal{E}$	51%	68%	65%
Δ	10%	10%	5.0%
$\mathcal{E}/\Delta$	5.1	6.8	13.0
$p_e > 0.6$ GeV/c			
$\mathcal{E}$	51%	69%	67%
Δ	7.0%	7.0%	4.0%
$\mathcal{E}/\Delta$	7.5	9.3	16.7

The suppression of the same-side component by the diagonal cut must also be considered, since it is necessary to correct for electrons from this source which leak through the cut and contribute to the measured spectrum. We divide the electrons from the same B into four components, according to which of the channels produced the tag lepton. Because it has both the largest branching fraction and the stiffest lepton spectrum, the mode $B \to D^*\ell\nu$ dominates. This is evident in Fig. 4.10. Table 4.3 lists the contributions mode by mode, in the momentum region 0.5 to 2.6 GeV/c, for a particular Monte Carlo sample. Of the four types of semileptonic decays, $B \to D^*\ell\nu$ has

Table 4.3: Unlike-sign electrons from same B

charm state	no cut	diagonal cut
D	4574 ± 68	147 ± 12
D^*	10103 ± 101	676 ± 26
D^{**}	1592 ± 40	53 ± 7
non-resonance	615 ± 25	39 ± 6
total	16884 ± 130	915 ± 30

been the most intensely studied, and has the best measured branching fraction with an error less than 10%. This insures that the uncertainties in the residues of the cut are well understood, since variations in the other three contribute very little. We are particularly insensitive to changes in the fraction of D^{**} and nonresonant modes for two

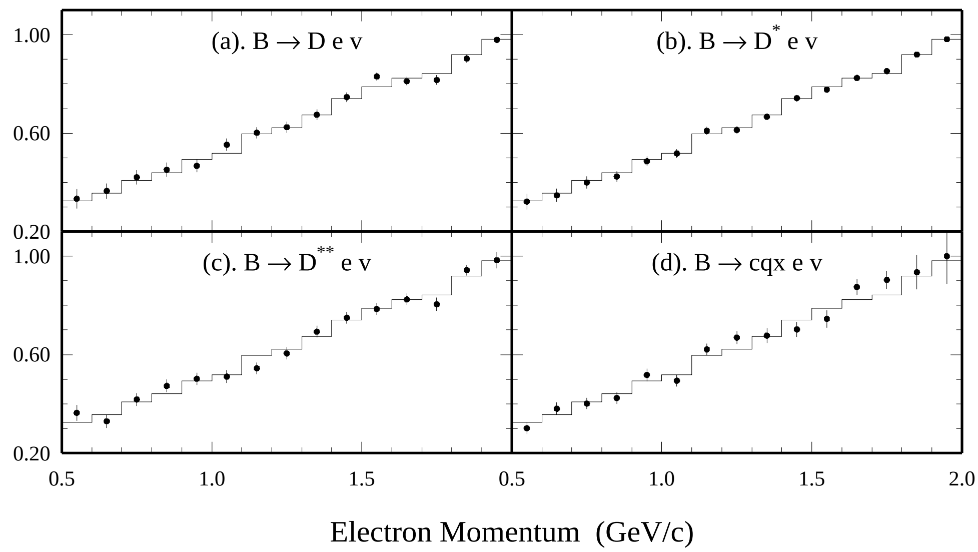

Figure 4.9: Diagonal cut efficiency $\epsilon(p)$ for opposite-side electrons. The histogram is the efficiency for all channels combined, and the dots represent the efficiencies for the individual modes. Nonresonant production is denoted by cqx. The efficiency for the small fraction of secondary electrons from the opposite side also agrees with the histogram.

reasons. Since these decays produce softer primary leptons, potential tags are detected with lower efficiency. Furthermore, when these decays occur several π's carry significant energy away, leaving less for the secondary electron, and increasing the likelihood of failing the diagonal cut in the $(p_e, cos(l,e))$ plane. Taking into account all of these uncertainties, we estimate that the overall uncertainty in the contribution of the same B after the diagonal cut is less than 15%.

To conclude this section, the charge and kinematic correlations are expressed in Eqs. 4.2 and 4.3. In principle, we should be able to obtain the spectrum of primary electrons and that of secondary electrons by solving these two equations, when the third term in Eq. (4.3) is not present. With the diagonal cut, and our thorough understanding of the residual same-B contribution, we are ready to apply our techniques to data.

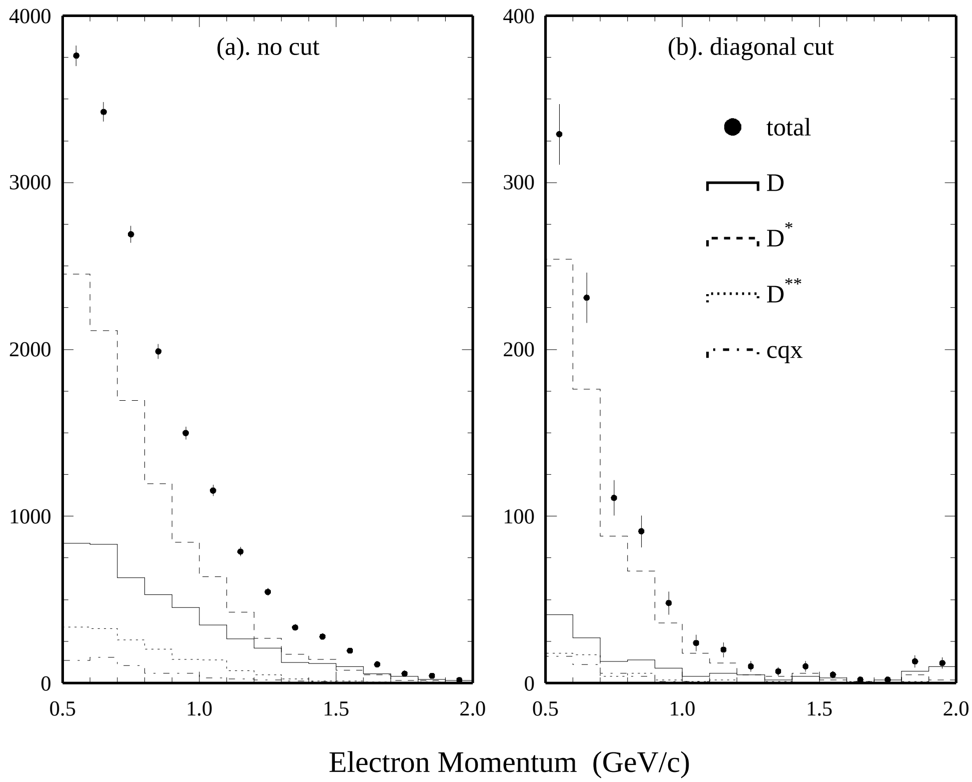

Figure 4.10: Same-side electrons divided into individual B semileptonic decay channels that give rise to the tag lepton. The dots are the totals, and the histograms are the charm states which accompany the tag lepton. The distributions before application of the diagonal cut are shown in (a), and those after the cut is applied are shown in (b). Contributions from D^{**} and non-resonant modes (marked as cqx) are very small. Their numerical values are listed in Table 4.3.

4.3 Data Yields and Background Corrections

The results we report with this chapter used the same data samples, event and lepton selection criteria, as the inclusive lepton spectrum analysis (Chapter 3 and ref. [28]). We briefly reintroduce them and discuss corrections for fake leptons and other backgrounds in this section.

4.3.1 Data Sample and Dilepton Selection

The data sample for this analysis consists of 2,057 pb^{-1} collected at the Υ(4S) resonance (ON), and 958 pb^{-1} taken at center-of-mass energies approximately 60 MeV below the resonance (OFF). The ON data include $2,202,000 \pm 11,000$ Υ(4S) decay events. The study of efficiencies and backgrounds used about 5 million generic $\Upsilon(4S) \rightarrow B\overline{B}$ Monte Carlo events.

The OFF spectra are used to estimate the shape and amount of the contribution from continuum processes to the ON spectra. No continuum-suppression cuts have been employed in this study. The scale factor for the continuum subtraction $\alpha_{\mathcal{L}}(4S) = 2.124 \pm 0.011$ is given by Eq. 3.1.

Lepton candidates are selected with the same criteria as described in Section 3.2. Mainly, we use lepton candidates for signal and loosely identified leptons for background rejection. In this analysis, a tag lepton is defined as either a muon or an electron candidate with a measured momentum greater than 1.4 GeV/c. For every event with a tag lepton, we search for an additional well identified electron candidate. These are then classified as unlike-sign or like-sign with respect to the tag. For unlike-sign electrons the diagonal cut $p_e + cos(\ell, e) > 1$ is applied to suppress those which were produced in the decay of the same B as the tag.

Using the above selection criteria we obtain the raw spectra of unlike- and like-sign electrons, both from the ON and the OFF data (Figs. 4.11 and 4.12). In the case of the OFF, we scale the electron momenta by the ratio of beam energies, and subtract (ON) − $\alpha_{\mathcal{L}}$(4S)(OFF) to obtain the net contribution from the Υ(4S). The integrated yields are summarized in Table 4.4. These raw spectra include not only the electrons we wish to measure, but also misidentified electrons and electrons from background sources. Correction for these contributions is the next step.

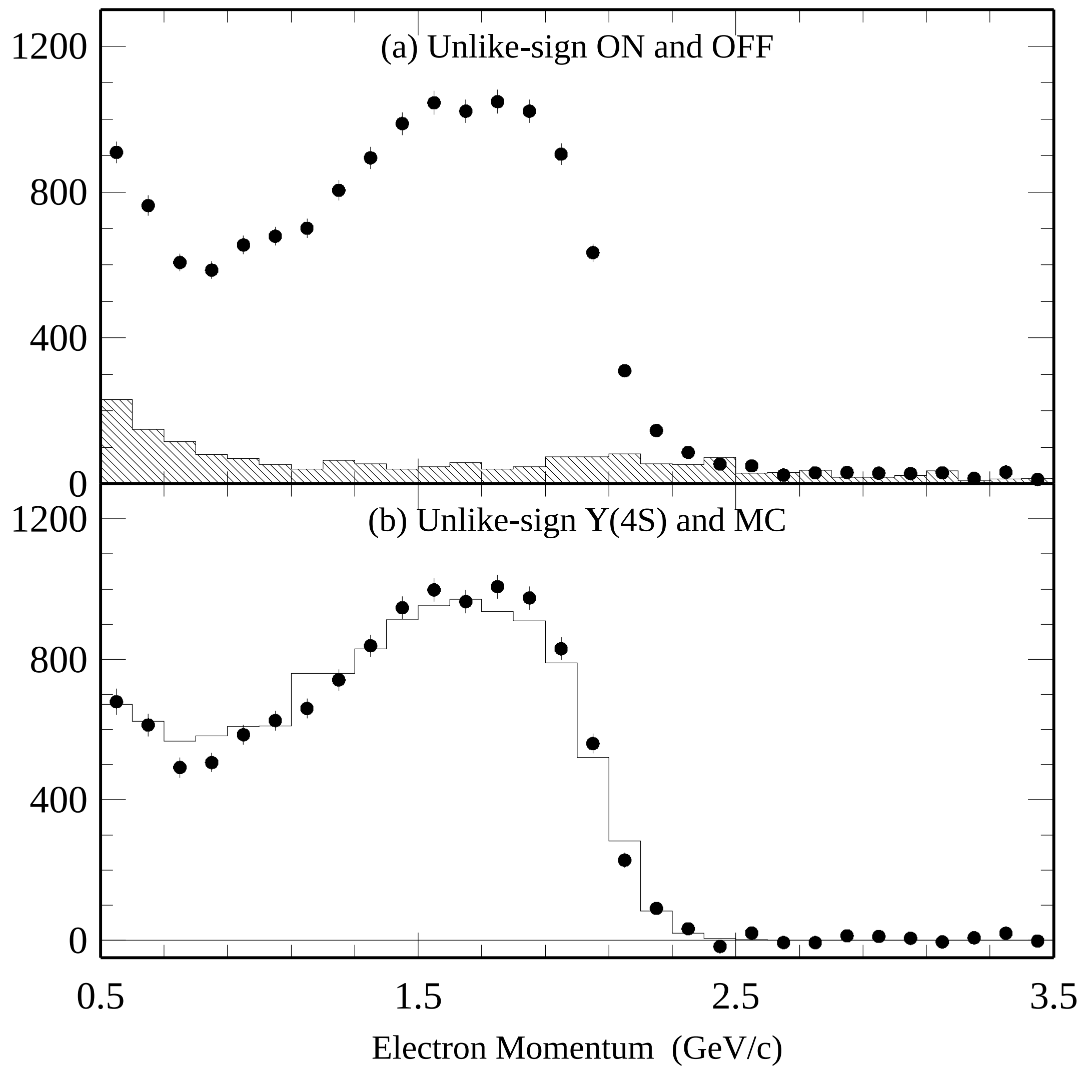

Figure 4.11: Raw Spectra of unlike-sign electrons with the diagonal cut applied. In (a), the dots are from the ON data and the shaded area is the luminosity-scaled OFF data. In (b), the dots are the net $\Upsilon(4S)$, and the histogram is $B\bar{B}$ Monte Carlo.

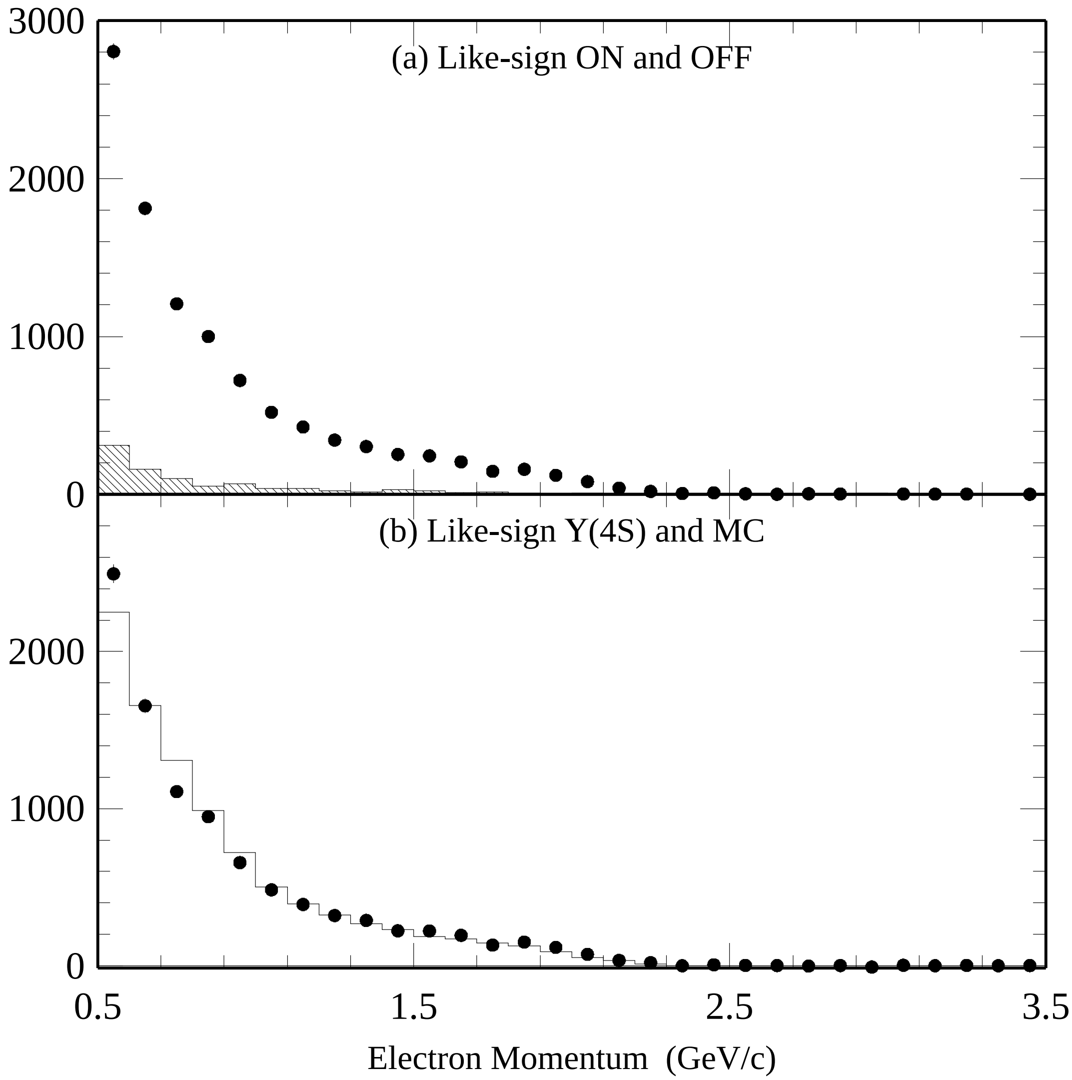

Figure 4.12: Raw spectra of like-sign electrons. In (a), the dots are from the ON data and the shaded area is the luminosity-scaled OFF data. In (b), the dots are the net $\Upsilon(4S)$, and the histogram is $B\bar{B}$ Monte Carlo.

Table 4.4: Raw Electron Yields from Data

0.6-2.6 GeV/c	ON	scaled OFF	$\Upsilon(4S)$
Unlike Sign	$13,115 \pm 115$	$1,365 \pm 54$	$11,749 \pm 127$
Like Sign	$7,699 \pm 88$	637 ± 37	$7,062 \pm 95$

4.3.2 Fake and Background Corrections

In this analysis we are interested in electrons from semileptonic decays of B and D mesons in events where the other B decayed to a high momentum tag lepton. In addition to these electrons, the raw spectra include the following backgrounds:

1. Hadrons misidentified as either the measured electron or the tag;
2. Electrons or tag leptons from pair-type processes in $\Upsilon(4S)$ decays
   - $J/\psi(\psi') \to \mu^+\mu^-$ or $J/\psi(\psi') \to e^+e^-$,
   - $\pi^0(\eta) \to e^+e^-\gamma$,
   - γ conversion to e^+e^- pairs in the detector;
3. Electrons or tag leptons from τ's produced in B decays;
4. Electrons or tag leptons from $D_s^\pm$ or $\Lambda_c^\pm$ produced in B decays;
5. Tags which are secondary leptons;
6. Same-side unlike-sign electrons which leak through the diagonal cut.

These backgrounds have been studied by using data and Monte Carlo, and are tabulated in Table 4.5.

The misidentification probability has been studied with enriched samples of pions, kaons and protons selected in $\Upsilon(4S)$ data [28]. The overall fake contribution to the observed yields is then computed by using hadron spectra obtained from $\Upsilon(4S)$ data, as was described in Chapter 3.

Table 4.5: Backgound Corrections. The errors are statistical, systematic.

0.6-2.6 GeV/c Source	Unlike Sign $p_e + cos(\ell, e) > 1$	Like Sign no cut
ON Υ(4S)	$13,115 \pm 115$	$7,699 \pm 88$
Continuum	$1,365 \pm 54 \pm 7$	$637 \pm 37 \pm 3$
Fake tag ℓ	$141 \pm 2 \pm 71$	$85 \pm 1 \pm 43$
Fake e	$214 \pm 3 \pm 107$	$540 \pm 8 \pm 270$
Unvetoed tag ℓ or e from J/ψ	$161 \pm 4 \pm 32$	$135 \pm 3 \pm 27$
Unvetoed tag ℓ or e from π^0	$45 \pm 4 \pm 9$	$131 \pm 8 \pm 27$
Unvetoed tag ℓ or e from γ	$56 \pm 5 \pm 11$	$152 \pm 8 \pm 30$
Tag ℓ or e from τ	$270 \pm 11 \pm 54$	$70 \pm 5 \pm 14$
Tag ℓ or e from Λ_c	$16 \pm 2 \pm 5$	$99 \pm 6 \pm 30$
Tag ℓ or e from D_s	$291 \pm 13 \pm 87$	$84 \pm 6 \pm 25$
Tag ℓ or e from ψ'	$77 \pm 4 \pm 19$	$19 \pm 2 \pm 5$
Tag ℓ or e from η	$7 \pm 3 \pm 2$	$27 \pm 5 \pm 7$
Tag ℓ from D	$205 \pm 10 \pm 51$	$401 \pm 13 \pm 100$
e from same B	$329 \pm 13 \pm 49$	–
Total Background	$3,177 \pm 60 \pm 183$	$2,380 \pm 43 \pm 298$
Background subtracted	$9,940 \pm 129 \pm 183$	$5,321 \pm 98 \pm 298$

Real leptons from J/ψ and π^0 Dalitz decays, and from photon conversions are rejected from data by using kinematic characteristics of these processes. These procedures are essentially identical to the methods used in the inclusive analysis (Chapter 3). Most of the leptons from $B \to XJ/\psi, J/\psi \to \ell^+\ell^-$ decays, for example, are rejected by using the invariant mass of the lepton pair. For each tag lepton or electron, we pair it with a loosely identified lepton of the same flavor, but opposite charge, to calculate the invariant mass. The distribution of this dilepton mass for our Υ(4S) data sample is shown in Fig. 4.13a. The mass peak can be fitted with a bifurcated Gaussian. If the invariant mass is within 3σ of the J/ψ mass, the event is vetoed. This veto is only about 60% efficient, so we correct by using the efficiency determined with Monte Carlo. A similar procedure is used to veto electrons from π^0 Dalitz decays. The three-body $e^+e^-\gamma$ invariant mass distribution is shown in Fig. 4.13b. Electrons from photon conversions in the beam pipe and chamber walls are rejected by using the geometry of the

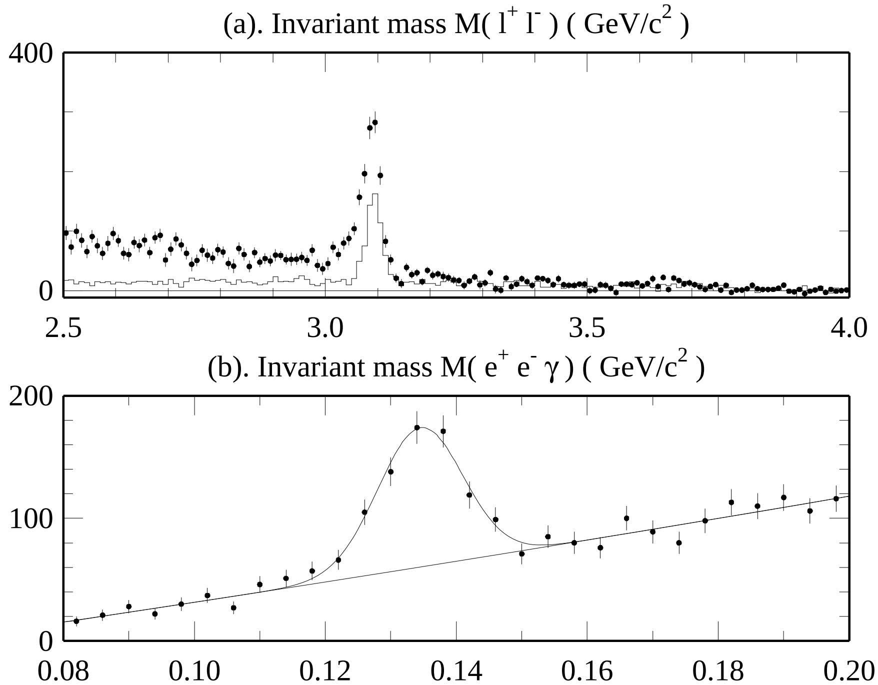

Figure 4.13: (a) The invariant mass of $\ell^+\ell^-$ candidates in our Υ(4S) data sample. The dots give the e^+e^- distribution, and the histogram is that for $\mu^+\mu^-$. (b) The invariant mass of $e^+e^-\gamma$ candidates, where the dots are data, the curve is the fitted Gaussian, the fitted background is also shown.

pairs [30, 28]. Again, we correct for leakage with the aid of Monte Carlo. The estimated systematic error for each of these three corrections is below 20%. Background leptons from ψ' and η Dalitz decays are subtracted by using Monte Carlo.

The next correction is for B semileptonic decays through τ which can contribute to our yields through the τ leptonic decay modes. We estimate these with Monte Carlo samples scaled to the integrated luminosity of our Υ(4S) sample. Leptons from these decays are quite soft, so that they mostly contribute only to the electron yields, and not to the tag leptons. We estimate the uncertainty to be less than 20%.

In the lepton tagged B events, leptons from D_s decays have different charge and kinematic correlations than those from $D^\pm$ and D^0, due to D_s mesons produced from $b \to cW^-$ and $W^- \to \bar{c}s$ decays. This is evident in Table 4.5. To corrected for leptons from charmed baryons, the model for B to charmed baryon decays described in

Chapter 3 is used, since we use the same Monte Carlo sample. In this model, 80% of B to charmed baryon decays go through $B \rightarrow \Lambda_c \bar{p}(\bar{n}) n\pi$ and 20% go through charmed baryon pair production. This model is consistent with the measured Λ_c spectrum and charmed baryon production rates in B events.

Secondary leptons from $B \rightarrow XD$, $D \rightarrow Yl\nu$ can occasionally be above 1.4 GeV/c, and contribute false tags. About 2.8% of all identified leptons above this momentum are secondaries. We correct for this by using luminosity-scaled Monte Carlo data, again with an estimated 25% uncertainty. The last correction is for electrons from the same B as produced the tag lepton, as described in Section 4.2. As we discussed there, the uncertainty is estimated to be less than 15%.

After all the corrections, we are left with $9,940 \pm 129 \pm 180$ unlike-sign electrons in the momentum region $0.6 - 2.6$ GeV/c, and $5,321 \pm 98 \pm 298$ like-sign. Their spectra before and after the corrections are shown in Fig. 4.14.

4.4 Spectra and Branching Fractions

After the above corrections for backgrounds, the spectra of like- and unlike-sign electrons described by Eqs. (4.2) and (4.3) are now simplified to the following:

$$\frac{dN(\ell^{\pm}e^{\mp})}{dp}_{(cut)} = N_{\ell}\eta(p)\left[\frac{d\mathcal{B}(b)}{dp}(1-\chi) + \frac{d\mathcal{B}(c)}{dp}\chi\right]\epsilon(p) \tag{4.4}$$

$$\frac{dN(\ell^{\pm}e^{\pm})}{dp} = N_{\ell}\eta(p)\left[\frac{d\mathcal{B}(b)}{dp}\chi + \frac{d\mathcal{B}(c)}{dp}(1-\chi)\right] \tag{4.5}$$

The two spectra $d\mathcal{B}(b \rightarrow x\ell\nu)/dp$ and $d\mathcal{B}(b \rightarrow c \rightarrow y\ell\nu)/dp$ can be obtained bin-by-bin by solving these two equations. In this section, we follow the steps that lead to the resulting spectra and branching fractions.

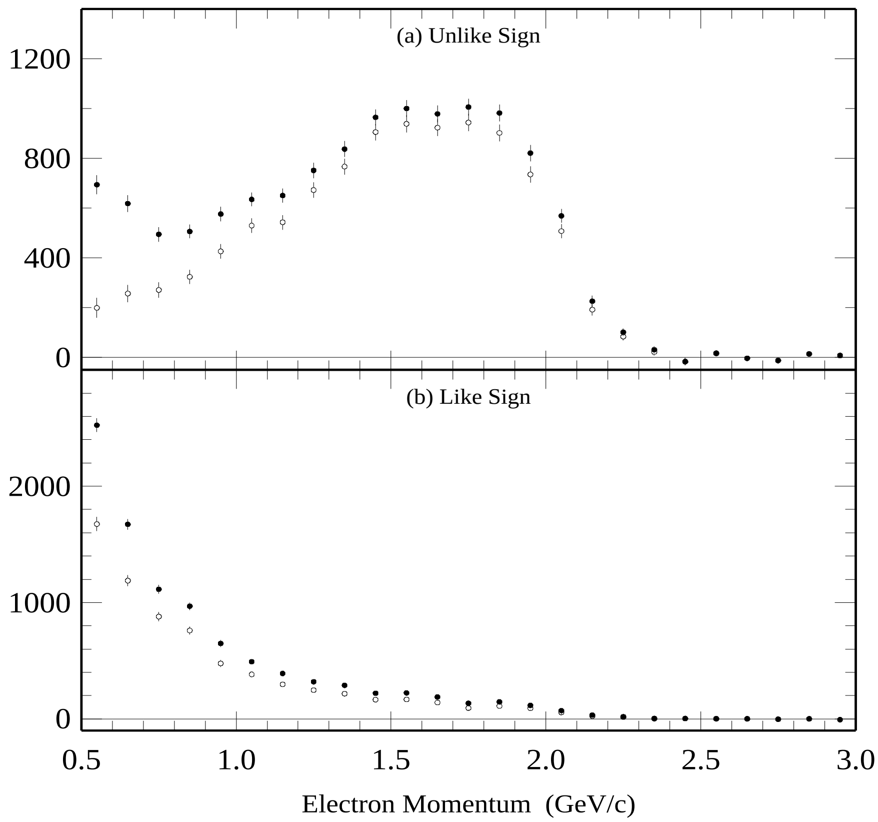

Figure 4.14: Momentum spectra of electrons in lepton-tagged $\Upsilon(4S)$ events. The dots are the raw yields, and the open circles are the yields after all background subtractions.

4.4.1 $B\bar{B}$ Mixing Parameter χ

The $B\bar{B}$ mixing parameter $\chi = f_0\chi_0$ in Eqs. (4.4) and (4.5) has been measured with different techniques both at the $\Upsilon(4S)$ and Z^0 energies. We choose the average of the latest ARGUS and CLEO results using dilepton samples [40]. We obtain $\chi_0 = 0.159 \pm 0.015 \pm 0.018$. Since our analysis uses $\chi = f_0 \times \chi_0$, it is immune to the systematic error associated with uncertainty of f_0. We therefore use $\chi = 0.080$ with a 15% error.

4.4.2 Number of Tag Leptons

Before solving Eqs. (4.4) and (4.5), we calculate the number of tag leptons N_ℓ from the background subtracted inclusive lepton spectra in Chapter 3. Above 1.4 GeV/c, these spectra contain a small fraction f_c of secondary leptons. f_c was determined to be about 2.8% with the $B^0\bar{B}^0$ in the mixing analysis [40]. We list the calculated number of tag leptons in Table 4.6. We have $251,752 \pm 755$ tag leptons, about 56% electrons and 44% muons.

Table 4.6: Number of High Momentum Tag Leptons

$p_\ell : 1.4 - 2.6$ GeV/c	e	μ	$e+\mu$
N_{tot}	$146,015 \pm 563$	$112,999 \pm 535$	
f_c	2.83%	2.77%	
$N_\ell = N_{tot}(1-f_c)$	$141,883 \pm 547$	$109,869 \pm 520$	$251,752 \pm 755$

We must also correct for possible differences in the efficiencies for selecting hadronic events with different numbers of leptons. Our hadronic event-selection criteria are `KLASGL`=10, and at least 5 charged tracks. The number of tag leptons calculated above is based on events with at least one lepton. For our signal sample we require hadronic events with a high momentum lepton tag and an additional electron. As the number of leptons (and neutrinos) in $B\overline{B}$ events increases, the total charged multiplicity tends to decrease, and the result is a slightly lower probability to pass the hadronic event selection. With our sample of 5 million generic $\Upsilon(4S) \to B\bar{B}$ events, which have been shown to agree well with data on particle multiplicity, we determine that the relative efficiency is $(97.9 \pm 0.5)\%$, with a very small lepton momentum dependence. The effective number of tag leptons is therefore $N_\ell = 246,465 \pm 739$ (statistical).

4.4.3 Results

With both the $B\bar{B}$ mixing parameter χ and the number of tag leptons N_ℓ, we solve Eqs. (4.4) and (4.5) to obtain the primary spectrum of electrons from B decays, $d\mathcal{B}(b \to x\ell\nu)/dp$, and also the secondary spectrum for electrons from charm decays, $d\mathcal{B}(b \to c \to y\ell\nu)/dp$. In solving the equations we use the efficiency of the diagonal cut $\epsilon(p)$ (Fig. 4.8), and the electron efficiency $\eta(p)$ (the product of tracking and electron identification efficiencies). The former is well modeled in the Monte Carlo, and the latter is measured with a data sample of radiative Bhabha tracks embedded in $\Upsilon(4S)$ hadronic events [25]. The separated primary and secondary spectra are shown in Fig. 4.15 (also tabulated in Appendix D after corrections for detector bremsstrahlung).

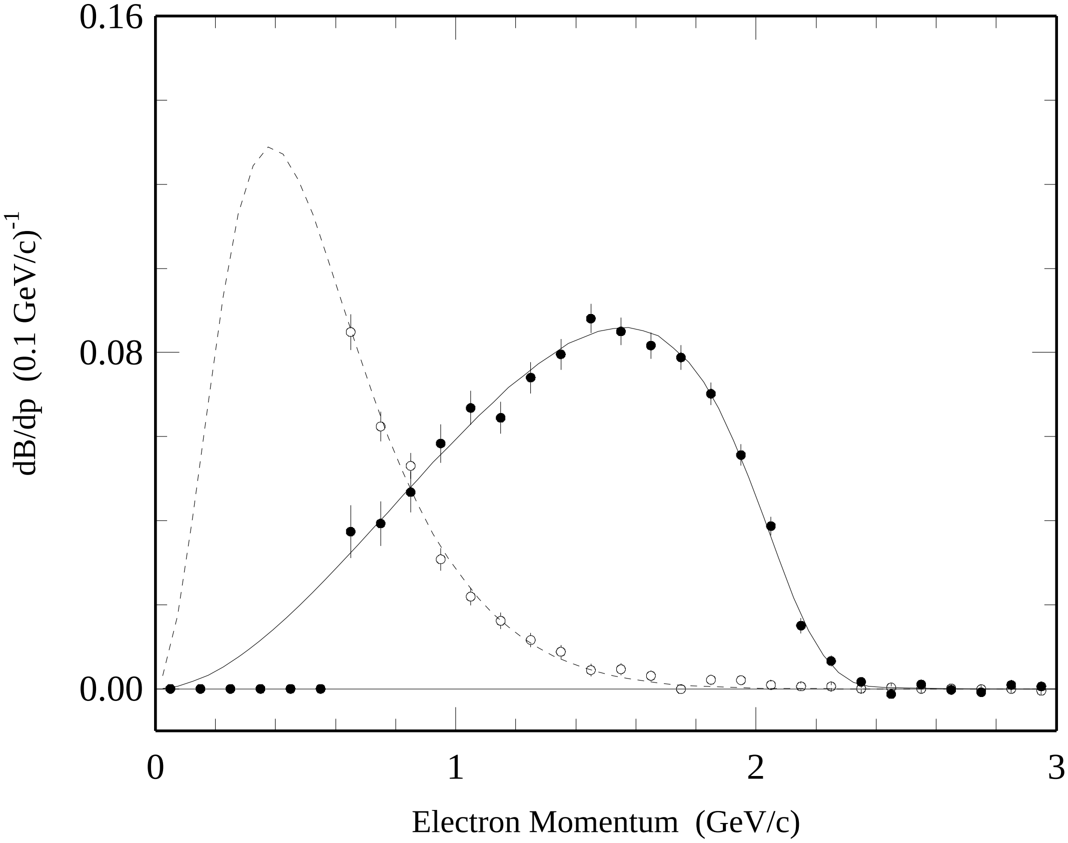

Figure 4.15: Spectrum of primary electrons, $d\mathcal{B}(b \to x\ell\nu)/dp$ (dots), and of secondary electrons, $d\mathcal{B}(b \to c \to y\ell\nu)/dp$ (open circles). The curves show the fits to the ISGW** model. Detector bremsstrahlung has been corrected for both the spectra and functions shown. The details of fits are discussed in the text.

The B-meson semileptonic branching fraction can now be obtained by integrating the primary electron spectrum. We integrate from 0.6 GeV/c to 2.6 GeV/c and obtain

$$\mathcal{B}(B \to Xe\nu; p > 0.6) = \int_{0.6}^{2.6} \frac{d\mathcal{B}(B \to Xe\nu)}{dp} dp = (9.85 \pm 0.16)\%. \qquad (4.6)$$

This is a model-independent result. Extracting the total semileptonic branching ratio requires us to extrapolate to momenta below 0.6 GeV/c. Theoretical models are needed for this extrapolation. Our procedure to generate the lepton spectrum for a given model was described in our previous analysis. Briefly, we generate the spectrum in the B-meson rest frame and apply electroweak radiative corrections. Then the spectrum is boosted into the laboratory frame, and smeared to simulate detector resolution and the effect of bremsstrahlung. The two models we use, ACCMM and ISGW, agree well in the fraction of the spectrum which lies above 0.6 GeV/c. Averaging the results for these two models, we find

$$\frac{\mathcal{B}(B \to Xe\nu; p < 0.6)}{\mathcal{B}(B \to Xe\nu)} = (5.8 \pm 0.5)\%, \tag{4.7}$$

where the systematic uncertainty given is just the difference between the models. With this help from theoretical models we obtain the semileptonic branching fraction of the B mesons,

$$\mathcal{B}(B \to Xe\nu) = (10.46 \pm 0.17)\%, \tag{4.8}$$

where the error is statistical only. The systematic error will be assessed in the next section. The model dependence is much smaller than in the inclusive analysis.

The models can be used, however, to fit the spectrum to obtain model-dependent branching ratios for comparison and consistency checks. The results of fits are listed in Table 4.7, together with the results of the inclusive spectra analysis. The errors are statistical only. The fraction of $b \to u\ell\nu$ has been constrained relative to $b \to c\ell\nu$ by using the results of $|V_{ub}/V_{cb}|$ obtained in Chapter 3. The $\chi^2/d.o.f.$ values of the fits to the primary spectrum are 21.7/22-1 for the ACCMM model, 42.1/22-1 and 16.5/22-2 for ISGW and ISGW** respectively. The details of fits are in Fig. 4.16. The fitted branching ratios in the tagged analysis are consistently somewhat smaller than those in the inclusive study. Possible explanations include statistical fluctuations and systematic effects which are not common between the two analyses. For the ACCMM model, parameters $p_F = 350\,\mathrm{MeV/c}$ and $m_c = 1,610\,\mathrm{MeV/c^2}$ are obtained by varying

Table 4.7: Comparison of Fits in Two Analyses

Model	Ratio (%)	This	Inclusive
None	$\mathcal{B}(b \to x\ell\nu)$	10.46 ± 0.17	–
ACCMM	$\mathcal{B}(b \to c\ell\nu)$	10.15 ± 0.16	10.43 ± 0.03
	$\mathcal{B}(b \to u\ell\nu)$	0.12	0.13
	$\mathcal{B}(b \to c \to y\ell\nu)$	7.77 ± 0.19	8.91 ± 0.18
	$\mathcal{B}(b \to x\ell\nu)$	10.27 ± 0.16	10.56 ± 0.03
ISGW	$\mathcal{B}(b \to c\ell\nu)$	9.86 ± 0.13	10.15 ± 0.03
	$\mathcal{B}(b \to u\ell\nu)$	0.09	0.10
	$\mathcal{B}(b \to c \to y\ell\nu)$	8.27 ± 0.21	10.25 ± 0.20
	$\mathcal{B}(b \to x\ell\nu)\%$	9.96 ± 0.13	10.25 ± 0.03
ISGW**	$\mathcal{B}(B \to D(D^*)\ell\nu)$	7.73 ± 0.23	8.38 ± 0.08
	$\mathcal{B}(B \to D^{**}\ell\nu)$	2.66 ± 0.30	2.45 ± 0.14
	$\mathcal{B}(b \to u\ell\nu)$	0.10	0.10
	$\mathcal{B}(b \to c \to y\ell\nu)$	8.27 ± 0.21	8.78 ± 0.24
	$\mathcal{B}(b \to c\ell\nu)$	10.39 ± 0.16	10.83 ± 0.07
	$\mathcal{B}(b \to x\ell\nu)$	10.49 ± 0.16	10.93 ± 0.07
	$\frac{\mathcal{B}(B \to D^{**}\ell\nu)}{\mathcal{B}(b \to c\ell\nu)}$	25.6 ± 2.6	22.6 ± 1.2

the two parameters in the plane $(p_F,\ m_c)$ with the same range and steps as in Chapter 3. The lepton spectrum in the ACCMM model is dependent on the sum $P_F + m_c$ as is shown in Figs. 3.12 and 3.13. This sum from the tagged analysis is consistent with that determined from fits to the inclusive spectra.

The secondary branching ratio $\mathcal{B}(b \to c \to ye\nu)$ is obtained by fitting the secondary electron spectrum with models. These model generated lepton spectral curves also include electroweak radiative corrections in the D rest frames, the boost to the laboratory frame, and detector smearing. The boost is performed by convoluting the measured inclusive $D^{\pm}$ and $D^0/\bar{D}^0$ momentum spectra from B decays and the electron spectrum in the D rest frame. For $14 - 1$ degrees of freedom, the ACCMM model gives a χ^2 of 18.1, and the ISGW model gives 18.2. The resulting secondary fits are shown in Fig. 4.17.

In this section, we successfully separated the primary electron spectrum from the

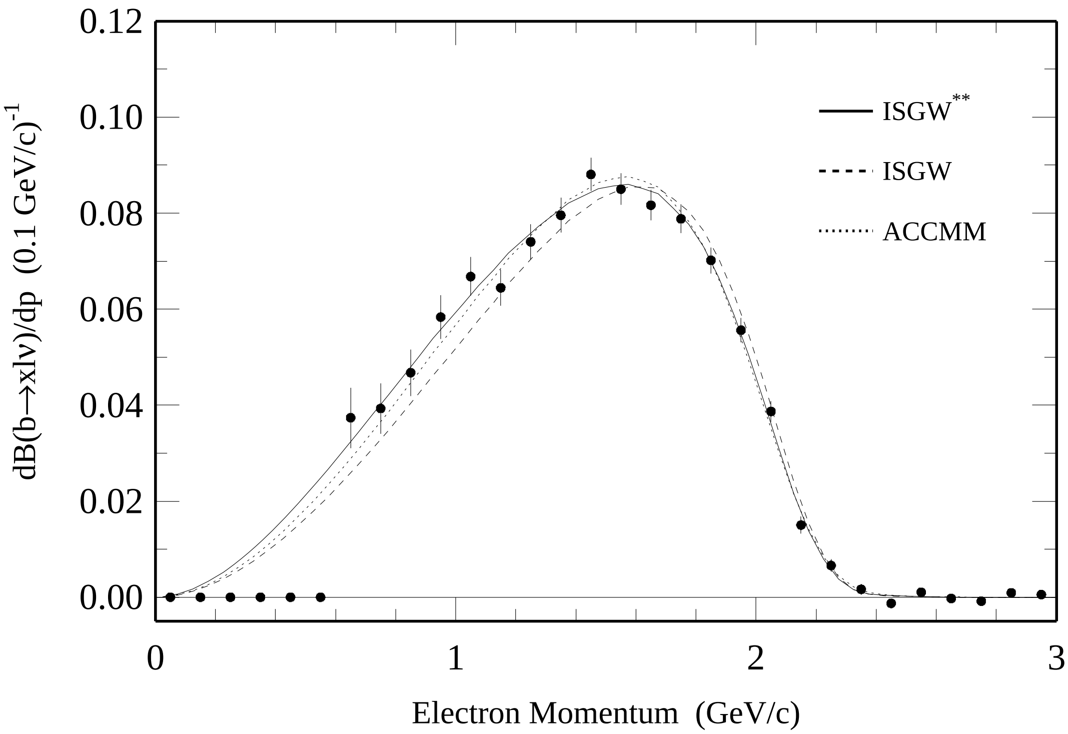

Figure 4.16: Fitting results of the primary electron spectrum $d\mathcal{B}(b \to x\ell\nu)/dp$ (dots) with three different models: ACCMM, ISGW, and ISGW**. The ISGW** model is identical to ISGW, except that the fraction of $B \to D^{**}\ell\nu$ is allowed to float.

secondary. We integrated the primary spectrum to obtain $\mathcal{B}(B \to Xe\nu) = (10.46 \pm 0.17)\%$, with minimum dependence on theoretical models. The secondary electron branching fraction is obtained by fitting with models. Both results are consistent with those of our inclusive lepton spectra analysis.

4.5 Systematic Errors

The major contributions to the systematic errors in the measured primary and secondary branching fractions are listed in Table 4.8. There are contributions from the background corrections, the $B\bar{B}$ mixing parameter, the electron identification efficiency, and the extrapolation from 0.6 GeV/c to zero momentum. The dominant ones are

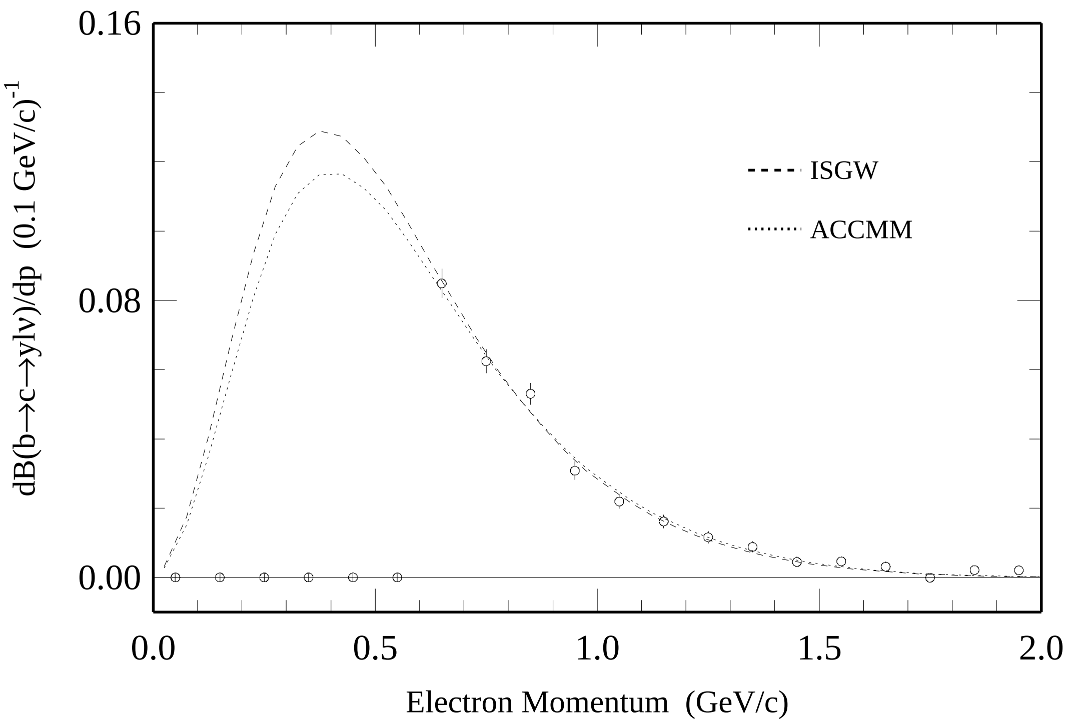

Figure 4.17: Fitting results of the secondary electron spectrum $d\mathcal{B}(b \to c \to y\ell\nu)/dp$ (open circles) with the ACCMM and the ISGW modesls.

the electron identification efficiency and the fake probability. The sum in quadrature is taken to be the combined systematic error. The theoretical uncertainty for $\mathcal{B}(b \to c \to ye\nu)$ is estimated to be 0.5% by taking the difference between the fits to the ACCMM and ISGW models.

The measured branching fraction $\mathcal{B}(B \to Xe\nu)$ in this analysis is the average of the semileptonic branching fractions of charged and neutral B mesons $\mathcal{B}(B) = f_+\mathcal{B}(B^+) + f_0\mathcal{B}(B^0)$. This average should be a very good representation for both type of B mesons, as the lifetimes of the charged and neutral B mesons are measured to be equal within 5-10% [41]. The differences between charged and neutral B decays could affect our result for the secondary electron branching fraction $\mathcal{B}(b \to c \to ye\nu)$, which is an average for the mixture of charmed particles produced in our B^+B^- and $B^0\bar{B}^0$ events. Questions would arise if the productions of D^+ and D^0 are drastically different in charged and

Table 4.8: Systematic Errors

Source X	$\frac{\delta X}{X}$ (%)	$\delta\mathcal{B}(b \to xe\nu)(\%)$	$\delta\mathcal{B}(b \to c \to ye\nu)(\%)$
ℓ fake	± 50	± 0.056	± 0.038
e fake	± 50	± 0.225	± 1.020
$J/\psi(\psi')$	± 30	± 0.043	± 0.042
$\pi^0(\eta)$	± 25	± 0.020	± 0.045
γ^0	± 20	± 0.016	± 0.034
τ	± 20	± 0.078	± 0.008
Λ_c	± 30	± 0.005	± 0.036
D_s	± 30	± 0.132	± 0.014
$\ell \leftarrow D$	± 25	± 0.052	± 0.130
same B	± 15	± 0.075	± 0.012
χ	± 15	± 0.100	± 0.087
f_c	± 25	± 0.074	± 0.056
$\epsilon_{\ell\ell}/\epsilon_\ell$	± 25	± 0.078	± 0.078
$\epsilon_{\ell ID}$	± 2	± 0.213	± 0.214
tracking	± 1	± 0.106	± 0.108
theory	± 10	± 0.062	± 0.500
total		± 0.428	± 1.200

neutral B decays. Whether our measurement is sensitive to this possibility has been tested by using a data sample with different fractions of charged and neutral B events. This sample consists of dilepton events with an additional soft pion that tags the decay of $B^0 \to D^{*+}l\nu, D^{*+} \to D^0\pi^+$. It includes about 75% $B^0\bar{B}^0$ and 25% B^+B^- events [41], very different from our standard $\Upsilon(4S)$ mix. We find good agreement between the primary electron branching ratio measurements made with the two different samples. To further assess the sensitivity of our analysis to the above question, we studied one million generator-level $B\bar{B}$ events using a generator which incorporates our current understanding of B decays. We show in Fig. 4.18 the secondary electrons from $B \to XD^0, D^0 \to Ye\nu$ and $B \to XD^+, D^+ \to Ye\nu$ for charged and neutral B mesons. Compared to the average of charged and neutral B mesons, B^- produces about 10% more D^0, and $\bar{B}^0$ produces about 20% more D^+. The production rates for D^0 in $B\bar{B}$ is about twice that for D^+, as is shown in Table 3.6. When averaged over D^0 and

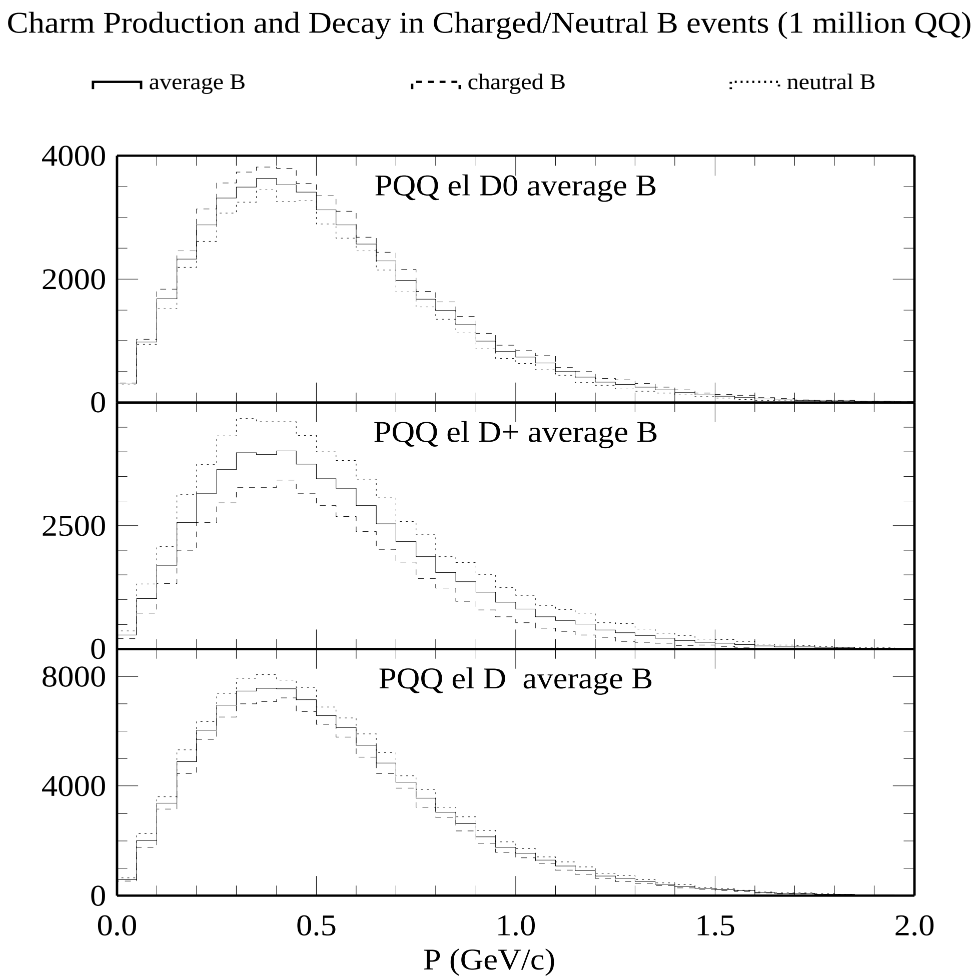

Figure 4.18: Secondary electron spectra from one million QQ generated $B\bar{B}$ events. Shown in (a) is electrons from $D^0\bar{D}^0$, (b) from $D^{\pm}$ and (c) for charged and neutral D combined. Comparisons are made in each case for $B^{\pm}$ and $B^0\bar{B}^0$ events.

D^+, the secondary lepton spectra of charged or neutral B differ from their average $\mathcal{B}(b \to c \to ye\nu)$ by less than 5%. We conclude that the difference in charm production from charged and neutral B events does not affect our measurement.

One important thing we check at this point is the value of f_c. We do the check by integrating the primary and secondary electron spectra in Fig. 4.15. The integral of secondary spectrum between 1.4 and 2.0 GeV/c is 0.0150 ± 0.0027, and the sum of primary and secondary between 1.4 and 2.6 GeV/c is 0.5119 ± 0.0083. We thus obtain our measured value $f_c = (2.93 \pm 0.57)\%$, which is consistent with the input value $f_c = (2.8 \pm 0.7)\%$ we used in this analysis.

4.6 CKM Matrix Element V_{cb}

The primary improvement in this lepton-tagged measurement compared to the inclusive analysis is reduced theoretical uncertainty. While the extrapolation to momenta below 0.6 GeV/c has some model dependence, this is small compared to the effect of model-to-model variations in the spectral shape used to fit the inclusive distribution. Recent progress with heavy quark expansion has considerably reduced the theoretical uncertainty in determining the CKM parameter $|V_{cb}|$ from the experimental measurements. In a recent paper[34], it was estimated to be 5% by using the experimental and theoretical constraints on the quark-mass difference $m_b - m_c$. Combining its prescription, the measured B-meson lifetime $\tau_B = (1.537 \pm 0.021)$ ps [52] and our measured B-semileptonic branching ratio in this analysis, we obtain $|V_{cb}| = 0.041 \pm 0.001 \pm 0.002$. Here the first error is the combined experimental error, including the errors in the branching ratio and B-lifetime measurements. The second error is theoretical.

4.7 Possible Non-$B\bar{B}$ Decays of the Υ(4S)

The second most significant improvement is the reduced dependence on the assumption that the Υ(4S) always decays to $B\bar{B}$. In the inclusive analysis, the lepton spectrum is normalized to the total number of Υ(4S) events. This correctly gives the B semileptonic branching fraction as long as there are no Υ(4S) decays to non-$B\bar{B}$ final states [42]. There is no substantial evidence for such decays, but the 90% confidence level upper limit for non-$B\bar{B}$ decays of the Υ(4S), which was set by CLEO using dilepton events is 13% [43]. At this level such decays would significantly affect our inclusive branching fraction. None of the non-$B\bar{B}$ decay models predict significant production of high momentum leptons, however. The sensitivity to the possibility of non-$B\bar{B}$ decays is therefore greatly reduced in the tagged analysis because of the requirement of a high momentum lepton tag and an additional electron in each event.

We assume effectively that all dilepton event are from B decays. Any possible mechanism through which non-$B\bar{B}$ decays of the Υ(4S) could affect this measurement would have to produce events which are remarkably similar to $B\bar{B}$, with high momentum leptons, a lepton momentum spectrum which is very similar to that for B decays, and kinematic characterictics similar to $B\bar{B}$ dileptons. While this can not be completely ruled out, it is unlikely.

Furthermore, we have combined the inclusive electron spectrum from the whole data set with the like- and unlike-sign electron spectra from the high momentum lepton subsample to set an upper limit on the fraction of non-$B\bar{B}$ decays at the Υ(4S). Assuming no direct lepton production from non-$B\bar{B}$ decays, the inclusive electron spectrum after all fake and background corrections is expressed as

$$\frac{dN(e^{\pm})}{dp} = 2N_{\Upsilon(4\mathrm{S})}(1-f)\eta(p)\left[\frac{d\mathcal{B}(b)}{dp} + \frac{d\mathcal{B}(c)}{dp}\right], \tag{4.9}$$

where f is the assumed fraction of non-$B\bar{B}$. In this equation, we have ignored the small fraction of $b \to u\ell\nu$ since $\mathcal{B}(b \to u\ell\nu) \approx 0.1\%$. By substituting the solutions $d\mathcal{B}(b)/dp$ and $d\mathcal{B}(c)/dp$ from equations (4.4) and (4.5) into the above equation, we obtain

$$\frac{dN(e^{\pm})}{dp} = \frac{2N_{\Upsilon(4\mathrm{S})}}{N_{\ell}}(1-f)\left[\frac{1}{\epsilon(p)}\frac{dN(\ell^{\pm}e^{\mp})}{dp_{(cut)}} + \frac{dN(\ell^{\pm}e^{\pm})}{dp}\right]. \tag{4.10}$$

The sum of like- and unlike-sign (corrected by $1/\epsilon(p)$ for unlike sign) spectra is compared with $dN(e^{\pm})/dp$ (scaled by $N_{\ell}/2N_{\Upsilon(4\mathrm{S})}$) in Fig. 4.19. The good agreement indicates a non-$B\bar{B}$ fraction close to zero. By integrating Eq. 4.10 from p_{min} to $p_{max} = 2.6$ GeV/c, we compute this fraction

$$f = 1 - \frac{N_{\ell}}{2N_{\Upsilon(4\mathrm{S})}} \frac{\int_{p_{min}}^{p_{max}} \frac{dN(e^{\pm})}{dp}dp}{\int_{p_{min}}^{p_{max}} \frac{1}{\epsilon(p)}\frac{dN(\ell^{\pm}e^{\mp})}{dp}dp + \int_{p_{min}}^{p_{max}} \frac{dN(\ell^{\pm}e^{\pm})}{dp}dp}. \tag{4.11}$$

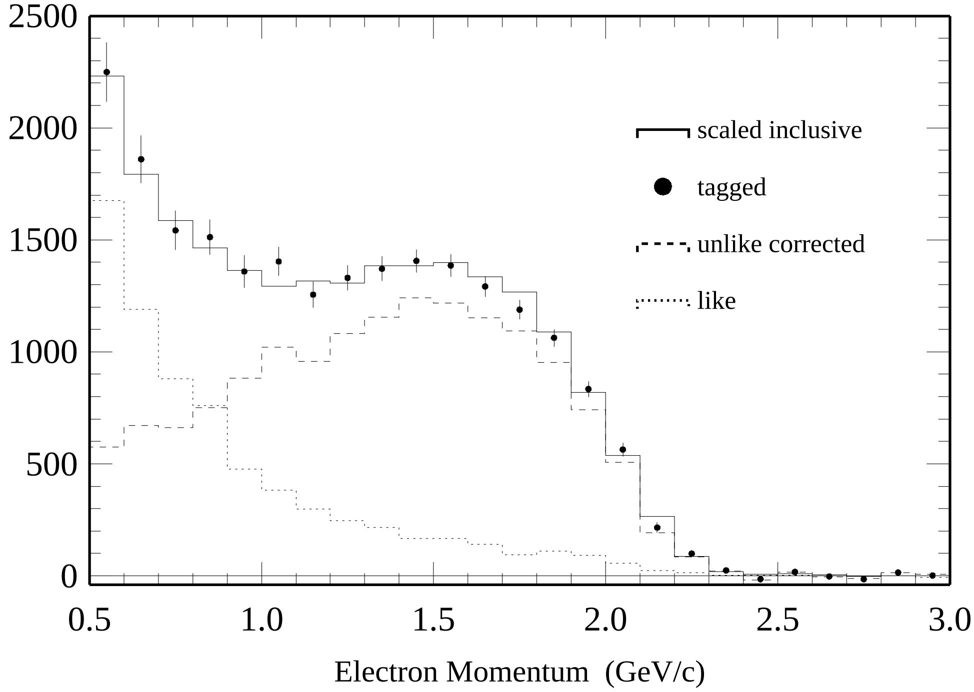

Figure 4.19: Comparison of inclusive electron spectrum $dN(e^{\pm})/dp$ (scaled by $N_\ell/2N_{\Upsilon(4S)}$) with the sum of like- and unlike-sign (corrected by efficieny of diagonal cut) electrons from the tagged sample.

The three integrals in this equation are summarized in Table 4.9 in two regions, 0.6–1.4 GeV/c and 1.4–2.6 GeV/c. In Table 4.10 we list the obtained values of f as a function of p_{min}. The errors are statistical and systematic. Most of the systematic contributions cancel when we take the ratio of the tagged electron spectrum to the inclusive, except the contribution to the N_ℓ calculation. This includes $\pm 25\%$ uncertainty in the fraction of leptons from secondary charm decay above 1.4 GeV/c and $\pm 25\%$

Table 4.9: Lepton and Dilepton Yields as represented by the integrals in Eq. 4.11

p range (GeV/c)	inclusive	unlike-sign	like-sign
$0.6 - 1.4$	$204,445 \pm 1,632$	$7,182 \pm 191$	$4,450 \pm 89$
$1.4 - 2.6$	$146,015 \pm 563$	$7,202 \pm 112$	871 ± 41
$N_\Upsilon(4S) = 2,143,430 \pm 4,546$		$N_\ell = 246,465 \pm 739$	

uncertainty in the relative event selection inefficiency of tagged events over inclusive lepton events.

Table 4.10: Fraction of non-$B\bar{B}$ decays at the Υ(4S).

p_{min} (GeV/c)	non-$B\bar{B}$ fraction f (%)	Upper Limit (%) 90% C.L.	95% C.L.
0.6	$-0.11 \pm 1.43 \pm 1.07$	2.87	3.43
1.0	$-0.66 \pm 1.44 \pm 1.06$	2.57	3.10
1.4	$-1.81 \pm 1.64 \pm 1.07$	2.31	2.83

The fraction of non-$B\bar{B}$ is consistent with zero within errors. We have calculated the 90% and 95% confidence level upper limit using the values of f and listed them in this table. The limit for f is quite stable when p_{min} varies from 0.6 GeV/c to 1.4 GeV/c. It is less than 4% at the 95% confidence level.

In conclusion, we have set a 4% upper limit for the fraction of non-$B\bar{B}$ decays of the Υ(4S) by assuming that there is no lepton production from such decays. The validity of this assumption should be questioned, as was investigated in an earlier CLEO note [43]. In that note, all available models were studied, including Υ(4S) decays to $c\bar{c}$, $D\bar{D}X$ and $D\bar{D}XY$, where X and Y are lighter mesons. It concluded that the upper limit either did not change or increased by no more than 15% of its value obtained from the ratio of inclusive leptons to dileptons. We therefore do not expect substantial changes in the 4% upper limit we obtained in this thesis, when taking into account these possbile decay modes.

4.8 Conclusion

We have reported a new measurement of the B meson semileptonic branching fractions with dilepton event samples collected with the CLEO-II detector at the $\Upsilon(4S)$ resonance. In each event we use a high momentum lepton to tag the semileptonic decay of one of the two B mesons, and collect the electron from the second B. We use kinematic correlations in this type of event to suppress the background when the electron is from the same side of the tag in an event. The primary and secondary electron spectra are separated by using charge correlations to solve the equations for the unlike-sign and like-sign spectra. We integrate over the primary spectrum to obtain the number of electrons directly from B semileptonic decays in the momentum acceptance above 0.6 GeV/c. Theoretical models are only used for extrapolation to lower momenta. Our measured value is

$$\mathcal{B}(B \to Xe\nu) = (10.46 \pm 0.17 \pm 0.43)\%, \tag{4.12}$$

where the first error is statistical and the second systematic. This measurement is largely independent of theoretical models and assumptions about possible non-$B\bar{B}$ decays of the $\Upsilon(4S)$. This result strongly supports our measurement with the inclusive lepton spectra, and most of the results from other experiments. The B-meson semileptonic branching fraction continues to be significantly below the current theoretical predictions.

From this measurement and the measurements of B-meson lifetime we obtain

$$|V_{cb}| = 0.041 \pm 0.001 \pm 0.002, \tag{4.13}$$

where the first error is experimental and the second one theoretical. By comparing the inclusive electrons and the tagged electrons we have set a 95% confidence level upper limit on the fraction of $\Upsilon(4S)$ decays to non-$B\bar{B}$ final states of 4%.

Chapter 5

Conclusion

We have carried out two analyses to answer the question: what is the semileptonic branching fraction of the B mesons? We draw conclusions in this chapter.

5.1 Summary of Results

To summarize, we collect in Table 5.1 and interpret our results from 2.057 fb^{-1} of data collected by the CLEO detector at the $\Upsilon(4S)$ resonance. With this substantially larger data sample and upgraded detector we have improved this measurement both statistically and systematically.

Table 5.1: Summary of Results

Model	Method	$\mathcal{B}(B \to X\ell\nu)\%$	$\lvert V_{cb}\rvert$
ACCMM		$10.56 \pm 0.04 \pm 0.22$	$0.042 \pm 0.001 \pm 0.004$
ISGW	fit $e + \mu$ spectra	$10.26 \pm 0.03 \pm 0.22$	$0.040 \pm 0.001 \pm 0.004$
ISGW**		$10.96 \pm 0.07 \pm 0.22$	$0.039 \pm 0.001 \pm 0.004$
none	high $\lvert\vec{p}\rvert$ lepton tagged	$10.46 \pm 0.17 \pm 0.43$	$0.041 \pm 0.001 \pm 0.002$

By fitting the inclusive spectra of electrons and muons from $\Upsilon(4S)$ decays to theory, we find $\mathcal{B}(B \to X\ell\nu) = (10.56 \pm 0.04 \pm 0.22)\%$ with the refined quark model by Altarelli *et al.,* and $\mathcal{B}(B \to X\ell\nu) = (10.96 \pm 0.07 \pm 0.22)\%$ with a modified version of the form factor model by Isgur *et al.,* in which the $D^{**}l\nu$ fraction is allowed to float. The fraction of $B \to D^{**}\ell\nu$ from this fit is $(23 \pm 1 \pm 5)\%$, somewhat larger than the model prediction. The fit to the original Isgur model yields a lower branching ratio, $\mathcal{B}(B \to X\ell\nu) = (10.26 \pm 0.03 \pm 0.22)\%$, with a higher χ^2.

To reduce the dependence on theoretical models and sensitivity to possible non-$B\bar{B}$ decays of the $\Upsilon(4S)$, we have made a second measurement with dilepton events. In each event we use a high momentum lepton to tag semileptonic decays of one of the two B mesons and collect the electron from the second B. We use kinematic correlations to suppress the background when the electron is from the same side of the tag in this type of events. The primary and secondary electron spectra are separated by using charge correlations to solve the equations for unlike-sign and like-sign events. We integrate over the primary spectrum to obtain the number of electrons directly from B semileptonic decays in the momentum acceptance above 0.6 GeV/c. Theoretical models are only used for extrapolation to lower momenta. We obtain $\mathcal{B}(B \to Xe\nu) = (10.46 \pm 0.17 \pm 0.43)\%$.

Based on our branching ratio results, we have also measured the CKM matrix element $|V_{cb}|$ with precision. Using predictions from models, we obtain from our first analysis $|V_{cb}| = 0.042 \pm 0.001 \pm 0.004$ with the ACCMM model, $|V_{cb}| = 0.040 \pm 0.001 \pm 0.004$ with the ISGW model and $|V_{cb}| = 0.039 \pm 0.001 \pm 0.004$ with the ISGW** model. Here the first error is experimental, including the errors in both the branching ratio and lifetime measurements, and the second error is an estimated 20% uncertainty in the model calculations. Combining the result from our second analysis and a recent paper based on operator product expansions[34] we obtain $V_{cb} = 0.041 \pm 0.001 \pm 0.002$. The experimental error in this result is largely model-independent and the theoretical uncertainty is greatly reduced due to the improved theoretical understanding. In addition, the fits with ACCMM and ISGW** showed a $b \to u\ell\nu$ component which is consistent with the CLEO measurement of $|V_{ub}/V_{cb}|$ [36].

The two measurements of $\mathcal{B}(B \to X\ell\nu)$ we made are consistent with each other, and they both strongly support previous observations that this branching ratio is significantly below the theoretical expectations. Our measurements are the most precise which have ever been made. Our lepton-tagged measurement (like that of the ARGUS experiment) is nearly independent of theoretical models, and is largely immune to the possibility of non-$B\bar{B}$ decays of the Υ(4S). By comparing the inclusive electron yield with the tagged electron yields we find at 95% confidence level that the fraction of Υ(4S) mesons that decay to non-$B\bar{B}$ final states is less than 4%.

5.2 Discussion

By two different procedures we have measured the B-meson semileptonic branching fraction to be less than 11%, while the theoretical expectation is 12.5% or more. Our measurements have relative errors of only a few percent, so this discrepancy is now very significant. What are the possible ways to account for this conflict between theory and experiment?

One possibility is that other semileptonic B decay channels may contribute more than is expected. So far we have measured $B \to X\ell\nu$ for $\ell = e$ or μ. An enhanced branching fraction for $B \to X\tau\nu$ would reduce the semileptonic fraction for electons and muons. The leptons produced in the decay chain $B \to X\tau\nu$, $\tau \to \ell\nu\bar{\nu}$ would have a substantially softer lepton momentum spectrum than those from $B \to X\ell\nu$. This is a consequence of the energy carried away by the three neutrinos in the τ mode. Our lepton spectra show no evidence of abnormally large contribution from such a low momentum component. More direct evidence has been obtained by the ALEPH experiment. They have measured $\mathcal{B}(B \to X\tau\nu) = (2.76 \pm 0.47 \pm 0.43)\%$, which is very consistent with the expectation in the Standard Model [32].

B semileptonic decay to baryons are another possible semileptonic mode which our analysis might miss. At CLEO we have searched for decays $B^0 \to \Lambda_c^+ \bar{p} \ell^- \bar{\nu}$ by fully reconstructing the missing mass of the event to check its consistency with a neutrino. We also studied the charge and kinematic correlations of leptons and baryons to see if they are from the same B meson. So far, we have observed no evidence for semileptonic decays with baryons, setting an upper limit on the branching fraction of 10^{-3}. The ARGUS experiment went further, by looking for the coexistence of a lepton and a proton in events with an additional high momentum lepton tag. No evidence was found, leading to an upper limit of 0.16% for such decays [12].

Another possible explanation for a too-small semileptonic branching fraction is enhancement in decay channels other than the semileptonic. These include the quark-pair channels in B weak decays (Fig. 1.2). As was discussed in Chapter 1, lowering the charm quark mass will increase the predicted rate for the nonleptonic $b \to c\bar{c}s$ transition, and thus reduce the semileptonic branching ratio. By using m_c/m_b values within the range of our present knowledge we find that the expected charm quark content per B decay is 1.1 – 1.2. Any effort to reduce the semileptonic branching ratio by lowering m_c will result in higher charm content, in contradiction with data (0.932 ± 0.10 charm quarks per B decay from ARGUS and 1.026 ± 0.057 from CLEO [44]).

Charmless hadronic transitions and non-spectator processes that do not produce charm states could be another candidate, if their branching ratios were significantly larger than expectations. The non-spectator modes include pure leptonic decays and "penguin" type decays. Pure leptonic decays $B \to \ell\bar{\nu}$ are heavily supressed by $|V_{ub}/V_{cb}|^2$. They are expected to contribute only below the 10^{-3} level. CLEO has set an upper limit for the $\ell = \tau$ channel, $\mathcal{B}(B \to \tau\nu) < 10^{-2}$. The channels for $\ell = e$ and μ are helicity suppressed with upper limits of about 10^{-5} [45]. Penguin decays are transitions through loop diagrams. They are higher order processes, and are generally expected to have branching ratios below 10^{-4}. The electromagnetic penguin decay $B \to K^*\gamma$ has been observed by CLEO at the 10^{-5} level [46]. Charmless hadronic decays $B \to K\pi$ and $B \to \pi\pi$ are mixtures of hadronic penguin and $b \to u$ transitions. Evidence for these two-body decays has been seen at CLEO, with branching ratio upper limits at the 10^{-5} level [47]. These small upper limits demonstrate convincingly that these modes cannot explain the small semileptonic branching fraction

Even though we have reduced the sensitivity to non-$B\bar{B}$ decays of the $\Upsilon(4S)$, there is still a small possibility that this type of unexpected decay could change our normalization, and thus reduce the semileptonic branching fraction. None of the plausible theoretical descriptions predicts significant lepton production in non-$B\bar{B}$ decays. Our tagged analysis required the presence of an electron and an additional high-momentum lepton tag to ensure that our leptons were indeed from B decay. This interpretation can be questioned only to the extent that non-$B\bar{B}$ decays of the $\Upsilon(4S)$ give rise to dileptons with momentum distributions and charge and kinematic correlations similar to those in B events. While this has not been completely ruled out, it is very unlikely.

It is beyond the scope of this thesis to assess the theoretical work that led to the predictions for semileptonic heavy quark decays. It is appropriate, however, to highlight some of the remaining uncertainties that could allow a lower semileptonic branching fraction for the B mesons [7].

The first is the perturbative correction to the parton description. It is by far the largest correction, and has reduced the prediction from 16.5% to a significantly lower level. The next-to-leading order correction (proportional to α_s^2, or g_3^4) could be unexpectedly large, and thereby decrease the semileptonic branching ratio further.

The non-perturbative correction is based on expanding the weak transition operator into a series of local operators with increasing dimensions. The coefficients of this series contain increasing powers of $1/m_Q$. So far it has been computed to order of $1/m_Q^2$. Several operators at order $1/m_Q^3$ have also been analyzed. If the $1/m_Q^3$ correction proves to be larger than expected, the lifetimes of the B^0, B^+, $B_s(b\bar{s})$ and $\Lambda_b(buu)$

would be quite different. CLEO has measured the lifetime ratio for B^+ and B^0 (τ^+/τ^0) to be $1.05 \pm 0.16 \pm 0.15$ [41]. Both the LEP experiments at CERN and the Tevatron experiments at Fermilab have been measuring the lifetimes, and they do not observe deviations in τ^+/τ^0 from the expectation of $\tau^+/\tau^0 \approx 1 - 1.05$, within statistics [48]. In short, no significant difference in lifetimes of the charged and neutral B mesons has been observed. Lifetime measurements with increased data samples will provide more stringent tests for this correction.

An additional possible shortcoming in the current theoretical treatment is the somewhat questionable applicability of quark-level QCD calculations. This approach effectively averages over all exclusive final states. This may not be completely appropriate in B semileptonic decay, where a small number of exclusive final states (D, D^*, D^{**}) dominate.

Still another possible scenario for resolving the theory-experiment conflict is that several effects could each contribute a few percent. These would likely include some of those discussed above, but might also include other effects which we have not yet identified.

An intriguing possibility has been recently suggested, and, one might conclude, hoped for [7]. This is the intervention of physics beyond our current understanding, the Standard Model. As we have just discussed, it is very difficult to adjust theoretical calculations to both a shortage of leptons and a shortage in the charm quark content of B decays. One speculation, for example, is that there might be some type of intermediate in new physics which interacts only with the lighter quarks, but with not leptons and charm. This might provide a successful, and revolutionary, explanation for our mystery.

However exciting the new physics may be, we must continue to pursue our efforts to determine if the measured B-semileptonic fraction can be accommodated by current theory. This shall be carried out with experimental work as well as theoretical. Complementing our inclusive studies, we foresee precision measurements of the lifetimes of B^-, B^0, B_s and Λ_b at LEP and the Tevatron. These will provide stringent constraints on the heavy quark expansion calculations. On a different front, CLEO is reaching the statistical capability to measure the form factors which describe semileptonic B decay. At the same time, heavy quark effective theory has made it possible not only to calculate leptonic decays, but also hadronic decays, when it is combined with chiral symmetry. The global effort to address these and other related questions is certain to result in great strides in our understanding of heavy quark decays and all fundamental interactions.

Appendix A

CLEO Terminology

1. General

`KLASGL` event class,

< 10 — QED, $\gamma\gamma$, cosmic ray events, etc.,

10 — hadronic events,

11 — beam gas events.

`Ebeam` beam energy of the collider run.

`Lumin` integrated luminosity of dataset.

2. Vertex

`IDTX` vertex type,

0 — primary,

2 — K_s^0,

4 — Λ^+,

8 — Λ^-.

`CHITX` χ^2 of fit to vertex.

`RBMTX` vertex displacement from interaction point.

`VMTX` mass of particle decayed at vertex.

3. Track

`NTRKCD`	number of charged tracks in CD (PT+VD+DR).
`PQCD`	track momentum with electric charge as sign.
`CZCD`	$\cos\theta$ of track where z is beam axis.
`DBCD`	track impact parameter in $r-\phi$.
`ZOCD`	track impact parameter in $r-z$.
`RESICD`	residue in tracking fitting.
`TRKMAN`	program to kill false tracks.
`KINCD`	general quality of track candidate,
	0 — track from primary vertex,
	2 — track from secondary vertex,
`IQALDI`	quality of dE/dx for a track,
	1 — good, more than 11 hits.
`NHITPT`	number of hits in PT for a track.
`NHITVD`	number of hits in VD for a track.
`RHITDR`	pecentage of DR hits over expected for a track.

4. Shower

`E9/E25`	ratio of energy deposit within the centeral 9 crystals over that of the centeral 25 crystals.

5. Lepton Identification

`R2ELEC`	likelihood for electron candidates.
`MUQAL`	quality of muon chamber hits matching CD track,
	0 — good, match in all layers,
	10K — fair, unsatisfactory match in one layer.
`DPTHMU`	depth of MU hits in unit of nuclear interaction length.

6. Monte Carlo

`PSAV`	generated 4-momentum of a particle.

Appendix B

Fake Rate Study from the Tagged Track Samples

The criteria for selecting $p\bar{p}$, $K^{\pm}$ and $\pi^{\pm}$ are listed below. These particles were selected as daughters of Λ, K_s^0 and D^0, D^{*+}. The effective mass distributions for candidates are shown in Fig. B.1.

1. p and $\bar{p}$ Selection:

   Vertex $\Lambda \to p\pi$

   - $\texttt{IDTX} = 4\ or\ 8$
   - $\texttt{CHITX} \leq 3.0$
   - $\texttt{RBMTX} \geq 0.01$
   - $|\texttt{VMTX} - 1.116| \leq 0.003$
   - $cos(\vec{p}(\Lambda), \vec{p}(vertex)) \geq 0.95$

   Both p and π tracks

   - $\texttt{KINCD} \geq 0$

- $|$DBCD$| \geq 0.001$
- IQALDI $= 1$

2. $\pi^{\pm}$ Selection:

   Vertex $K_s^0 \rightarrow \pi^+\pi^-$

   - IDTX $= 2$
   - CHITX ≤ 3.0
   - RBMTX ≥ 0.01
   - $|$VMTX $- 0.4977| \leq 0.008$
   - $cos(\vec{p}(\mathrm{K}_s^0), \vec{p}(vertex)) \geq 0.95$

Both π^+ and π^- tracks

   - KINCD ≥ 0
   - $|$DBCD$| \geq 0.001$
   - IQALDI $= 1$

3. $K^{\pm}$ Selection:

   $D^{*+} \rightarrow D^0\pi_s$ and $D^0 \rightarrow K^-\pi^+$

   K^- , π^+ and π_s^+ tracks

   - KINCD $= 0$
   - $|$DBCD$| \leq 0.005$
   - $|$CZCD$| \leq 0.05$
   - IQALDI $= 1$

Masses are calculated using particle assumptions

- $|m(K^-\pi^+) - 1.8645| \leq 0.025$

- $|[m(K^-\pi^+\pi_s^+) - m(K^-\pi^+\pi)] - 0.1455| \leq 0.0025$

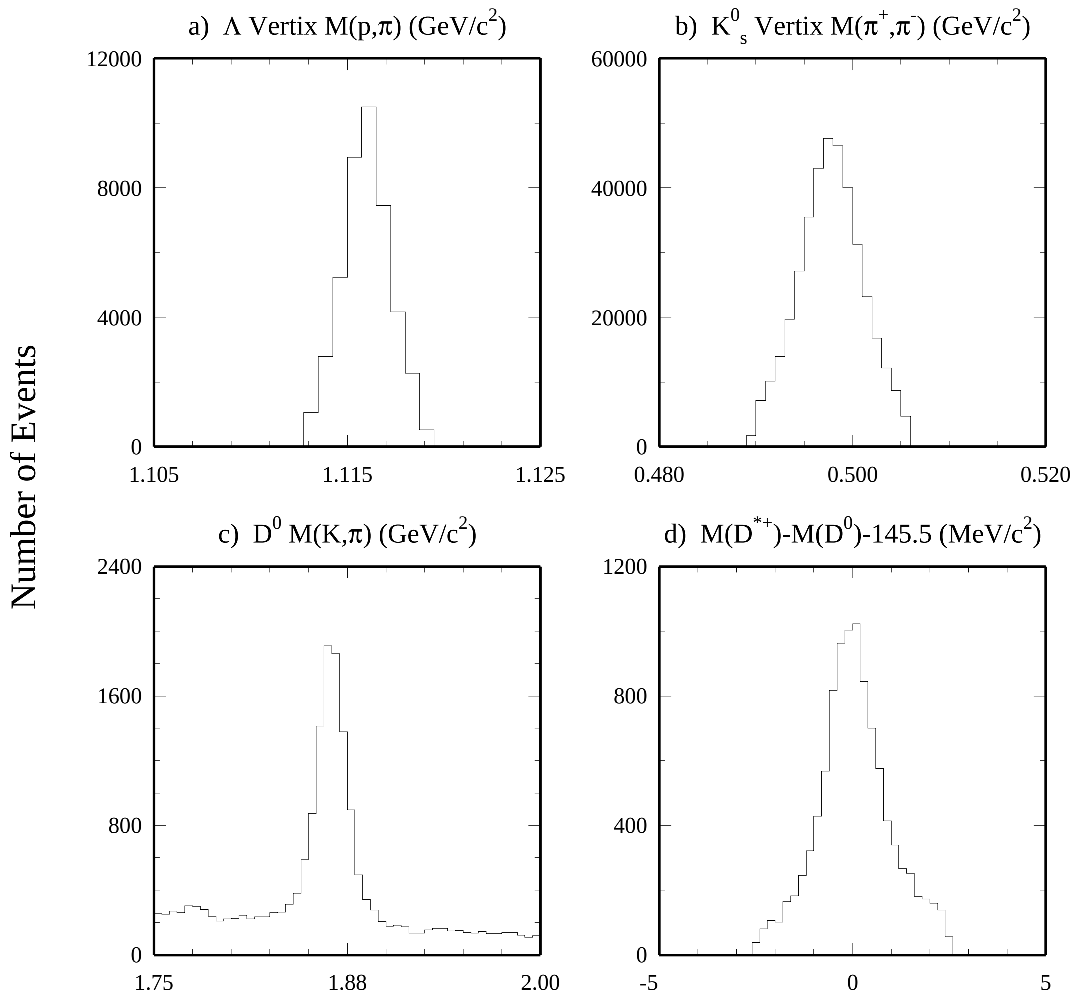

Figure B.1: Mass constraints for selecting $p\bar{p}$, $K^\pm$ and $\pi^\pm$ for fake-probability studies.

The individual lepton misidentification probabilities are shown in Fig. B.2. They are then combined according to the particle abundances at Υ(4S) from Monte Carlo, as shown in Fig. B.3, to give the results in Figs. 2.6 in Chapter 2.

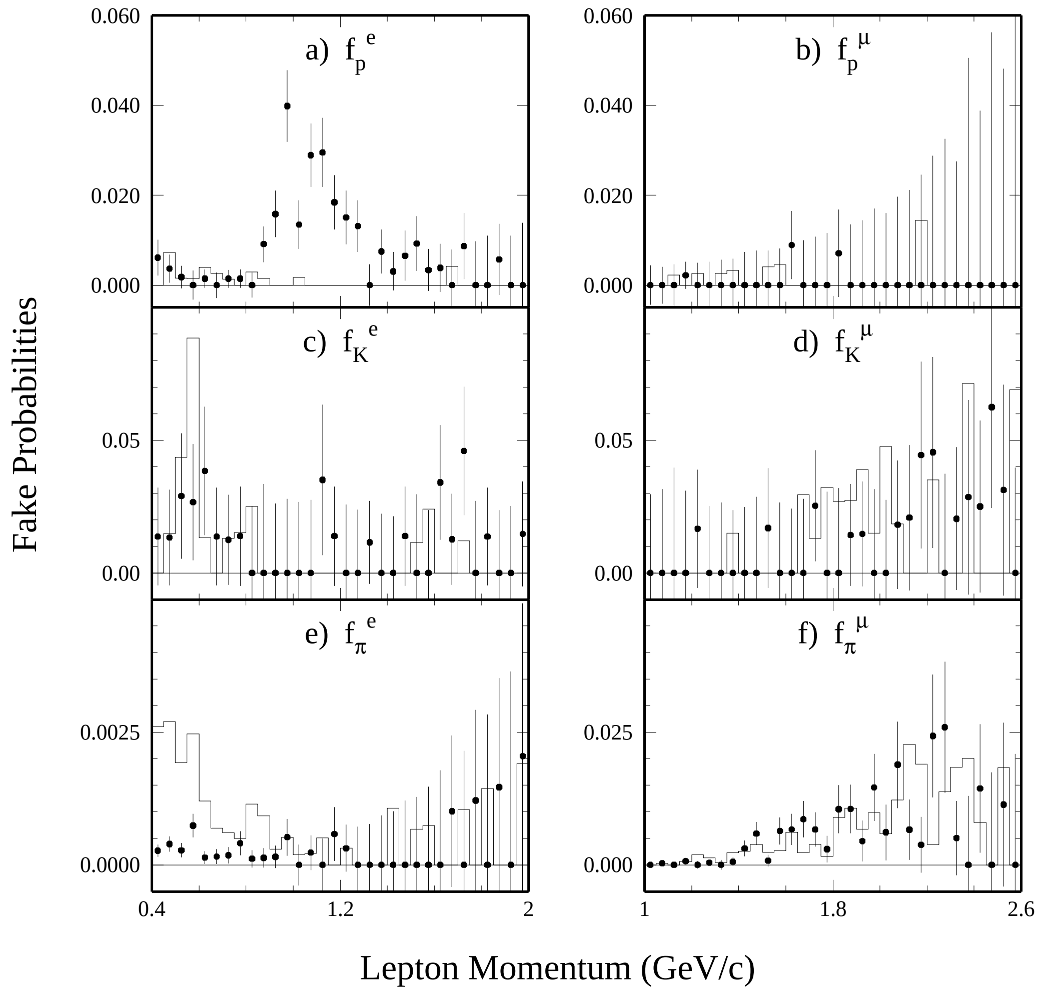

Figure B.2: Probabilities of misidentifying hadrons as leptons as a function of momentum. The the electron fake probabilities are shown on the left and the muon fake probabilities on the right. The histograms are for positive charge tracks and the dots are for negative.

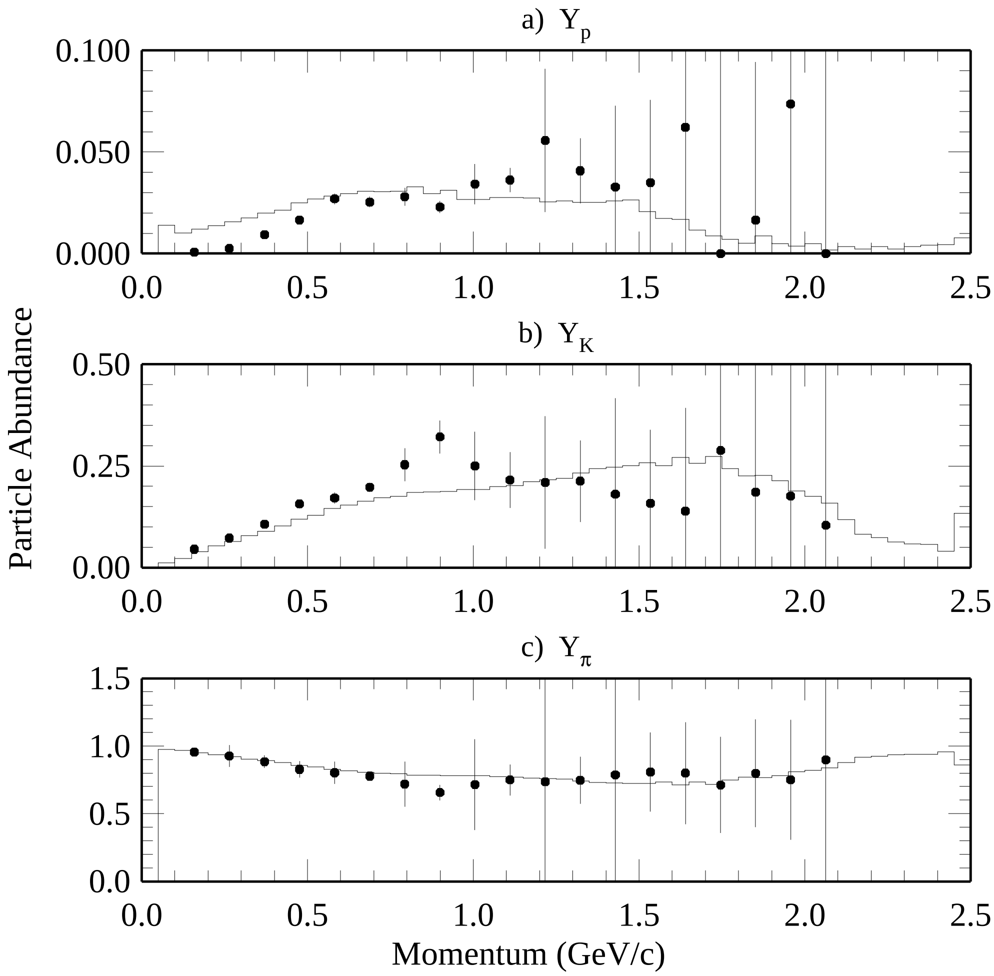

Figure B.3: Particle abundances at the $\Upsilon(4S)$ as a function of momentum. The histograms are from Monte Carlo and the dots are measured from data [27].

We also made a cross check by combining the p, K, π fake probabilities with their measured abundance at $\Upsilon(1S)$ [27] and comparing the results with the fake rates measured directly from $\Upsilon(1S)$ which was described in Chapter 2. As is demonstrated by Fig. B.4, the agreement between the two measurements of lepton fakes at $\Upsilon(1S)$ is adequate.

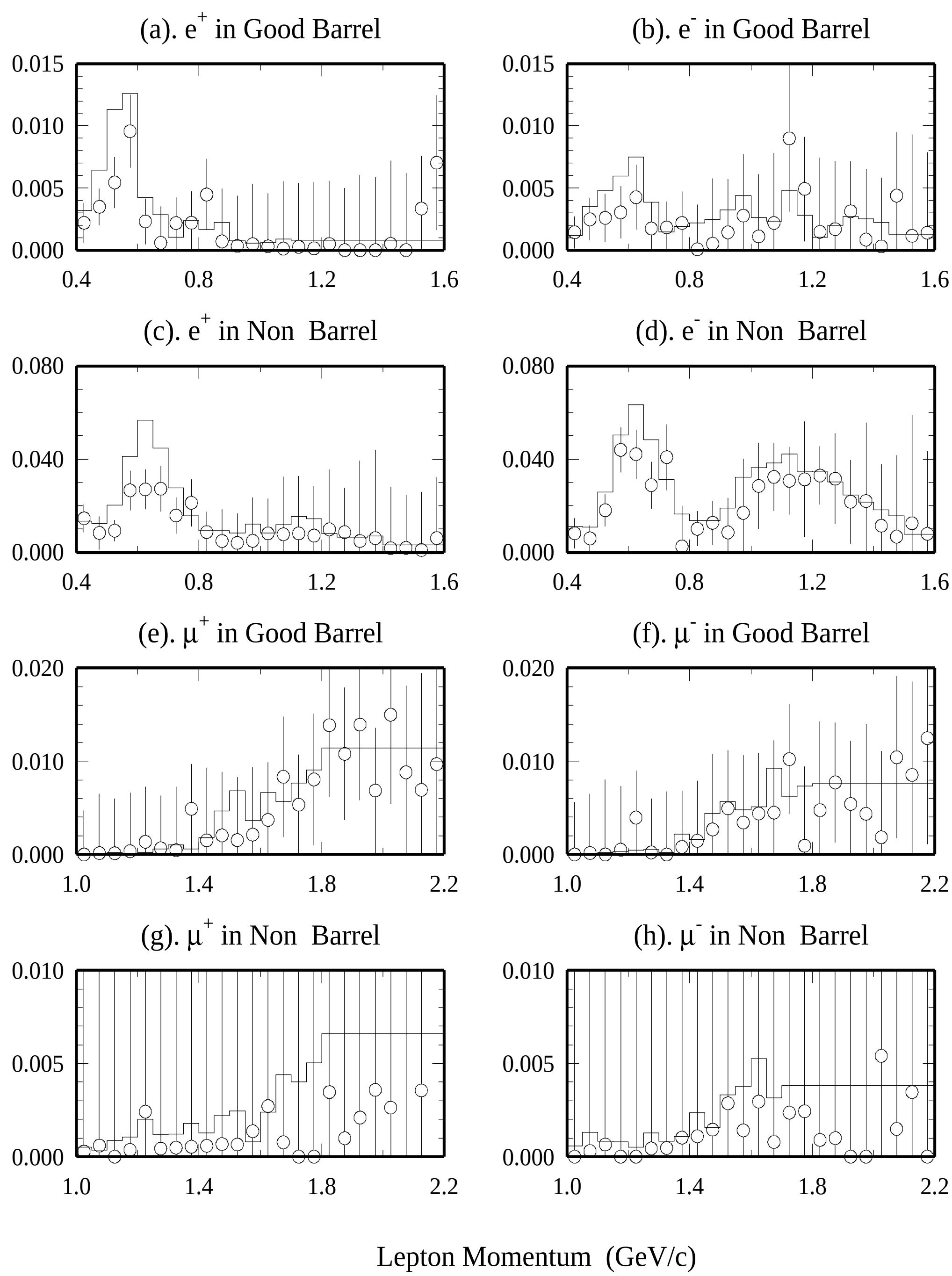

Figure B.4: Comparison of two measurements of fake rates at $\Upsilon(1S)$. The histograms are from the direct measurement described in Chapter 2 and the dots are from combined p, K and π contributions.

Appendix C

Over-Subtraction Factor r in $\Upsilon(1S)$ Fake Rate Study

The contribution to the $\Upsilon(1S)$ lepton spectra due to $\Upsilon(1S) \to \gamma^* \to q\bar{q}$ decay processes is excluded in the $\Upsilon(1S)$ fake rate study by over subtracting the continuum. The over subtraction factor r in Equation 2.4 in Section 3.2 is defined as follows.

$$
\begin{aligned}
r &= \frac{\sigma_{had}(\Upsilon(1S) \to \gamma^*)}{\sigma_{had}(continuum)} && \text{(C.1)} \\
&= \frac{R_{had}(\Upsilon(1S))\sigma^{res}(\Upsilon(1S) \to \mu^+\mu^-)}{\sigma_{had}(continuum)} && \text{(C.2)} \\
&= R_{had}(\Upsilon(1S))\mathcal{B}_{\ell\ell}(\Upsilon(1S))\frac{\sigma^{res}_{tot}(\Upsilon(1S))}{\sigma^{had}_{tot}(continuum)} && \text{(C.3)}
\end{aligned}
$$

where the quantities with subscript "had" are hadronic and thsese with "res" are from the $\Upsilon(1S)$ resonance. By using

$$\Gamma_{tot}(\Upsilon(1S)) = \frac{\Gamma^{had}(\Upsilon(1S))}{1 - 3\mathcal{B}_{\ell\ell}} \tag{C.4}$$

we obtain

$$r = R_{had}(\Upsilon(1S))\frac{B_{\ell\ell}(\Upsilon(1S))}{1 - 3\mathcal{B}_{\ell\ell}}\frac{\sigma^{res}_{had}(\Upsilon(1S))}{\sigma_{had}(continuum)} \tag{C.5}$$

where $\mathcal{B}_{\ell\ell} = \mathcal{B}(\Upsilon(1S) \to \ell^+\ell^-)$.

Now we list the values for the quantities involved in the above equation and calculate the value for r.

From the weighted average of the measurements[49] shown in Tab. C.1 we obtain

$$R_{had(\Upsilon(1S))} = 3.63 \pm 0.14$$

.

Table C.1: Measurements of R_{had} at $\Upsilon(1S)$ Region

Experiment	R_{had}	Energy(GeV)
PLUTO	$3.67 \pm 0.23 \pm 0.29$	9.4
DASP-II	$3.73 \pm 0.16 \pm 0.28$	9.5
LENA	$3.37 \pm 0.06 \pm 0.28$	7.4-9.4
CUSB	$3.63 \pm 0.06 \pm 0.37$	10.4-10.5
CLEO	$3.77 \pm 0.06 \pm 0.26$	10.4-10.5
Average	3.63 ± 0.14	

The weighted average of τ, μ and e from [1] gives

$$\mathcal{B}_{\ell^+\ell^-} = 2.50 \pm 0.06\%$$

which are listed in Tab. C.2.

Table C.2: PDG-92 $\mathcal{B}_{\ell\ell}$ Values

mode	$\mathcal{B}_{\ell^+\ell^-}(\%)$
$\tau^+\tau^-$	2.97 ± 0.35
$\mu^+\mu^-$	2.48 ± 0.06
e^+e^-	2.52 ± 0.17
$\ell^+\ell^-$	2.50 ± 0.06

The value for $\sigma_{had}(continuum)$ is derived from[1, 49]

$$\sigma_{had}(continuum) = R_{had}(\Upsilon(1S))\sigma(e^+e^- \to \mu^+\mu^-) \quad \text{(C.6)}$$

$$
\begin{aligned}
&= (3.63 \pm 0.14) \times \frac{86.8}{(9.460 \pm 0.004)^2} &\quad (C.7)\\
&= 3.52 \pm 0.14(nb) &\quad (C.8)
\end{aligned}
$$

Last, the resonance hadronic cross section at the $\Upsilon(1S)$ has been measured both in CLEO and CUSB. From Plunkett's thesis[50] in CLEO, we have

$$\sigma^{res}_{had}(\Upsilon(1S)) = \frac{15.87(nb)}{\epsilon(=82\%)} = 19.35(nb)$$

The average of this CLEO result and the CUSB result 18.0 nb is 18.7 (nb), which agrees with the value 18.55 nb estimated from CLEO II data. Thus we use

$$\sigma^{res}_{had}(\Upsilon(1S)) = 18.7 \pm 1.0(nb)$$

in the calculation of r.

By using the values of the above four quantities we finally obtain

$$r = 0.52 \pm 0.04$$

.

Appendix D

Tabulated Spectra

Table D.1: Inclusive muon spectrum in Chapter 3.

p (GeV/c)	dN_μ/dp (GeV/c^{-1})	$\delta(dN_\mu/dp)$ (GeV/c^{-1})	p (GeV/c)	dN_μ/dp (GeV/c^{-1})	$\delta(dN_\mu/dp)$ (GeV/c^{-1})
1.30	9.588e-2	4.40e-3	1.35	9.430e-2	2.83e-3
1.40	9.375e-2	2.30e-3	1.45	9.563e-2	2.00e-3
1.50	9.060e-2	1.82e-3	1.55	9.530e-2	1.74e-3
1.60	9.404e-2	1.67e-3	1.65	9.129e-2	1.58e-3
1.70	9.051e-2	1.52e-3	1.75	8.534e-2	1.49e-3
1.80	8.066e-2	1.41e-3	1.85	7.481e-2	1.33e-3
1.90	6.612e-2	1.24e-3	1.95	5.637e-2	1.18e-3
2.00	4.422e-2	1.09e-3	2.05	3.369e-2	9.98e-4
2.10	2.496e-2	8.86e-4	2.15	1.590e-2	8.13e-4
2.20	8.525e-3	7.72e-4	2.25	3.946e-3	6.57e-4
2.30	1.099e-3	6.25e-4	2.35	1.163e-3	5.54e-4
2.40	1.441e-3	5.50e-4	2.45	-1.417e-4	4.70e-4
2.50	1.163e-3	4.61e-4	2.55	8.926e-5	6.13e-4
2.60	3.160e-4	4.07e-4	2.65	3.394e-4	3.78e-4
2.70	8.022e-5	3.86e-4	2.75	3.900e-6	3.54e-4

Table D.2: Inclusive electron spectrum in Chapter 3.

p (GeV/c)	dN_e/dp (GeV/c^{-1})	$\delta(dN_e/dp)$ (GeV/c^{-1})	p (GeV/c)	dN_e/dp (GeV/c^{-1})	$\delta(dN_e/dp)$ (GeV/c^{-1})
0.60	1.284e-1	5.44e-3	0.65	1.203e-1	5.14e-3
0.70	1.160e-1	4.75e-3	0.75	1.037e-1	3.97e-3
0.80	1.021e-1	3.67e-3	0.85	9.943e-2	4.14e-3
0.90	9.388e-2	3.66e-3	0.95	9.348e-2	3.37e-3
1.00	8.483e-2	3.86e-3	1.05	8.583e-2	4.60e-3
1.10	8.923e-2	2.71e-3	1.15	8.595e-2	2.70e-3
1.20	8.623e-2	3.84e-3	1.25	8.769e-2	2.31e-3
1.30	9.302e-2	2.16e-3	1.35	9.097e-2	1.60e-3
1.40	9.202e-2	1.56e-3	1.45	9.569e-2	1.54e-3
1.50	9.270e-2	1.44e-3	1.55	9.288e-2	1.40e-3
1.60	8.951e-2	1.34e-3	1.65	8.967e-2	1.34e-3
1.70	8.919e-2	1.29e-3	1.75	8.255e-2	1.23e-3
1.80	7.935e-2	1.21e-3	1.85	7.180e-2	1.16e-3
1.90	6.255e-2	1.09e-3	1.95	5.265e-2	1.02e-3
2.00	4.309e-2	9.55e-4	2.05	3.367e-2	8.53e-4
2.10	2.368e-2	7.67e-4	2.15	1.526e-2	6.94e-4
2.20	8.746e-3	6.13e-4	2.25	4.295e-3	5.24e-4
2.30	1.949e-3	4.85e-4	2.35	8.969e-4	4.20e-4
2.40	7.667e-4	3.98e-4	2.45	1.623e-4	3.71e-4
2.50	7.465e-4	3.40e-4	2.55	3.767e-4	3.16e-4
2.60	7.260e-4	2.95e-4	2.65	4.001e-4	2.95e-4
2.70	-4.889e-4	2.90e-4	2.75	8.165e-5	2.69e-4

Table D.3: Primary electron spectrum in Chapter 4.

p (GeV/c)	dN_e/dp (GeV/c^{-1})	$\delta(dN_e/dp)$ (GeV/c^{-1})	p (GeV/c)	dN_e/dp (GeV/c^{-1})	$\delta(dN_e/dp)$ (GeV/c^{-1})
0.60	3.738e-2	6.29e-3	0.70	3.931e-2	5.28e-3
0.80	4.476e-2	4.83e-3	0.90	5.834e-2	4.55e-3
1.00	6.678e-2	4.04e-3	1.10	6.444e-2	3.79e-3
1.20	7.401e-2	3.72e-3	1.30	7.956e-2	3.64e-3
1.40	8.804e-2	3.46e-3	1.50	8.498e-2	3.28e-3
1.60	8.164e-2	3.18e-3	1.70	7.880e-2	2.99e-3
1.80	7.017e-2	2.72e-3	1.90	5.560e-2	2.56e-3
2.00	3.870e-2	2.20e-3	2.10	1.503e-2	1.81e-3
2.20	6.610e-3	1.28e-3	2.30	1.649e-3	1.11e-3
2.40	-1.273e-3	1.02e-3	2.50	1.049e-3	7.26e-4
2.60	-2.491e-4	6.09e-4	2.70	-8.262e-4	7.35e-4

Table D.4: Secondary electron spectrum in Chapter 4.

p (GeV/c)	dN_e/dp (GeV/c^{-1})	$\delta(dN_e/dp)$ (GeV/c^{-1})	p (GeV/c)	dN_e/dp (GeV/c^{-1})	$\delta(dN_e/dp)$ (GeV/c^{-1})
0.60	8.484e-2	4.23e-3	0.70	6.239e-2	3.48e-3
0.80	5.302e-2	3.13e-3	0.90	3.080e-2	2.65e-3
1.00	2.192e-2	2.13e-3	1.10	1.616e-2	1.94e-3
1.20	1.160e-2	1.74e-3	1.30	8.810e-3	1.61e-3
1.40	4.460e-3	1.49e-3	1.50	4.652e-3	1.45e-3
1.60	3.103e-3	1.31e-3	1.70	-8.014e-5	1.07e-3
1.80	2.138e-3	1.23e-3	1.90	2.058e-3	1.17e-3
2.00	9.183e-4	9.23e-4	2.10	5.563e-4	7.20e-4
2.20	5.537e-4	3.27e-4	2.30	2.592e-5	2.47e-4
2.40	3.116e-4	3.36e-4	2.50	-2.287e-6	2.06e-4

References

[1] Particle Data Group, Review of Particle Properties, Phys. Rev. **D 45**, 11 (1992).

[2] J.Z. Bai *et al.,* (BES), Phys. Rev. Lett. **69**, 3021 (1992).

[3] F. Abe *et al.,* (CDF) FERMILAB-PUB-94-097-E (1994).

[4] G. Kane, Modern Elementary Particle Physics, (Addison-Wesley, 1987);
V. Barger and R. Phillips, Collider Physics, (Addison-Wesley, 1987).

[5] S. Stone, B Decays, 2nd ed. (World Scientific, 1994).

[6] G. Altarelli and S. Petrarca, Phys. Lett. **B 261** 303 (1991).

[7] I. Bigi *et al.,* Phys. Lett. **B 323** 408 (1994).

[8] N. Cabibbo and L. Maiani, Phys. Lett. **B 79** 109 (1978);
M. Suzuki, Nucl. Phys. **B 145** 420 (1978).

[9] C. Quigg and J. Rosner, Phys. Rev. **D 19** 1532 (1979).

[10] G. Altarelli and L. Maiani, Phys. Lett. **B 52** 351 (1974);
M.K. Gaillard and B.W. Lee, Phys. Rev. Lett. **33** 108 (1974).

[11] S. Henderson *et al.,* (CLEO), Phys. Rev. **D 45** 2212 (1992);
M.A. Worris, Ph.D. Thesis, Cornell University (1991).

[12] H. Albrecht *et al.,* (ARGUS), Phys. Lett. **B 249** 359 (1990).

[13] G. Altarelli *et al.,* Nucl. Phys. **B 208** 365 (1982).

[14] N. Cabibbo *et al.,* Nucl. Phys. **B 155** 93 (1979).

[15] N. Isgur *et al.,* Phys. Rev. **D 39** 799 (1989).

[16] M. Wirbel *et al.,* Zeit. Phys. **C 29** 637 (1985).

[17] J. Körner and G. Schuler, Zeit. Phys. **C 38** 511 (1988).

[18] N. Isgur and M. Wise, Phys. Lett. **B 232** 113 (1990);
N. Isgur and M. Wise, Phys. Lett. **B 237** 527 (1990).

[19] M. Wise, Proc. of XVI Int. Symp. on Lepton-Photon Interactions, 253 (1994).

[20] I. Bigi *et al.,* Phys. Rev. Lett. **71** 496 (1993).

[21] D. Atwood and W. Marciano, Phys. Rev. **D 41**, 1736 (1990).

[22] M. Sands, SLAC-121(1970).

[23] Y. Kubota *et al.,* (CLEO), Nucl. Instr. Meth. **A 320** 66 (1992).

[24] T. Haupt, CLEO Note CBX 91-78 (1991).

[25] B. Gittelman *et al.,* CLEO Note CBX 91-82 (1991).

[26] S. Schrenk, CLEO Note CBX 93-20 (1993);
S.E. Schrenk, Ph.D. Thesis, University of Minnesota (1994).

[27] D.N. Brown, Ph.D. Thesis, Purdue University (1992).

[28] J. Bartelt *et al.,* (CLEO), Inclusive Measurement of B-meson Semileptonic Branching Fractions, submitted to XVI Intl. Symp. on Lepton-Photon Interactions, Ithaca, NY (1993);
R. Wang *et al.,* CLEO Note CBX 93-71 (1993).

[29] D. Perticone and A. Silverman, CLEO Note CBX 92-47 (1992);
J. Nelson *et al.,* CLEO Note CBX 92-56 (1992).

[30] H. Kroha, CLEO Note CBX 91-53 (1991).

[31] D. Bortoletto *et al.,* (CLEO), Phys. Rev. **D 45** 21 (1992);
J. Lewis Ph.D. Thesis, Cornell University (1991).

[32] D. Buskulic *et al.,* (ALEPH), Phys. Lett. **B 298** 479 (1993).

[33] W. Bacino *et al.,* (DELCO), Phys. Rev. Lett. **43**, 1073 (1979).

[34] M. Shifman *et al.,* TPI-MINN-94/13-T, UMN-TH-1251-94, NSF-ITP-94-39 (1994).

[35] D. Besson, Proc. of XVI Int. Symp. on Lepton-Photon Interactions, 221 (1994).

[36] J. Bartelt *et al.,* (CLEO), Phys. Rev. Lett. **72** 4111 (1993);
F. Muheim *et al.,* CLEO Note CBX 93-36 (1993);
J. Nelson, Ph.D. Thesis, University of Minnesota (1994).

[37] R. Wang and R. Poling, CLEO Note CBX 94-29 (1994).

[38] H. Albrecht *et al.,* (ARGUS), Phys. Lett. **B 318** 397 (1993).

[39] P.L. Tipton, Ph.D Thesis, University of Rochester (1987).

[40] A. Albrecht *et al.,* (ARGUS), Zeit. Phys. **C 5** 357 (1992);
J. Bartelt *et al.,* (CLEO), Phys. Rev. Lett. **71** 1680 (1993);
D. Perticone and A. Silverman, CLEO Note CBX 92-47 (1992);
H. Kroha *et al.,* CLEO Note CBX 92-35 (1992);
C.H. Wang, Ph.D. Thesis, University of Rochester (1993).

[41] M. Artuso *et al.,* (CLEO), A Measurement of the Charged to Neutral B Meson Lifetime Ratio, submitted to XVI Intl. Symp. on Lepton-Photon Interactions,

Ithaca, NY (1993);

K. Kinoshita *et al.,* CLEO Note CBX 93-70 (1993).

[42] A. Khodjamirian *et al.,* Phys. Lett. **B 242** 489 (1990).

[43] M. Battle *et al.,* CLEO Note CBX 90-44 (1990).

[44] M. Danilov, *B* Physics Plenary Talk, EPS Conference, Marseille (1993).

[45] D. Cinabro, The Fermilab Meeting — DPF 92, 843 (1993).

[46] R. Ammar *et al.,* (CLEO), Phys. Rev. Lett. **71** 674 (1993).

[47] M.Battle *et al.,* (CLEO), Phys. Rev. Lett. **71** 3922 (1993).

[48] W. Venus, Proc. of XVI Int. Symp. on Lepton-Photon Interactions, 274 (1994).

F. Abe *et al.,* (CDF), FERMILAB-Pub-94/034-E (1994).

[49] P. and J. Franzini, Ann. Rev. Nucl. Part. Sci. **33**, 1 (1983).

[50] R. Plunkett, Ph.D. Thesis, Cornell University (1983).

[51] F. Muheim, Charm Production in *B* Meson Decays, DPF Meeting (1994).

[52] Particle Data Group, Review of Particle Properties, Phys. Rev. **D 50**, 1173 (1994).